UNIVERSIDAD DE VALENCIA - CSIC

DEPARTAMENTO DE FíSICA ATÓMICA, MOLECULAR Y NUCLEAR

INSTITUTO DE FÍSICA CORPUSCULAR

β-decay Total Absorption Spectroscopy measurements for reactor decay heat calculations

TESIS DOCTORAL

MARÍA DOLORES JORDÁN MARTÍN

Enero de 2010

José Luis Taín Enríquez, Invesigador Científico del Consejo Superior de Investigaciones Científicas (CSIC), y **Alejandro Algora** Científico Titular del Consejo Superior de Investigaciones Científicas

CERTIFICAN:

Que la presente memoria "***β-decay Total Absorption Spectroscopy measurements for reactor decay heat calculations***" ha sido realizada bajo su dirección en el Instituto de Física Corpuscular (Centro Mixto Universidad de Valencia - CSIC) por **María Dolores Jordán Martín** y constituye su Tesis doctoral dentro del programa de doctorado del Departamento de Física Atómica, Molecular y Nuclear.

Y para que así conste, en cumplimiento con la legislación vigente, presenta ante el Departamento de Física Atómica, Molecular y Nuclear la referida memoria, firmando el presente certificado en Burjassot (Valencia) a 29 de Enero de 2010.

Contents

List of Figures

List of Tables

1 General overview

1.1 β-decay

1.1.1 Introduction to β-decay

β-decay is one of the most common nuclear decay mechanisms given in nature. This process, governed by the Weak Interaction, is responsible for the conversion of one type of nucleon (proton or neutron) into another. Depending on the type of β-decay, a proton is converted into a neutron, or a neutron into a proton. The first type is known as β^+-decay, and the last type is called β^--decay. There is also a third type of decay classified as β-decay, similar to β^+-decay but in this case, the proton captures one of the atomic electrons before converting into a neutron. This third type is called electron capture, and competes with β^+-decay on the proton-rich side of the valley of stability. In all these processes, the mass number remains constant but Z and N changes by one unit.

The β-decay process also involves the emission of two additional particles depending on the type, an electron (or positron) and a neutrino (or antineutrino):

- β^- decay: $n \rightarrow p + e^- + \bar{\nu}_e$
- β^+ decay: $p \rightarrow n + e^+ + \nu_e$
- Electron Capture (EC): $p + e^- \rightarrow n + \nu_e$

In order for any of these processes to take place, the decay must be energetically possible. It means that the energy released in the β-decay process, Q-value, must be positive. The Q-value is defined as the difference in mass-energy between the initial and

the final states, i.e,

$$Q_{\beta^-} = [M(^A_Z X_N) - M(^A_{Z+1} X_{N-1})]c^2 = E_{\beta^-} + E_{\overline{\nu}} + E_{ex}$$
$$Q_{\beta^+} = [M(^A_Z X_N) - M(^A_{Z-1} X_{N+1})]c^2 = E_{\beta^+} + E_\nu + E_{ex} + 2m_e c^2$$
$$Q_{EC} = [M(^A_Z X_N) - M(^A_{Z-1} X_{N+1})]c^2 = E_\nu + B_i$$

In these equations, $M(^A_Z X_N)$, $M(^A_{Z+1} X_{N-1})$ and $M(^A_{Z-1} X_{N+1})$ are the atomic masses of the mother and daughter nuclei respectively, c is the speed of light, E_β is the β particle energy, E_ν is the neutrino (anti-neutrino) energy, E_{ex} is the excitation energy of the daughter nucleus and B_i is the binding energy of the electron in orbit i (K, L,...) from which it was captured.

Then, if we have in mind the previous relations, the β^+ decay process is limited to a minimum energy of 1022 keV in order to occur. This threshold determines that this kind of decay may not be energetically possible for lower transition energies (less than 1022 keV) and then, only electron capture is possible. On the neutron-rich side of the valley of stability, only the β^--decay process is possible.

1.1.2 Conservation laws and selection rules

The β-decay process obeys very well defined conservation laws and selection rules. They are related to the intrinsic properties of the particles emitted in the decay, in particular the spin S, and the angular momentum L they are emitted with:

- When the β-particle (electron or positron) and neutrino (or antineutrino) are emitted with zero orbital angular momentum, which is called the allowed approximation, only the intrinsic spins of those particles need to be considered in the transition between initial and final states ($\pi_i = \pi_f$). In such a way, we can define two types of transitions depending on whether the spins of the particles are parallel or anti-parallel, i.e., total S=1 or total S=0:
  - Total S=1: in this case, the total change in nuclear spin between initial and final states, ΔJ, could be 0 or 1 (with the exception of the 0-0 transition). Then the transition is called a *Gamow-Teller transition.*
  - Total S=0: in this transition, ΔJ must be 0 and the transition is known as *Fermi transition.*
- In case both particles are emitted with $L \neq 0$, the decay is called forbidden. This type of decay occurs with lower probability than allowed decays. The order of forbiddenness increases with L-value. For each forbidden decay, both types of transitions defined above can occur, and the parity between initial and final states may not be the same.

Defining the initial and final angular momenta as $\overrightarrow{I_i}$ and $\overrightarrow{I_f}$, respectively, we can generalize these rules for any $\overrightarrow{L}$:

$\overrightarrow{I_f} = \overrightarrow{I_i} + \overrightarrow{L}$	Fermi-type transition
$\overrightarrow{I_f} = \overrightarrow{I_i} + \overrightarrow{L} + \overrightarrow{1}$	Gamow-Teller-type transition
$\pi_i = \pi_f(-1)^L$	Connection between parity, π, and angular momentum

1.1.3 Characterization of β-decay

A way to compare the β-decay properties in different nuclei is through the so called *log ft* value. It is defined as[1]:

$$ft = \frac{C}{\langle F\rangle^2 + \left(\frac{g_A}{g_V}\right)^2 \langle GT\rangle^2} \tag{1.1}$$

In equation (1.1), C is a constant, and g_V and g_A are the weak-coupling vector and axial vector coupling constants and f is called statistical rate function or the phase-space factor containing the energy dependence of the transition. This equation shows the relationship between the partial half-life t with the Fermi and Gamow-Teller nuclear matrix elements:

$$\langle F\rangle = \langle \psi_f | \sum_{k=1}^{A} \tau_k^{\pm} | \psi_i \rangle \tag{1.2}$$

$$\langle GT\rangle = \langle \psi_f | \sum_{k=1}^{A} \overrightarrow{\sigma}_k \tau_k^{\pm} | \psi_i \rangle \tag{1.3}$$

Variations in the *log ft* values must only be due to differences in the nuclear matrix elements and thus, to differences in the nuclear wave functions.

The square of the two nuclear matrix elements mentioned above are called the Fermi and Gamow-Teller strengths, B(F) and B(GT), respectively. The ft value can be rewritten with these strengths as follows[2]

$$ft = \frac{C}{B(F) + \left(\frac{g_A}{g_V}\right)^2 B(GT)} \tag{1.4}$$

Due to the isospin selection rule, the Fermi decay is suppressed over most of the nuclear chart. Then, we are going to consider only the particular case of pure Gamow-Teller transitions. Rather than the B(GT), we will use the related magnitude β-strength distribution $S_\beta(E_x)$. This distribution as a function of the excitation energy, E_x, is related to the normalized β-feeding distribution, also called β-intensity or I_β, by

$$S_\beta(E_x) = \frac{I_\beta(E_x)}{f(Q_\beta - E_x)T_{1/2}}$$

where $T_{1/2}$ is the β-decay half-life, and $f(Q_\beta - E_x)$ is the statistical rate Fermi function, which depends both on the β process type and on the available energy to the decay, $Q_\beta - E_x$. All the variables involved in equation (1.5) can be experimentally measured. Most commonly $S_\beta(E_x)$ is defined as an average quantity which stands for the mean value of the total rate for all the transitions occurring to levels inside a certain energy bin ΔE_x at central excitation energy E_x

$$S_\beta(E_x) = \frac{1}{T_{1/2}} \sum_{E_x \in \Delta E_x} \frac{1}{\Delta E_x} \frac{I_\beta(E_x)}{f(Q_\beta - E_x)} \tag{1.5}$$

This quantity is introduced in order to deal with the situation where the level density in the daughter nucleus in the β-decay is too large to distinguish individual levels, but it is applicable when the level density is low too.

B(GT) and β-strength are related by the equation

$$S_\beta(E_x) = \frac{1}{6147 \pm 7} \left(\frac{g_A}{g_V}\right)^2 \sum_{E_f \in \Delta E_x} \frac{1}{\Delta E_x} B(GT)_{i \to f} \tag{1.6}$$

Additionally, the integral value of $S_\beta(E_x)$ is commonly expressed in terms of the total ft value, defined as

$$total\ ft = \frac{1}{\sum_{E_x} S_\beta(E_x)\Delta E_x} \tag{1.7}$$

1.2 Relationship between β-decay and reactor decay heat

β-strength measurements or the related β feeding distribution measurements are not just fundamental to the understanding of nuclear structure. They are also of interest in several applications[3] in particular nuclear technology. β-decay is responsible for about 8% of the energy released in a nuclear reactor during operating conditions and for essentially all the energy after shutdown. This so-called *decay heat*[4] depends on the design of the nuclear power plant and decreases as a function of time after shutdown.

Independently of which reactor system one may consider, there are a number of important design and operating criteria which require an accurate knowledge of the heat generation, from the entire reactor or from an individual fuel element, at times ranging from a few seconds to hundreds of days, and possibly years, following shutdown of the reactor. Some of those criteria where decay heat must be taken into account are[5]:

- Proper dimension/control of cooling systems: any emergency-core-cooling system must be able to remove the short-term heat generation from irradiated fuel in the reactor core.
- Shielding requirements on fuel discharge and transport routes when irradiated reactor fuel is transferred from the reactor to the chemical reprocessing plant.
- Safe storage of radioactive waste extracted from spent reactor fuel during reprocessing.

Failure to remove decay heat may cause the reactor core heat-up and possible core meltdown with the consequence of nuclear accidents, as in the nuclear accident at Three Mile Island.

1.3 Decay heat calculations

Decay heat can be determined by two methods: direct experimental measurements or theoretical calculations. Although the calculations may be preferred due to its generality, they must be verified with experimental measurements in order to ensure the reliability of the method of calculation. This is the reason why both methods are considered complementary.

Regarding the theoretical calculation method, it is based on the inventory of nuclei created during the fission process and after shutdown, and their radioactive decay characteristics. The most common method used to calculate theoretically the decay heat is

the *summation calculations*. This method consists of the summing up of the products of the activities of all fission product nuclides with the values of the mean β- and γ-ray energy released per disintegration of that nuclide at each cooling time or time following reactor shutdown. Mathematically, the decay heat is described by the following equations:

$$H_\beta(t) = \sum_i^{all\ FPs} E_\beta^i \lambda_i N_i(t) \tag{1.8}$$

$$H_\gamma(t) = \sum_i^{all\ FPs} E_\gamma^i \lambda_i N_i(t) \tag{1.9}$$

where $H_\beta(t)$ and $H_\gamma(t)$ stand for the total β and γ decay heat components respectively at a cooling time t, E_β^i and E_γ^i are the mean beta and gamma energies released respectively per disintegration of nuclide i, λ_i is the decay constant of the nuclide i and $N_i(t)$ is the number of nuclide i at the cooling time t.

The number of nuclides $N_i(t)$ at time t following shutdown can be expressed in terms of its predecessor in the decay by the equation

$$\frac{d}{dt}N_i = -\lambda_i N_i + \lambda_{i-1} N_{i-1} \tag{1.10}$$

It means that the number of nuclides once a nuclear reactor is shutdown depends on the number of nuclides that exist in operating conditions, and this number can be obtained by solving the system of equations

$$\frac{dN_i}{dt} = -(\lambda_i + \sigma_i \phi)N_i + \sum_j f_{j\to i}(\lambda_j N_j) + \sum_k g_{k\to i}(\sigma_k \phi N_k) + y_i F \tag{1.11}$$

where

N_i = Number of nuclide i
λ_i = decay constant of nuclide i
σ_i = neutron reaction cross section of nuclide i
ϕ = neutron flux
$f_{j\to i}$ = production rate of nuclide i by the unit decay of nuclide j
$g_{k\to i}$ = production rate of nuclide i by the unit neutron reaction of nuclide k
y_i = fission yield of nuclide i
F = fission rate

All this information (cross sections, fission-yields, lifetimes, mean β- and γ-energy released in the decay and n-capture cross sections) is extracted from nuclear databases. These databases must contain accurate data in order to carry out the calculations with

confidence. However, discrepancies between calculated and measured decay heat have been detected.

Many studies have been performed to find out the possible sources of the discrepancies and to test the sensitivity of summation calculations to uncertainties in the data ([6]-[9]). Thus, fission yields, neutron cross sections and decay data were evaluated concluding that the main source of discrepancies is related to the β-decay data available for many short-lived fission products.

1.3.1 Uncertainties in decay data

Many short-lived fission products are very poorly characterized because their γ-ray spectra have been incompletely measured or remain undetected. This fact is particularly true for nuclei with complicated level schemes and large Q_β windows, when the conventional high resolution γ-ray spectroscopy is used. This type of spectroscopy makes use of high resolution Germanium detectors. The determination of the β-intensity with this technique proceeds in two steps. First, the level scheme in the daughter nucleus is constructed based on the $\gamma - \gamma$ coincidence data. Secondly, the feeding intensity to each level is obtained by γ-ray intensity balance. It has been recognized[10] that this technique fails to detect the β-feeding at high excitation energies due to:

- the high fragmentation of the I_β at these energies. When the decay proceeds to highly excited levels where the level density is so high that the spectrum of levels in the nucleus could be considered almost continuous [11] the feeding probability is distributed over many levels.
- The low detection efficiency for primary high energy γ-rays. The probability that the cascade includes an energetic γ-ray which may easily escape from detection is high.
- The fact that an excited state could be de-excited through different paths.

In such a situation, feeding at high excitation energy is not observed and incorrectly assigned to low-lying levels. The experimental problem is known as the *Pandemonium effect* [12]. This effect may have direct consequences for decay heat calculations because the β-ray energy released per decay (or average β-ray energy, $\overline{E}_\beta$) may be overestimated and the γ-ray energy (or average γ-ray energy, $\overline{E}_\gamma$) may be underestimated as is shown on the right hand-side of figure (1.1).

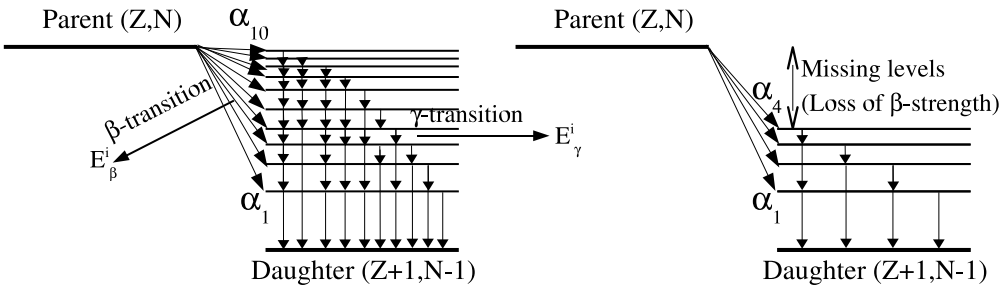

Figure 1.1: Pandemonium effect on average β- and γ-ray energies. The picture illustrates the β-decay of a nucleus to its daughter. The left-hand side corresponds to a schematic ideal case. The effects of the Pandemonium effect, is shown in the right-hand side.

1.3.2 Discrepancies in the summation calculations of fission products decay heat

The next figure, fig. (1.2)[13], shows the γ-ray decay heat component ($f(t)\ [MeV/s \cdot fission]$ multiplied by cooling time *t[s]* after a fission burst according to the usual convention in this field) as a function of time t for ^{239}Pu. Experimental data, Akiyama et al.[14] (YAYOI-reactor), Dickens *et al.*[15]-[16] (Oak Ridge National Laboratory), and Nguyen[17] (Lowell University), are compared with calculated decay heat using JNDC-FP-V2[18], JEF-2.2[19] and ENDF/B-VI[20] databases. As seen here, the calculations performed using JNDC-V2 and ENDF/B-VI underestimate the experiment in the range of 300 to 3000 seconds even though they are theoretically corrected (Gross theory[21, 26]) for the Pandemonium effect, while the curve corresponding to the European decay-data library JEF-2.2 runs far below the experiments. This is because no theoretical corrections are applied in this last library. JEF-2.2 is only based on published decay schemes except in the case of nuclides for which no experimental information is available at all, then theoretical or empirical values for the mean energies are used.

This discrepancy, called the "*γ-ray discrepancy*"[13], is thought to originate from nuclides where the measurements suffer from the Pandemonium effect and was also observed in ^{233}U, ^{235}U and ^{238}U.

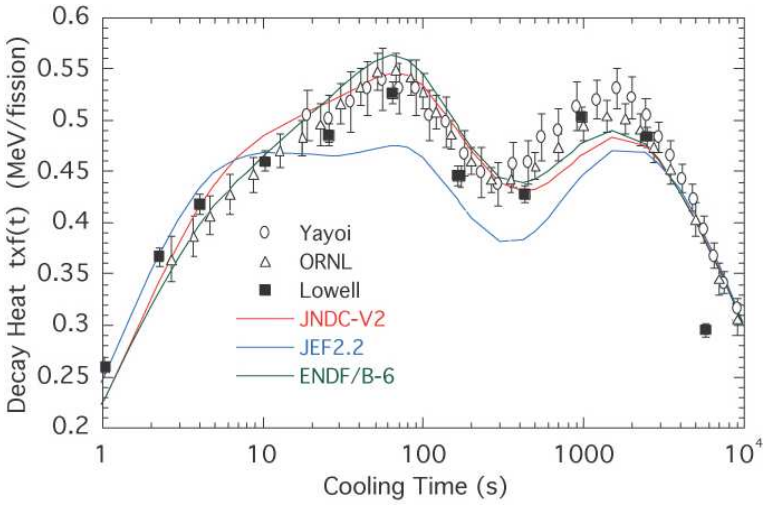

Figure 1.2: Comparison of calculated decay heat (γ-ray component) after an instantaneous fission event in ^{239}Pu with measurements carried out in different laboratories.

1.4 β-decay measurements of short-lived fission products

It has been shown that the only way to avoid the pandemonium effect is the application of the total absorption technique to β-decay studies (see for example reference [27]).

1.4.1 Total absorption γ-ray spectroscopy technique

The total absorption γ-ray spectroscopy technique is based on the detection of the sum of all the γ-ray energy produced in the de-excitation of a level fed in β-decay instead of detecting each individual γ-ray as in high resolution spectroscopy. Ideally, the energy spectrum provided by a Total Absorption Gamma-ray Spectrometer, commonly called TAGS, has sum peaks corresponding to the total energy deposited in the spectrometer by the γ-ray cascades. A schematic picture is given in figure (1.3). If we assume a simple level scheme as shown in figure (1.3), the feeding to level 2 (E_2) will produce a gamma cascade of two γ-rays, E_{γ_a} and E_{γ_b}. In this case, an ideal TAGS detector, would obtain a spectrum with a sum peak of energy E_2.

TAGS detectors are constructed with large scintillator crystals, for example of NaI(Tl) or BaF_2, that cover a solid angle of approximately 4π around the radioactive source pro-

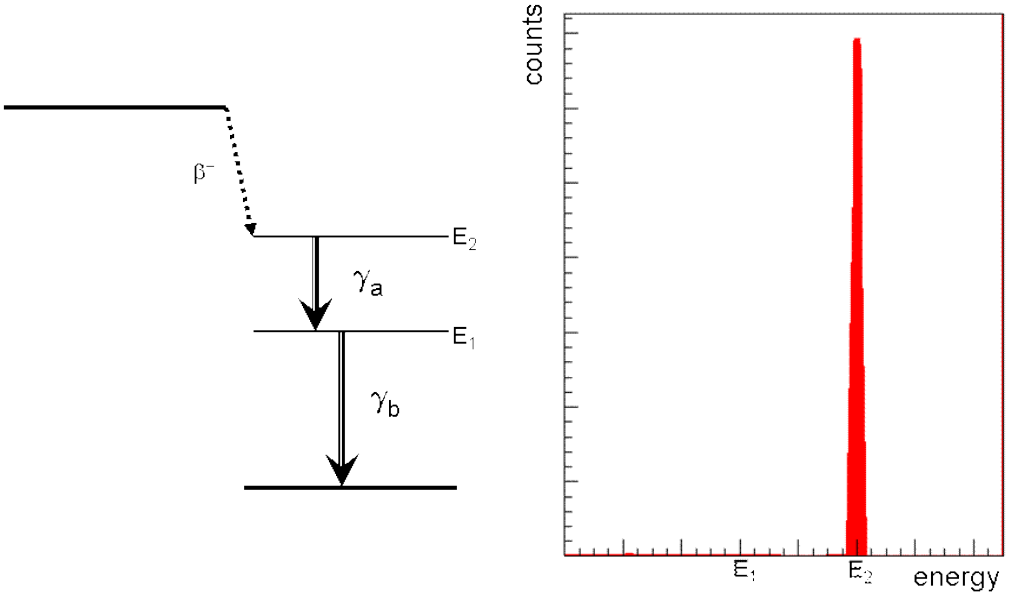

Figure 1.3: Schematic picture of a TAGS spectrum. The left side of the picture shows the β-decay scheme of a source and the right side shows its corresponding spectrum measured with a TAGS detector. In this source, only the upper level has direct feeding so the corresponding TAGS spectrum has a sum peak of energy equal to the energy of this level.

viding the spectrometer with very high efficiency for γ-ray detection. An ideal TAGS response would be independent of the γ-ray cascade pattern and, therefore, the information on the β-feeding could be extracted directly from the measured spectrum since it is proportional to the β-feeding. This implies that it has 100% full-energy peak efficiency for γ-rays of all energies.

However, a real TAGS efficiency is always lower than 100% since for practical reasons it does not fully cover a 4π solid angle. It is usually not thick enough or it is complemented by beta absorbers and ancillary detectors which causes the reduction of the TAGS γ-ray efficiency. This leads to different detector responses for different γ-ray cascade patterns depending on the γ-ray energies to be summed. The limited efficiency makes the analysis of total absorption spectra a very complex problem, since the β-intensity has to be extracted from the measured spectrum which depends on the spectrometer response.

The measured spectrum data d is related to the level feeding distribution f [28] by the equation

$$d_i = \sum_{j=1}^{j_{max}} R_{ij} f_j, \quad i = 1, i_{max} \quad or \quad \mathbf{d} = \mathbf{R} \cdot \mathbf{f} \tag{1.12}$$

where d_i represents the content of spectrum channel i, f_j represents the number of decays feeding the level labeled j, and each column j of the matrix $\mathbf{R}$ represents the average response (or normalized spectrum) of the spectrometer to the decay into the levels in the energy bin represented by the channel j. Equation (1.12) can equally represent the decay to discrete well-separated levels with j labeling their energy. The response matrix $\mathbf{R}$ depends on the emitted radiation as well as on the apparatus itself. The knowledge of $\mathbf{R}$ is a prerequisite of the analysis of TAGS spectra. This ill-posed inverse problem can be solved using appropriate deconvolution techniques such as those developed in reference [29].

Another difficulty is related to transitions between ground states. Due to the working principle of the TAGS, the $gs \longrightarrow gs$ feeding, if it exists, is more difficult to detect, since only the penetration of the betas could produce a signal in the TAGS detector. This effect reduces the sensitivity of the setup to $gs \longrightarrow gs$ transitions.

Determination of the average energies with a TAGS detector

The average β- and γ-ray energies can be calculated by using the β-feeding intensities. The equations that must be evaluated are:

$$\overline{E}_\beta = \sum_i I_\beta(E_i) \frac{f_\beta(Q_\beta - E_i)}{f(Q_\beta - E_i)} \tag{1.13}$$

$$\overline{E}_\gamma = \sum_i I_\beta(E_i) E_i \tag{1.14}$$

where $f_\beta(Q_\beta - E_i)$ is the average energy of the β continuum corresponding to the excited level E_i and $f(Q_\beta - E_i)$ is the normalization which coincides with the integrated Fermi function:

$$f_\beta(Q_\beta - E_i) = \int_1^{\frac{Q_\beta - E_i}{mc^2}+1} mc^2(\varepsilon - 1)\varepsilon\sqrt{\varepsilon^2 - 1}\Big(\frac{Q_\beta - E_i}{mc^2} + 1 - \varepsilon\Big)^2 F(Z,\varepsilon)d\varepsilon \tag{1.15}$$

$$f(Q_\beta - E_i) = \int_1^{\frac{Q_\beta - E_i}{mc^2}+1} \varepsilon\sqrt{\varepsilon^2 - 1}\Big(\frac{Q_\beta - E_i}{mc^2} + 1 - \varepsilon\Big)^2 F(Z,\varepsilon)d\varepsilon \tag{1.16}$$

$$\varepsilon = \frac{E_\beta}{mc^2} + 1 \tag{1.17}$$

with E_β the kinetic energy of the β-particle, E_i is the energy of the i-th level in the daughter nucleus, m is the electron rest mass, Z is the proton number of the daughter nucleus and F is the Fermi function. For simplicity, we assume that all transitions are of allowed type.

1.4.2 Application of the TAGS technique to the decay heat problem

The TAGS technique was applied successfully by Greenwood *et al.*[31] at the INEL[1] on-line mass separator at Idaho Falls (EEUU). Greenwood measured the β-feeding as a function of the excitation energy of the daughter nuclide for 45 isotopes of 12 fission products elements: Rb, Sr, Y, Cs, Ba, La, Ce, Pr, Nd, Pm, Sm and Eu. These data were included in JEFF-3.1, the last version of the European data library, and JENDL, the current name of the Japanese data file (JNDC FP Decay Data File), and their effect was studied by Yoshida and coworkers[30]. The effect of the inclusion of these data in the databases can be seen in figure (1.4).

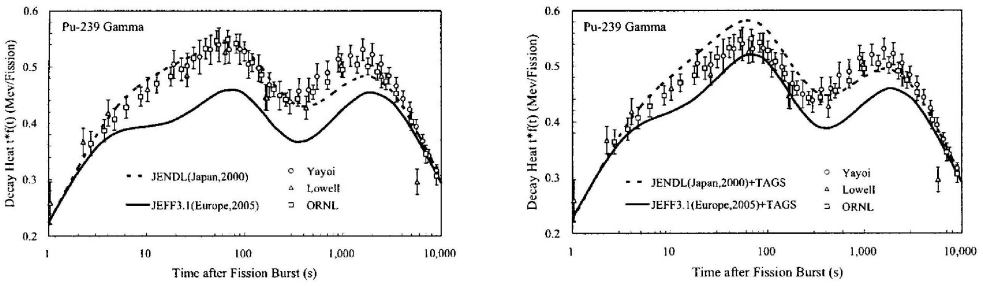

Figure 1.4: The left hand figure corresponds to the γ-ray component of decay heat after a fission burst in ^{239}Pu before the total absorption γ-ray spectroscopy (TAGS) correction. The right hand figure is exactly the same but after the TAGS correction.

After the inclusion of TAGS data, the JEFF-3.1 curve was pulled up, improving the agreement obtained for this database, but the results using JENDL, which are also pulled up, deviate from the integral measurement at low cooling times. The differences between the results from the two databases can be understood if we keep in mind that

[1]The word INEL stands for the acronym of Idaho National Engineering Laboratory.

JENDL includes experimental data complemented with theoretical calculations (Gross Theory) in cases where the experimental information is believed to be incomplete, and JEFF-3-1 only uses experimental data.

In order to have a deeper understanding of the cause of the large discrepancies, Yoshida and collaborators identified the nuclides that contribute more to the differences between the two databases after the introduction of the TAGS data and which are possible candidates to be measured using the TAGS technique. For example, they decided that ^{102}Tc, ^{103}Mo, ^{105}Mo and ^{139}Xe are large contributors to the differences.

1.4.3 Proposed TAGS measurements

Taking all this information as their starting point, Yoshida and coworkers[2] made a high priority request list of nuclei responsible for the discrepancy that should be measured using the TAGS technique. They selected fission product nuclei using the following three criteria:

- its contribution to the difference between JENDL and JEFF-3.1 is more than 1% of the total fractional difference in the β- and γ-ray component of the decay heat after a fission burst in ^{235}U and ^{239}Pu,
- they are large contributors to the decay heat themselves, and
- the highest known level is lower than 70% of the decay Q value, which is a clear indication that the available decay data may suffer from the Pandemonium effect.

Table (1.1) corresponds to the last version of this high priority request list. The nuclei are classified depending on its priority (1 means high priority and 3 lower priority). Some additional data is given in the last column of this table for several nuclei. This table also contains some radionuclides, measured at the INEL on-line mass separator by Greenwood *et al.*, whose data analysis methods require comparison with the new ones.

[2] Work done in the framework of the WPEC, Working Part on International Evaluation Cooperation of the NEA Nuclear Science Committee.

radionuclide	priority	Q_β (keV)	Half-life	Comments
$^{86}_{35}Br$	1	7626 (11)	55.1 s	
$^{87}_{35}Br$	1	6852 (18)	55.65 s	Extremely complex decay scheme with substantial gamma component; large uncertainties in the mean gamma energy arises from significant disagreements between the various discrete γ-ray measurements. Also (β^-, n) branch.
$^{88}_{35}Br$	1	8960 (40)	16.36 s	(β^-, n) branch.
$^{89}_{36}Kr$	1	4990 (50)	3.15 min	Incomplete decay scheme.
$^{90}_{36}Kr$	1	4392 (17)	32.32 s	Incomplete decay scheme.
$^{90m}_{37}Rb$	2	6690 (15)	258 s	Repeat of INEL TAGS measurement; data check.
$^{92}_{37}Rb$	2	8096 (6)	4.49 s	Small (β^-, n) branch.
$^{89}_{38}Sr$	2	1493 (3)	50.53 d	
$^{97}_{38}Sr$	2	7470 (16)	0.429 s	Extremely short half-life and possible (β^-, n) branch.
$^{96}_{39}Y$	2	7096 (23)	5.34 s	
$^{99}_{40}Zr$	3	4558 (15)	2.1 s	
$^{100}_{40}Zr$	2	3335 (25)	7.1 s	
$^{98}_{41}Nb$	1	4583 (5)	2.86 s	
$^{99}_{41}Nb$	1	3639 (13)	15.0 s	
$^{100}_{41}Nb$	1	6245 (25)	1.5 s	
$^{101}_{41}Nb$	1	4569 (18)	7.1 s	
$^{102}_{41}Nb$	2	7210 (40)	1.3 s	
$^{103}_{42}Mo$	1	3750 (60)	67.5 s	
$^{105}_{42}Mo$	1	4950 (50)	35.6 s	
$^{102}_{43}Tc$	1	4532 (9)	5.28 s	
$^{103}_{43}Tc$	1	2662 (10)	54.2 s	
$^{104}_{43}Tc$	1	5600 (50)	18.3 min	
$^{105}_{43}Tc$	1	3640 (60)	7.6 min	
$^{106}_{43}Tc$	1	6547 (11)	35.6 s	
$^{107}_{43}Tc$	2	4820 (90)	21.2 s	
$^{132}_{51}Sb$	1	5509 (14)	2.79 min	
$^{135}_{52}Te$	2	5960 (90)	19.0 s	
$^{136}_{53}I$	1	6930 (50)	83.4 s	Incomplete decay scheme.
$^{136m}_{53}I$	1	7580 (120)	46.9 s	
$^{137}_{53}I$	1	5877 (27)	24.13 s	(β^-, n) branch.

$^{137}_{54}Xe$	1	4166 (7)	3.82 min	Incomplete decay scheme.
$^{139}_{54}Xe$	1	5057 (21)	39.68 s	
$^{140}_{54}Xe$	1	4060 (60)	13.6 s	
$^{142}_{55}Cs$	3	7308 (11)	1.69 s	(β^-, n) branch.
$^{145}_{56}Ba$	2	5570 (110)	4.31 s	Repeat of INEL TAGS measurement; data check.
$^{143}_{57}La$	2	3425 (15)	14.2 min	Repeat of INEL TAGS measurement; data check.
$^{145}_{57}La$	2	4110 (80)	24.8 s	Repeat of INEL TAGS measurement; data check.

Table 1.1: High priority request list for TAGS measurements.

1.5 Motivation of this work

Motivated by the fact that several Technetium isotopes were identified as possible important contributors to the differences between experimental data and calculations in the decay heat γ-ray component and considering the good results obtained in other experiments performed at GSI and ISOLDE with the total absorption technique[32, 37], we decided to measure the β-decay of ^{101}Nb, ^{102}Tc, ^{104}Tc, ^{105}Tc, ^{105}Mo, ^{106}Tc and ^{107}Tc[3] using this technique. These isotopes were selected from the high priority request list because their decays presumably suffer from the Pandemonium effect and they are considered good candidates for measurement using the TAGS technique. It was expected that the study of these nuclides with a total absorption γ-ray spectrometer would improve the overall prediction power of the summation calculations and thus provide a better understanding of the decay heat problem. Thus, the goal is to measure the β-decay of all these nuclei in order to obtain experimental data for the average β- and γ-ray energies free of the Pandemonium effect. Then the data could be used for the summation calculations and assess the impact of these nuclides in the decay heat.

On the other hand, there is a second reason why we are interested in the measurement of those isotopes. This reason is related with the more fundamental problem of understanding the structure of atomic nuclei. The β-strength distribution is sensitive to small components of the wave functions as well as to the global shape of the nucleus which may be of interest in this region of the nuclide chart, where the co-existence of different nuclear shapes has been confirmed[38].

[3] All of them have priority 1 in the high priority list except the ^{107}Tc which has priority 2.

2 The experiment

2.1 The IGISOL facility

An important question is where to measure the selected isotopes. We cannot use a conventional ion source because the elements of the isotopes of interest are refractory. We need to produce them with a technique where no ion source in the classical sense is used. This is the reason why we have performed the experiment at the Ion Guide Isotope Separator On-Line (IGISOL)[39] facility of the University of Jyväskylä (Finland). At this facility low-energy radioactive ion beams of exotic nuclei are produced using the ISOL technique. In this technique, a target is bombarded with particles from an accelerator. The reaction products are stopped, ionized and accelerated with electric fields to a few tens of keV, and are then mass separated with a magnetic field. The target in which the reactions take place is usually an integral part of the ion source and can be either thick, when it acts as a catcher material, or thin, in which case it is followed by a separate solid or gaseous catcher.

Refractory elements cannot be produced using thick targets due to their high boiling points, but it is possible with thin targets such as the ones used at the IGISOL facility. Figure (2.1) shows the current layout of the IGISOL facility. The different components of the facility are labeled with numbers. In the following sections some of them will be described in more detail.

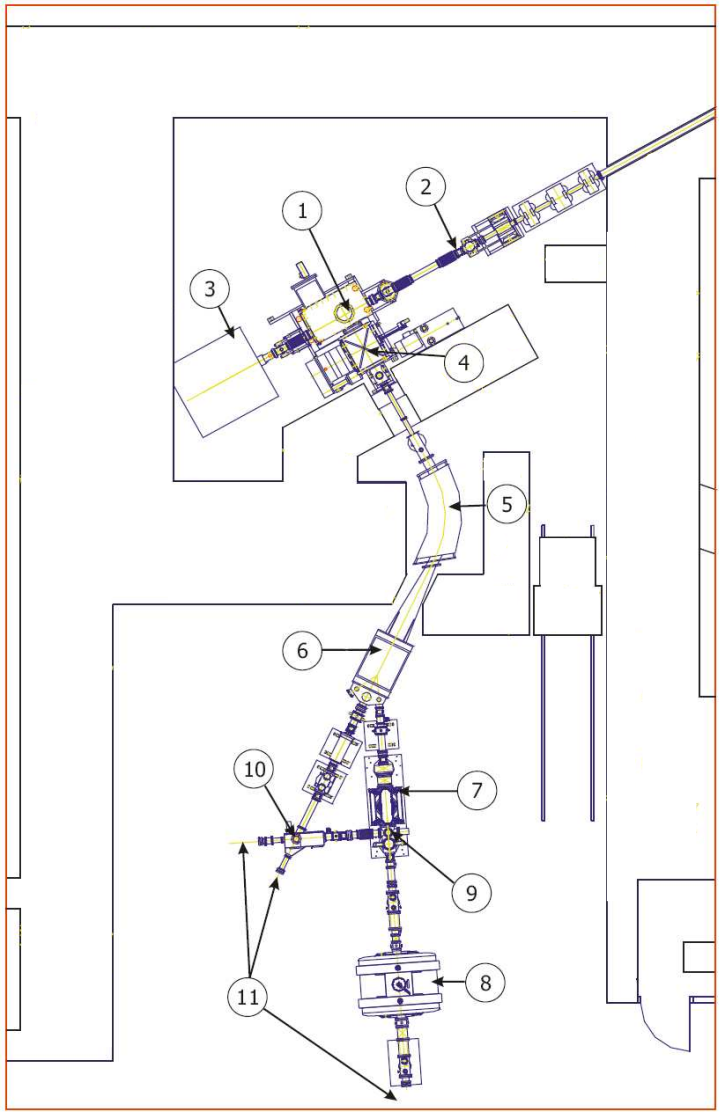

Figure 2.1: Layout of the IGISOL facility. In this picture, the labeled parts are: 1) Ion guide; 2) K130 cyclotron beamline; 3) beam dump; 4) acceleration chamber; 5) dipole magnet; 6) Switchyard; 7) RFQ cooler; 8) tandem Penning trap; 9) miniquadrupole deflector; 10) electrostatic deflector and beamline to upstairs; and 11) experimental setups.

2.1.1 The ion guide isotope separator

In the ion guide technique a primary ion beam from the JYFL K130 cyclotron is directed onto a thin target foil. Usually the beam consists of protons with an energy of 15-35 MeV hitting a thin Uranium target to produce fission fragments. Most of the fragments are produced initially at high energy and in high charge states. The reaction products are stopped in Helium gas at a pressure of about 100-300 mbar and the charge state of these ions gradually decreases due to charge exchange processes with the gas. Finally, a considerable portion of the reaction products is thermalized in the buffer gas as singly charged ions. These ions are then swept out through an exit nozzle to an adjacent vacuum chamber by gas flow. When the ions exit the ion guide they are guided through a hole in a skimmer electrode with an electric field whereas the neutral buffer gas is mostly pumped away. The ions are further accelerated to 30-40 keV energy and are sent into the separating magnet. A schematic view of the ion guide principle can be seen in figure (2.2).

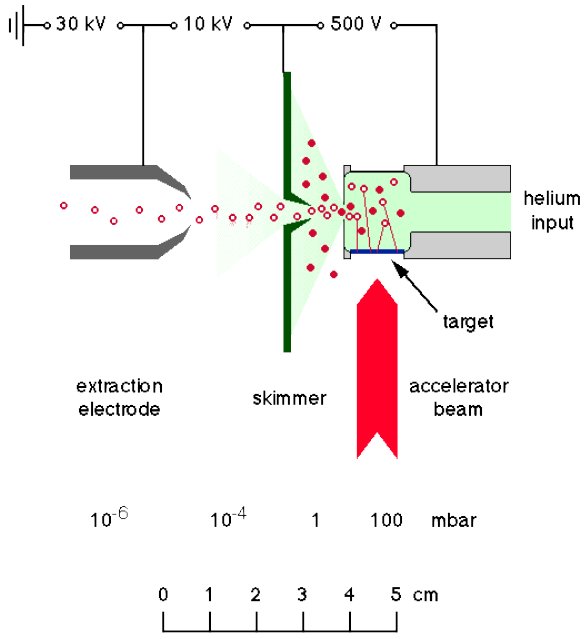

Figure 2.2: Ion guide principle.

There are three ion guides available, depending on the nuclear reaction needed to

produce the desired reaction products: the light-ion ion guide, the HIGISOL heavy-ion ion guide and the fission ion guide. The one used in the present experiment is the fission ion guide (figure (2.3)). This ion guide is used to produce neutron-rich isotopes by proton- or neutron- induced fission of Uranium or Thorium. The resulting ions cover a large mass range due to the asymmetric fission of Uranium. The target is placed outside the stopping volume at an angle of 7° with respect to the beam, leading to a larger effective thickness.

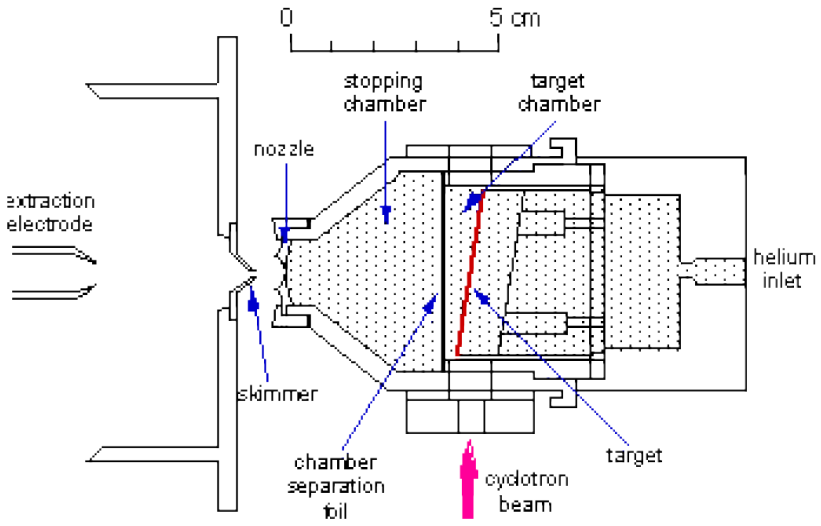

Figure 2.3: Fission ion guide.

The mass separation is carried out with a dipole magnet that has a tilted exit face for vertical beam focusing. Its typical mass resolving power, $R = M/\delta M$, is below 500, however, it is sufficient to select a single mass number. The mass resolving power depends on the front-end parameters in such a way that when a higher energy spread[1] is introduced to the beam due to increased cell pressure or higher electric fields used for extracting the ions, the mass resolving power decreases. On the other hand, the overall yield is generally directly proportional to these two parameters. Therefore, yield optimization has to be carried out at the cost of the mass resolving power or vice versa.

[1] A real ion beam has always some energy spread and thus there are some ions in the beam that go faster and some that go slower than average ions. If ions are traversing over long distances, their energy spread can introduce large differences in the ions time-of-flight which in some applications may lead to difficulties.

A beam switchyard equipped with a Faraday cup and a silicon detector for beam diagnostics is located at the separator focal line. The separated beam can then be sent either straight to the central beam line or electrostatically deflected by 30° toward the trap beam line.

2.1.2 JYFLTRAP

The JYFLTRAP[40] system is a combination of a gas filled radio-frequency quadrupole (RFQ) for beam cooling and bunching, and a double Penning trap for beam purification and precision mass measurements. A schematic layout of this device is illustrated in figure (2.4).

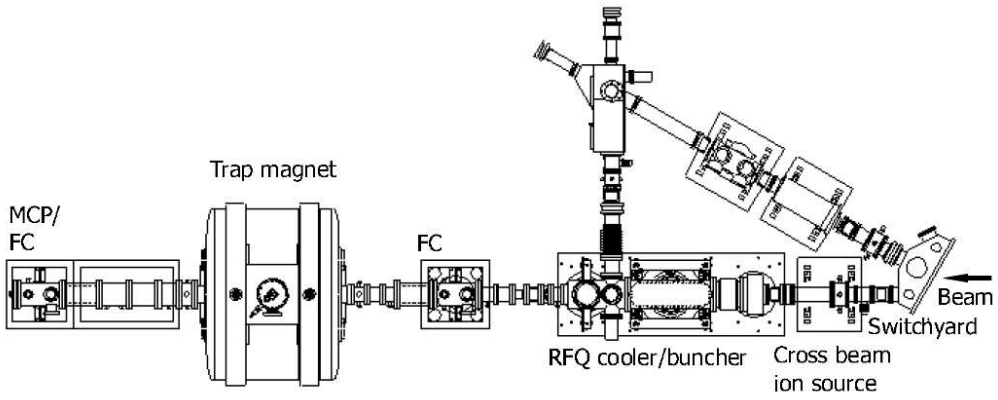

Figure 2.4: Experimental setup of JYFLTRAP.

Radio-frequency quadrupole cooler

The RFQ cooler accepts the low quality ion beam and confines it in the radial direction with oscillating electric fields. This structure is filled with a low pressure Helium buffer gas in which the injected ions are thermalized. The ions are guided to the extraction end of the structure with a DC potential and the beam is bunched by applying a pulsed voltage to the end plate electrode and accumulating ions in a potential well created by the DC fields. The ions are subsequently released in short bunches when the wall is lowered. The availability of a bunched beam enables an efficient dynamic trapping scheme to be used for injection into the Penning trap.

Penning trap system

The Penning trap is an electromagnetic trap that confines charged particles by means of the combination of a strong magnetic field (radial confinement), and a electric quadrupole field (axial confinement). The electric quadrupole field can be created using a set of three electrodes: a ring and two endcaps. The most common structures used are hyperbolical and cylindrical. The hyperbolical structure has the advantage of a very precise field geometry, whereas the cylindrical structure is a more open construction and simplifies the injection of ions or buffer gas into the trap. Otherwise, the motion of the charged particles in the trap can be described in the same way in both structures.

Let us consider a particle of charge q and mass m. In the axial direction, the particle undergoes a harmonic oscillation in a harmonic electric potential, so its angular frequency will be given by equation (2.1):

$$\omega_Z = \sqrt{\frac{qV_0}{md^2}} \tag{2.1}$$

where V_0 is the potential difference between the endcap and the ring electrodes, and d is the characteristic trap dimension

$$4d^2 = r_0^2 + 2z_0^2$$

that depends on the inner radius of the ring electrode, r_0, and the spacing between the endcap electrodes, $2z_0$.

In the radial plane, there are two circular motions around the magnetic field lines called reduced cyclotron motion and magnetron motion. The sum of these frequencies is the true cyclotron frequency, which is related to the mass and charge of the particle, and to the magnetic field by

$$\omega_C = \omega_+ + \omega_- = \frac{q}{m}B \tag{2.2}$$

Each motion has associated a frequency given by

$$\textit{reduced cyclotron frequency} \qquad \omega_+ = \frac{1}{2}\left\{\omega_C + \sqrt{\left(\omega_C^2 - 2\omega_Z^2\right)}\right\} \tag{2.3}$$

$$\textit{magnetron frequency} \qquad \omega_- = \frac{1}{2}\left\{\omega_C - \sqrt{\left(\omega_C^2 - 2\omega_Z^2\right)}\right\} \tag{2.4}$$

being the magnetron motion almost mass independent. In a first order polynomial approximation, it can be written as

$$\omega_- \approx \frac{V_0}{2Bd^2} \tag{2.5}$$

The three motion frequencies are

$$\omega_+ \gg \omega_Z \gg \omega_-$$

and satisfy the so-called invariance theorem[41]

$$\omega_+^2 + \omega_-^2 + \omega_Z^2 = \omega_C^2 \tag{2.6}$$

The three superposed motions of a charged particle in the trap are shown in figure (2.5).

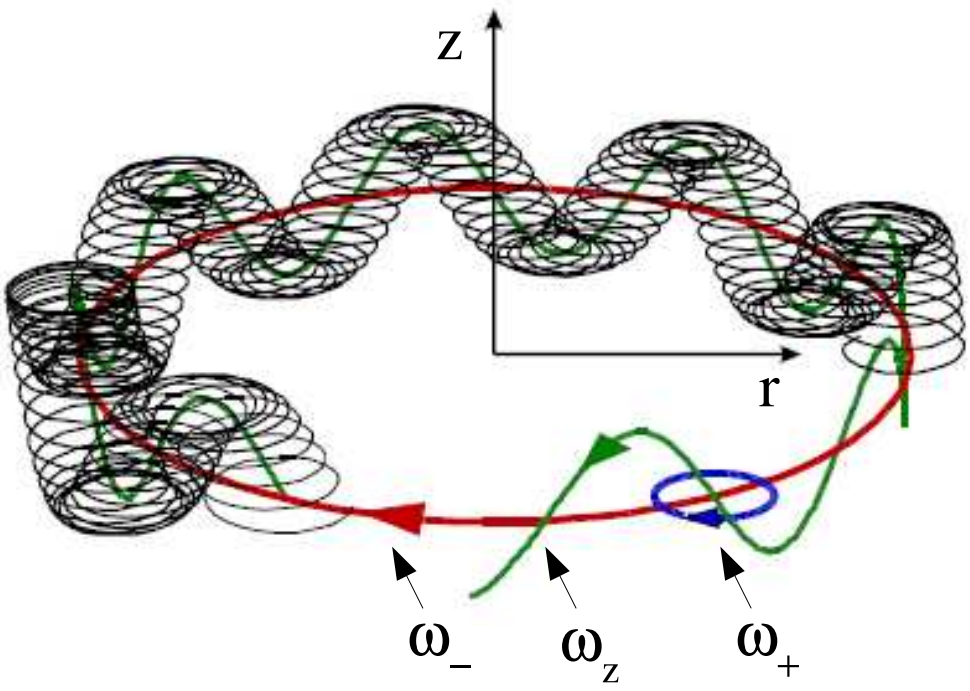

Figure 2.5: Motion of an ion in the Penning trap. ω_z is the axial motion, ω_- is the magnetron motion and ω_+ is the reduced cyclotron motion.

The Penning trap at the IGISOL facility consists of two cylindrical Penning traps housed in the warm bore of a superconducting 7 T magnet. The magnet has two homogeneous field regions of 1 cm^3 each. Placing both traps in the same magnet avoids the problem of having to transport the ions through strong magnetic field gradients between the traps. The disadvantage, however, is that no pumping is possible between the traps, and the pressure, especially in the precision trap, is harder to control. The whole trap is kept on a high voltage (HV) platform to decelerate the incoming beam from 30 keV to $\approx$ 100 eV.

The first trap is used for isobaric mass separation. Due to imperfections in the magnetic and electric fields the relation $\omega_C = \omega_+ + \omega_-$ might be not exactly fullfilled. The frequency shifts depend on the amplitudes of the ion motions, then, it is very important to decrease their motional amplitude. In order to achieve that, the ions are cooled injecting helium buffer gas in the trap. As a result of the collisions with the gas atoms, the ions lose kinetic energy and thus the reduced cyclotron motion is cooled down whereas the magnetron amplitude increases[42]. The next step is to increase the diameter of the magnetron orbit of all the ions to more than 2 mm, which is the diameter of the extraction aperture. It can be done with an electric dipole field at the magnetron frequency with the correct amplitude and duration[2]. Once it is achieved, a radio frequency quadrupole electric field is introduced. This quadrupole field, in resonance with the cyclotron frequency ω_C, leads to a coupling of the reduced cyclotron and magnetron motions. In this way, an initial pure magnetron motion can be converted into a pure reduced cyclotron motion (and viceversa) choosing properly the field amplitude and the duration of the excitation. At this point, ions have only magnetron motion so the excitation will convert the magnetron motion to the reduced cyclotron motion. The converted reduced cyclotron motion is cooled away due to the buffer gas, leading to a centering of the ions. This centering is mass selective due to mass dependence of the cyclotron frequency. When the ions are ready to be extracted, only the centered ones can pass. With this method, a mass resolving power of 10^4 to 10^6 is obtained, which is sufficient for isobaric purification.

Figures (2.6) and (2.7) show the isobaric resolving power of the Penning trap system during our experiment. The first picture corresponds to the mass 101 and the second to the mass 105. As can be seen in these two pictures, the different isotopes are labeled and the corresponding peaks are well separated in frequency, allowing the extraction of beams of high purity.

[2]An electric dipole excitation with the proper frequency can change the amplitude of the motion. In this case, if the electric dipole excitation has a frequency equal to the magnetron frequency, it will increase the radius of all the ions in the trap since the magnetron frequency is almost mass independent (equation (2.5)).

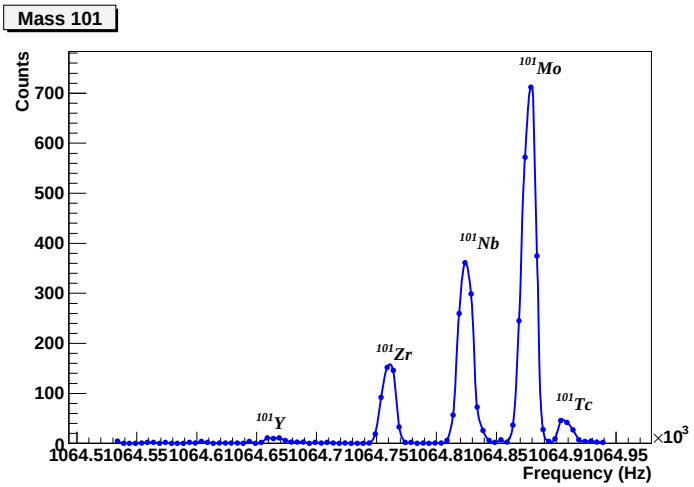

Figure 2.6: Mass scan obtained with the Penning trap corresponding to the mass 101 in our experiment.

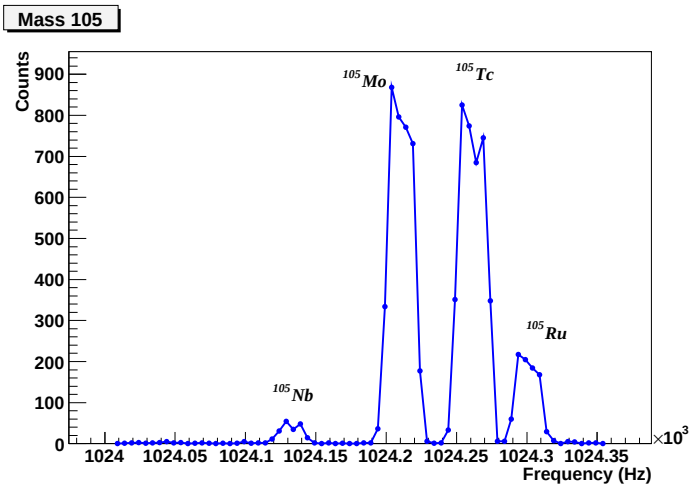

Figure 2.7: Mass scan obtained with the Penning trap corresponding to the mass 105 in our experiment.

The second trap is used for precision mass measurements and it can be also used for separation of isomers. This trap is operated in vacuum so the ions' motion is not cooled. The ion mass determination is based on the mass dependence of the cyclotron frequency[43]. In particular, it is based on the measurement of the ratio of the cyclotron frequencies between the ion of interest, ω_C^{meas}, and a reference ion, ω_C^{ref}, since

$$\frac{\omega_C^{ref}}{\omega_C^{meas}} = \frac{m_{meas} - m_e}{m_{ref} - m_e} \tag{2.7}$$

where m_{meas} is the mass we want to measure, m_{ref} is the mass of the reference atom and m_e is the electron mass. Rewriting equation (2.7) we obtain

$$m_{meas} = \frac{\omega_C^{ref}}{\omega_C^{meas}}(m_{ref} - m_e) + m_e \tag{2.8}$$

The determination of the cyclotron frequency for the ions of interest is done using the time of flight technique[44]. In order to use it, the ions are firstly moved to a well-defined radius. It is done with a dipole excitation at the magnetron frequency. Then, with a quadrupole field the magnetron motion is converted into reduced cyclotron motion for those ions whose cyclotron frequency is in resonance with the excitation energy. Ions in purely cyclotron motion have more radial kinetic energy than ions in purely magnetron motion due to $\omega_+ \gg \omega_-$ and the radial kinetic energy is propotional to the square of the velocity. After the quadrupole excitation, the ions are extracted from the trap to a time of flight detector. The ions, in their way to the time-of-flight detector, feel an axial force due to the interaction of their magnetic moment with the gradient of the magnetic field. Since the ions with more reduced cyclotron motion will be more accelerated due to the energy difference between both radial motions, they will reach the detector earlier. The time of flight of the ions can be calculated with equation (2.9)

$$T(\omega_{rf}) = \int_{z_0}^{z_1} \sqrt{\frac{m}{2[E_0 - q \cdot V(z) - \mu(\omega_{rf}) \cdot B(z)]}} dz \tag{2.9}$$

where E_0 is the total initial energy of the ion, *V(z)* and *B(z)* are the electric and magnetic fields along the ion path from the trap (z_0) to the detector (z_1). Trying different quadrupole excitation energies a time of flight spectrum can be obtained. Once the cyclotron frequency has been determined, the desired ion mass can be calculated using equation (2.8). This method allows the measurement of unknown masses with a precision better than 10 keV for A=100 ions[45] and further purification for trap assisted spectroscopy experiments. In our experiment in particular the second trap was not used.

2.2 Experimental setup

The experimental setup used for the measurements is shown in picture (2.8). It consisted of a germanium detector, a total absorption γ-ray spectrometer (TAGS) and a silicon detector. In our setup, the Ge detector was used to monitor the quality of the sources. The purity of the samples is of great importance in TAGS measurements due to the fact that a TAGS is a high efficiency device but with pour resolution compared with a high resolution setup (Ge detector).

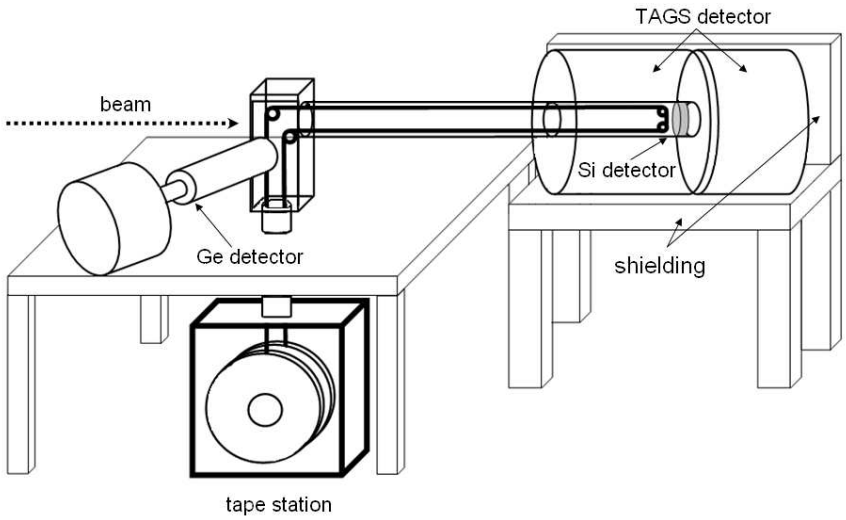

Figure 2.8: Experimental setup used in our measurements. A germanium detector monitorizes the composition of the source at the implantation point. The source is implanted in a tape and transported through an Aluminium tube to the centre of the TAGS. The TAGS detector is shielded with lead to reduce the background. A silicon detector is coupled to the end of the Aluminium tube.

In order to measure the sources properly with the total absorption spectrometer, the sources are first implanted onto a tape, and after a given collection time, they are transported inside the TAGS detector through a tube of Aluminium (the complete composition is AlMgSi) which forms part of the tape transport system. The processes of implantation and transport are done in high vacuum. In our case, the vacuum was very stable during all the experiment being about $6 \cdot 10^{-5}$ mbar. The measurements were performed using symmetrical collection/measuring times ($t_{coll} = t_{cycle}$). The cycles were usually taken as $1.6 \times T_{1/2}$ of the source under study see table (2.1). After the comple-

tion of a cycle, the tape moves replacing the old source with a new one. The collection and measuring cycles are established and controlled with the tape control station. The station also controls the rewind of the tape when it is necessary. The TAGS detector was partly covered by lead shielding to reduce the impact of background radioactivity (this will be explained in more detail in the next chapter).

The silicon detector is used for the detection of the β-particles produced in the β-decay of the sources of interest. The dimensions of the Si detector are $\oslash = 23$ mm $\times l = 0.85$ mm. It is placed inside the TAGS detector as can be seen in the figure (2.8). The measuring point is positioned in front of the Silicon detector and in the "centre" of the TAGS detector. For more details see figure (2.9).

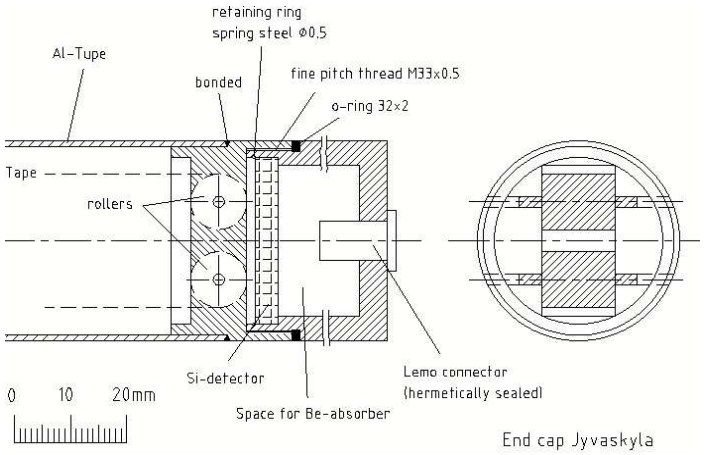

Figure 2.9: Aluminium tube and silicon detector coupling. The picture also shows the different pieces needed for the coupling as well as the rollers inside the Aluminium tube. The right hand side corresponds to a frontal view of the rollers in the Aluminium tube.

The full setup, which was mounted in the experimental hall of IGISOL, is shown in figure (2.10) from a top view. In this photograph we can distinguish two of the three detectors used in the experiment. The Ge detector at the right hand side of the picture just in front of the implantation point and the TAGS detector. In the left hand side the tape control station can be seen. The controller sets the number of steps of the step motor to define the length of the movement of the tape. The movement of the tape is triggered by means of an external logical signal which has $1/t_{cycle}$ frequency.

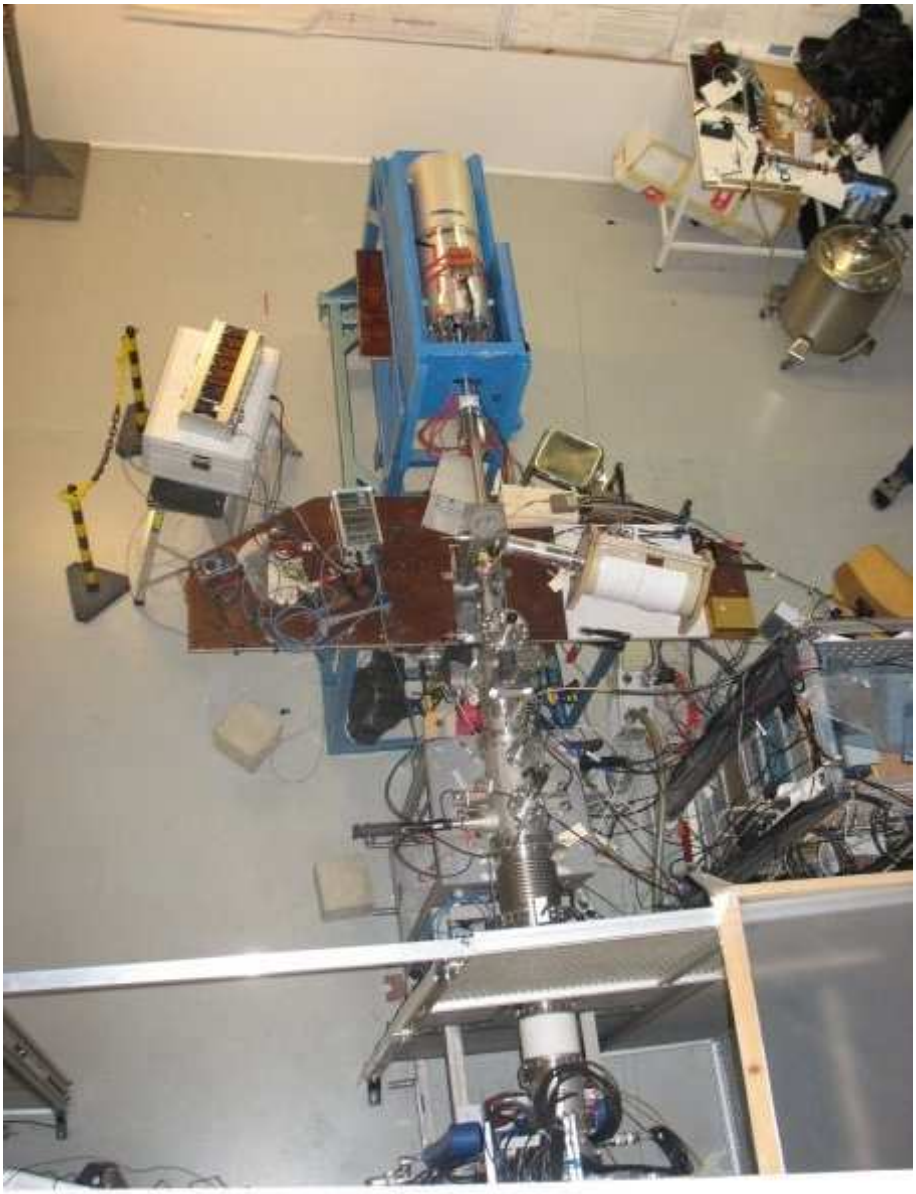

Figure 2.10: Photograph of the experimental setup used in the experiment from the top. In this photograph we can distinguish two of the three detectors used in the experiment: 1) the germanium detector and 2) the TAGS detector. The silicon detector is inside the TAGS.

2.2.1 The TAGS detector

The TAGS detector used in this experiment was designed at the Nuclear Institute of Saint Petersburg. It has been used previously in other experiments[46]. It consists of two NaI(Tl) cylindrical crystals. The dimensions of each crystal are: the larger one has a diameter of 200 mm and a length of 200 mm, and the smaller has a diameter of 200 mm and a length of 100 mm. The big crystal also has a longitudinal hole of $\oslash = 43$ mm[47]. The scintillation light of the big crystal is collected by five photomultiplier tubes arranged surrounding the longitudinal hole (figure (2.11)) and for the smaller NaI(Tl) crystal only one photomultiplier tube is used.

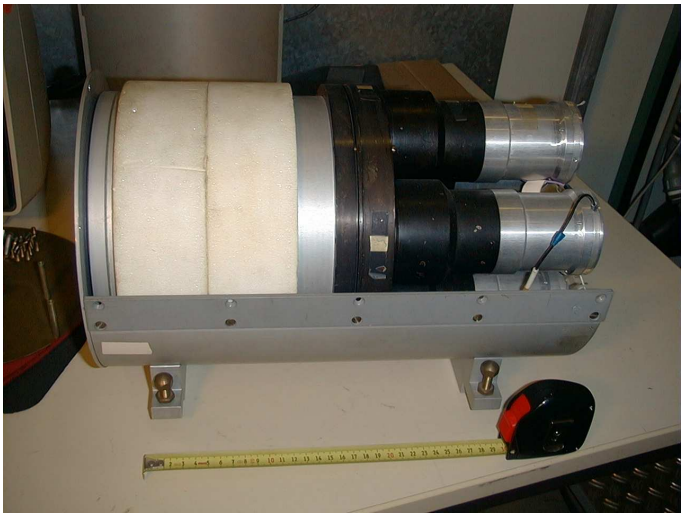

Figure 2.11: Photo of the larger NaI(Tl) crystal of the TAGS detector. This part of the detector has a longitudinal hole of $\oslash = 43$ mm.

The detector geometry has been implemented as precisely as possible in a Monte Carlo code. As will be explained in section 3.4, an accurate Monte Carlo simulation of the response of the spectrometer to γ-rays and β-particles is a prerequisite for the analysis of TAGS data. A good description of the geometry is obtained with Geant4[48], version geant4.9.0.p01 (figure (2.12)). Figure (a) shows the complete geometry: the two NaI(Tl) crystals with their canning of Aluminium, the Si detector and part of the tape transport system as a section of the Aluminium tube, the rollers and the coupling of Si detector and the Aluminium tube. More details of this coupling are given in the figure (b). We can also distinguish the rollers, all the screws used for holding the rollers and also the Si frame, the Si detector support, the spacers and the lemo connector.

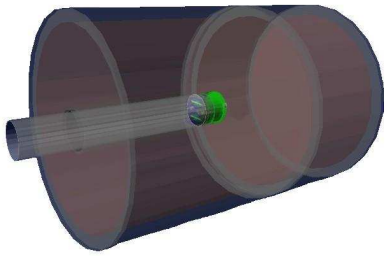

(a) Simulation of the geometry of the whole TAGS detector system.

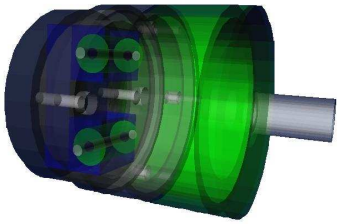

(b) Some details of the Si detector and the rollers.

Figure 2.12: Simulation of the geometry with Geant4. The full TAGS setup can be seen in figure (a). Figure (b) corresponds to a more detailed description of the pieces inside the TAGS detector.

The total and photopeak efficiencies of the TAGS for γ-rays have been calculated using the geometry implemented in full detail. The results can be seen in figure (2.13). This specific detector has a high total efficiency but a relatively small photopeak efficiency compared with other TAGS detectors (see for example LUCRECIA (CERN)[49]) due to its smaller dimensions. At 5 MeV the total efficiency is estimated to be 70%, although the photopeak efficiency is close to 25%.

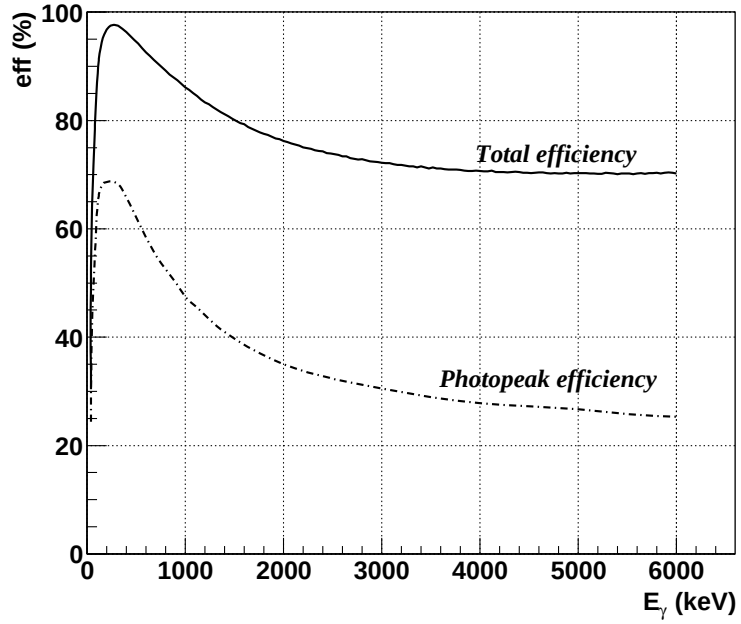

Figure 2.13: Total and photopeak efficiencies of the TAGS detector for different γ-ray energies.

2.3 Experimental measurements

The experiment took place in February of 2007. A proton beam of 50 MeV delivered by the K130 cyclotron of the Jyväskylä University was used to produce fission in a natural Uranium target. The thickness and dimensions of the target were 15 mg/cm^2 and 10×50 mm^2, respectively, tilted at 7 degrees to the beam direction. Typical currents were about 4 μA. The separated activity produced by the IGISOL facility after purification in the Penning trap (JYFLTRAP), was implanted on a tape and carried inside the total absorption spectrometer by the tape transport system described earlier.

In this way, the isotopes produced were (in order of measurement): ^{105}Mo, ^{105}Tc, ^{102}Mo, ^{102}Tc, ^{101}Nb, ^{101}Mo, ^{104}Tc, ^{107}Tc, ^{107}Ru and ^{106}Tc. Some isotopes, such as ^{102}Mo, ^{101}Mo and ^{107}Ru, do not belong to the high priority list introduced in the previous chapter but they were also measured as possible contaminants in the measurements of ^{102}Tc, ^{101}Nb and ^{107}Tc, respectively.

The most challenging and at the same time most interesting nucleus of those mentioned above is ^{102}Tc. This nucleus has a small production yield in comparison with other isotopes studied[50] and it can not be cleanly separated from its parent nucleus, ^{102}Mo, using the Penning trap[3]. In this case, the way to overcome the problem was to perform two kinds of measurement:

1. Measure the ^{102}Tc decay directly using different collection/measurement cycles to separate the ^{102}Mo contamination and the two ^{102}Tc decaying isomers.

2. To produce ^{102}Tc through the decay of ^{102}Mo.

Both methods have advantages and disadvantages. The first method has the advantage of obtaining clean ^{102}Tc decay spectra, free of ^{102}Mo contamination, but it has the disadvantage of the very low production yield for ^{102}Tc. Table (2.1) summarizes the counting rate obtained for each isotope and the cycle used. For ^{102}Tc the counting rate (1754 counts/s) is very close to the background counting rate (1750 counts/s). The advantage of the second method is the higher production yield of ^{102}Mo in comparison with ^{102}Tc. However, the problem with this method is the additional contamination introduced by ^{102}Mo decay. Despite this problem, the second method was considered the better solution for producing ^{102}Tc.

^{101}Mo was measured as a possible contaminant of ^{101}Nb. The production rate was very low. Anyway, the possibility of daughter activity contamination was not considered to be a problem in the case of the ^{101}Nb decay.

After five working days, the proton beam energy was changed from 50 MeV to 30 MeV in order to increase the production of some isotopes: ^{107}Tc, ^{107}Ru and ^{106}Tc. About 30% of the approved beam time of the experiment was used for measuring background in the same conditions of the measurements. The background had a counting rate of 1750 counts per second and remained stable during the whole experiment. The rest of the time was dedicated to source measurements and calibrations. The calibrations were performed before, during and after the experiment. A more detailed explanation

[3]As we have seen in pictures (2.6) and (2.7), each isotope in the plots has a very well defined curve centred in a radio frequency which is characteristic of this nucleus. However, in the case of these two nuclei, there is an overlap. It makes it difficult to avoid the presence of some ^{102}Mo isotopes in the isotope selection process. In this case, this is due to the mass difference between ^{102}Mo and ^{102}Tc.

about contamination, calibration, etc. will be given in the next chapter.

isotope	$T_{1/2}$ [s]	t_{cycle} [s]	counting rate (counts/s)	comments
^{105}Mo	35.6	60	2870	$^{105}Mo \longrightarrow ^{105}Tc$. Measured because it has priority 1 in the high priority list and also as possible contamination of the ^{105}Tc decay.
^{105}Tc	456	720	2434	$^{105}Tc \longrightarrow ^{105}Ru$. It has priority 1 in the high priority list.
^{102}Mo	678	1080	1940	$^{102}Mo \longrightarrow ^{102}Tc$. Measured as possible contamination of its daughter nucleus and also to produce ^{102}Tc through its decay.
^{102}Tc	5.28	10	1754	$^{102}Tc \longrightarrow ^{102}Ru$. It has priority 1 in the high priority list. Very low production at the IGISOL facility.
^{101}Nb	7.1	12	2110	$^{101}Nb \longrightarrow ^{101}Mo$. It has priority 1 in the high priority list.
^{101}Mo	876.6	12	1785	$^{101}Mo \longrightarrow ^{101}Tc$. Measured as possible contamination of the ^{101}Nb decay.
^{104}Tc	1098	1800	4234	$^{104}Tc \longrightarrow ^{104}Ru$. It has priority 1 in the high priority list.
^{107}Tc	21.2	30	1857	$^{107}Tc \longrightarrow ^{107}Ru$. It has priority 2 in the high priority list.
^{107}Ru	225	30	1800	$^{107}Ru \longrightarrow ^{107}Rh$. Measured as possible contamination of the ^{107}Tc decay.
^{106}Tc	35.6	60	2125	$^{106}Tc \longrightarrow ^{106}Ru$. It has priority 1 in the high priority list.

Table 2.1: Counting rate of all the isotopes measured and collection cycles used in the measurements. Comments are also given for each nuclei. The background had a counting rate of 1750 counts/s and was very stable during the measurements.

2.3.1 Problems during the experiment

Apart from the usual problems that are inherent to the preparation and the starting up of an experiment, the most relevant problem we faced was related to the tape control system and its precision to place the source in the exact point inside the TAGS detector and just in front of the Si detector. Because of this uncertainty, the data from the Si detector are not 100% reliable although the TAGS data are not affected since this kind of detector has a geometry close to 4π around the source. The problem lies in the fact that not all the β-particles produced in the disintegrations could be registered, so instead of using the coincidence data, we will use the singles TAGS data. This problem does not mean that the coincidence data cannot be useful. In the next chapter it will be explained how to use this information.

3 Data analysis

This chapter concerns the technical details of the analysis performed. The analysis process will be explained and some other important features related to the analysis will be introduced. The different calibration procedures can be found in the second section about the data treatment in this chapter. It also includes a brief description of some possible external contaminations. These contaminations can become a serious problem when one tries to analyze a nucleus. The subtraction of these data from the original measured spectrum is the solution to this problem.

3.1 Data treatment I: sorting the data

Sorting the data is the first stage during the analysis process. The procedure is 1) we read the raw data generated during the measurements; 2) we convert it into an ASCII file; 3) we store the ASCII data in a TTree; and 4) we save it in a ROOT file (for more information about the Object-Oriented Data Analysis framework see reference [51]). Once we have done this, we have to pass through all the data event-by-event, making projections of all the parameters of interest, and finally getting the desired spectra.

3.2 Data treatment II: calibrations

Once we have obtained the spectra, the next step is to calibrate them in order to have a correspondence between channels and energies. The simulations, needed for the construction of the response matrix (see section 3.4), must be also calibrated.

It is required that experiment and simulation have the same calibration in order to use them with the analysis programs. So, to compare simulations with experiment we needed:

1. to recalibrate one of the spectra to the other. In our case, we recalibrate experiment to simulation.

2. to widen the simulated response function[1]. We do that with the instrumental width, defined as the difference of the square of the widths:

$$\sigma^2 = \sigma_{exp}^2 - \sigma_{sim}^2 \tag{3.1}$$

The calibrations of the experimental spectra were performed using measured sources of ^{24}Na and ^{137}Cs. These sources have the property that all of them are well-known, with simple level schemes.

In the next two tables we summarize the energies used for the calibrations. Table (3.1) contains the γ-ray energies for the experiment calibration. It includes the γ-ray energy peak from the disintegration of ^{137}Cs to ^{137}Ba, the two γ-ray energy peaks of the decay of ^{24}Na to ^{24}Mg and the corresponding γ-ray sum peak. We must cover an energy range as wide as possible in order to have a proper calibration. The lowest energy available with the calibration sources is that corresponding to the disintegration of Caesium, 661.66 keV, but there are isotopes under study that have well-known γ-rays with energies lower than the Barium γ-ray energy. This is the reason why we have added the γ-ray energy peaks of ^{106}Ru and ^{104}Ru. These two nuclei have γ-rays with energies of 270.07 keV and 358.02 keV, respectively.

The fit of the peaks for the experiment was done with a combination of three functions, a Gaussian with an additive tail, a step function and a linear background function. The additive tail has the form[52]:

$$P_1 e^{-\frac{(x-X+P_2\sigma)^2}{2\sigma^2}} \tag{3.2}$$

where X and σ stand for the centroid (in channels) and the Gaussian width parameter of the main Gaussian. P_1 and P_2 are constants.

[1] A scintillation detector converts the energy into light. Part of the light is collected by a photomultiplier tube and transformed into an electrical signal. The signal is amplified by the tube and processed by the electronic chain. Usually the effect of all these statistical processes is condensed in an empirical instrumental resolution distribution. The simulations do not include this effect so widening the simulated data is necessary to obtain comparable spectra.

Nucleus	energy (keV)	comments
^{106}Ru	270.07	$2^+ \rightarrow 0^+$
^{104}Ru	358.02	$2^+ \rightarrow 0^+$
^{137}Ba	661.66	$11/2^- \rightarrow 3/2^+$
^{24}Mg	1368.633	$2^+ \rightarrow 0^+$
	2754.028	$4^+ \rightarrow 2^+$
	4152.661	sum peak

Table 3.1: Calibration energies for the experiment.

In the simulations we have more freedom concerning the energies used for the calibration: we can simulate γ-rays of any energy. Due to this fact we have also included some extra simulated energies (table (3.2)). These energies are 150, 997 and 1112 keV.

Nucleus	energy (keV)	comments
	150.00	
^{106}Ru	270.07	$2^+ \rightarrow 0^+$
^{104}Ru	358.02	$2^+ \rightarrow 0^+$
^{137}Ba	661.66	$11/2^- \rightarrow 3/2^+$
	997	
	1112	
^{24}Mg	1368.633	$2^+ \rightarrow 0^+$
	2754.028	$4^+ \rightarrow 2^+$
	2870	$2^+ \rightarrow 2^+$
	3866	$3^+ \rightarrow 2^+$
	4238	$2^+ \rightarrow 0^+$

Table 3.2: Calibration energies for the simulations.

Concerning the fitting of the simulated γ-ray energy peaks, it was a trickier situation. The simulations were performed over an energy range of 8192 keV in 4096 channels (2keV/channel). It is difficult to fit them correctly with the same functions as those used for fitting the experimental peaks. So instead of using them, centroid and sigma were obtained with the ROOT functions *GetMean()* and *GetRMS()*, respectively.

Energy calibration

For the energy calibration we have represented the energy versus channel. The points at low energies were fitted to a quadratic function, and for those at high energies a linear function was used. Both fits must coincide in one point, denoted by X_0, so the next condition must be satisfied:

$$a + bX_0 + cX_0^2 = n + mX_0 \tag{3.3}$$

a, b, c, X_0 and m are considered free parameters and n depends on them. It turned out that this X_0 has the same value in both calibrations, experiment and simulation:

$$X_0 = 400 \ channels$$

The experimental calibrations are:

1. For low energies

$$E = 6.464 + 1.610 \cdot chan + 1.182 \cdot 10^{-4} \cdot chan^2 \tag{3.4}$$

2. For high energies

$$E = -21.550 + 1.728 \cdot chan \tag{3.5}$$

And for the simulation:

1. For low energies:

$$E = -6.345 + 36.904 \cdot chan + 4.736 \cdot 10^{-2} \cdot chan^2 \tag{3.6}$$

2. For high energies:

$$E = -30.731 + 39.071 \cdot chan \tag{3.7}$$

Width calibration

In this case, the points were fitted using a quadratic function of the type

$$\sigma^2 = a + bE + cE^2$$

where we have forced a to be zero. In such way we have obtained the width calibrations:

- For the experiment

$$\sigma^2 = 1.06163 \cdot E + 9.25599 \cdot 10^{-5} \cdot E^2 \tag{3.8}$$

- And for the simulation

$$\sigma^2 = 0.23584 \cdot E + 3.17613 \cdot 10^{-5} \cdot E^2 \tag{3.9}$$

Instrumental width

The instrumental width (defined by equation (3.1)) is fitted with a quadratic function with the parameter a fixed to zero as for the width calibration. The result of this fit is

$$\sigma^2 = 0.87542 \cdot E + 3.91923 \cdot 10^{-5} \cdot E^2 \tag{3.10}$$

3.3 Data treatment III: subtraction of possible contaminations

A common problem of any detector is that the measured data could be suffering from some external contaminations. Our detector is not free from this problem. Care must be taken with all these contaminations because they introduce undesired counts in our spectra that must be controlled and eliminated from the measured spectra. The most common distortions and contaminations that one could find in the data are pulse pileup and room background, respectively. However, an additional contamination could arise in the measured data related to the decay of the daughter and/or the presence of the parent decay of the nuclei under study.

3.3.1 Electronic pileup

The electronic pileup must be removed from the spectra, otherwise, the unphysical contribution of the pulse pileup to the deduced β-strength could appear[53]. In order to solve this problem, we calculate the pileup following the procedure described in reference [53], and subtract it from the measured spectrum.

3.3.2 Room background

The ideal way to perform an experiment is in an isolated place free from external background contamination. However, this is not easy in practice, for example, the walls

of the experimental hall contains Potassium and the background measurements present a strong peak at the energy of 1460.859 keV due to the decay of this long-lived element with $T_{1/2} = 1.25 \times 10^9$ y. Other background contributions are due to the protons coming from the JYFL K130 cyclotron beam or scattered protons coming from other places that produce neutrons which in turn produce γ-rays (through elasctic, inelastic and n-capture processes). This contribution can be reduced with Lead shielding placed around the total γ-ray absorption spectrometer as shown in the picture (3.1). Using this shielding, the number of counts per second obtained for the background was around 1750. Concerning the cosmic background, it could be further reduced by an active plastics shielding. This kind of shielding was not available in the experiment.

Figure 3.1: TAGS lead shielding.

The room background was measured during one hour every two hours of data measurements. In this way, the background was continuously checked and if any problem arose, we were able to solve it. This contamination remained stable during all the experiment. However, the beam energy change produced during the experiment (see 2.3.1), involved a small change in the background spectra. The picture (3.2) shows the background before and after the change of the beam energy. The files plotted in this picture correspond to the sum of all the background files obtained when the proton beam had an energy of 50 MeV and after the change of energy to 30 MeV. The files do not contain the same number of counts so they have been scaled to one of them. In such way they can be compared directly. The difference between both spectra is minimal except in the region between channels 2000 and 4000, where the background due to neutrons is larger

for the high energy beam.

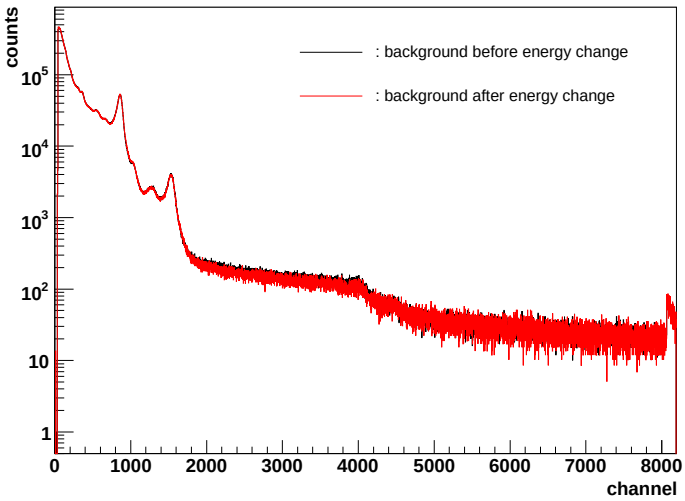

Figure 3.2: Background measured during the experiment before and after of the proton energy beam change.

In this background plot, two strong peaks appear. The first one is placed round channel 880 and comes from the decay of ^{40}K (1460.859 keV). The second peak is close to channel 1550. It corresponds to the decay of ^{208}Tl to ^{208}Pb with an energy of 2614.529 keV.

3.3.3 Other contaminations: additional parent or daughter activity

The extremely good separation of the isobars obtained with JYLTRAP solves only part of the contamination problem, since during the measurements the daughter decay can also contaminate our spectra. In order to deal with this kind of contamination, the daughter of some nuclei were measured. The contribution of the daughter activity can be reduced in general by proper choice of collecting/measuring cycles of the decay of interest but in some cases it can not be avoided completely and then the contribution of the daughter activity has to be evaluated and subtracted. The factors need for the subtraction of the daughter activity were obtained by solving the Bateman equations (see table (3.3)).

Decay	$T_{1/2}$ [s] parent	$T_{1/2}$ [s] daughter	t_{cycle} [s]	daughter contamination [%]
$^{101}Nb \longrightarrow ^{101}Mo$	7.1	876.6	12	1.88
$^{105}Mo \longrightarrow ^{105}Tc$	35.6	456	60	13.76
$^{105}Tc \longrightarrow ^{105}Ru$	456	15984	720	4.77
$^{106}Tc \longrightarrow ^{106}Ru$	35.6	32278176	60	2.16×10^{-4}
$^{107}Tc \longrightarrow ^{107}Ru$	21.2	225	30	12.97

Table 3.3: Estimation of daughter contamination obtained by applying the Bateman equations for some isotopes studied. ^{102}Tc and ^{104}Tc decay to stable isotopes so they are not included in this table.

These corrections were applied in the cases were the daughter activity contamination was above 5% of the measured spectrum of interest, i.e., for the ^{105}Mo and ^{107}Tc decays.

In the case of ^{102}Tc, produced through its parent nucleus, problems arose with the spectra obtained. This is because it is impossible to avoid the ^{102}Mo decay contamination: the ^{102}Mo has a much longer lifetime (11.3 min) compared with the lifetime of ^{102}Tc (5.28 s). The parent contamination made this nucleus the most difficult case of all of the studied nuclei, and its analysis must be handled in a special way. We have to incorporate the known level scheme of ^{102}Mo to the analysis and subtract it as a contaminant.

3.3.4 Subtractions and determination of the contamination factors

Taking into account all the different contaminants that our TAGS decay data could have, the general form of the spectrum free of contaminant, namely A, would be

$$A_i = M_i - \lambda_B B_i - \lambda_P P_i\Big(- \lambda_C C_i\Big), \quad i = 1, ..., n \tag{3.11}$$

where we have denoted as M the measured spectrum, B is the spectrum corresponding to the background, normalized by a factor λ_B, P is the distortion introduced by the electronic pulse pileup, weighted a factor λ_P and C is the daughter activity contamination normalized by a factor λ_C. The daughter activity contamination (term in brackets) is only used when the daughter activity contribution exceeds a 5% of the measured spectrum. The errors in the spectrum A are given by the covariance matrix $\sigma_{A_i A_j}$

$$\sigma_{A_i A_j} = \sigma_{M_i M_j} + \lambda_B^2 \sigma_{B_i B_j} + B_i B_j \sigma^2_{\lambda_B} + P_i P_j \sigma^2_{\lambda_P}\Big(+ \lambda_C^2 \sigma_{C_i C_j}\Big) \tag{3.12}$$

We have assumed that the calculated pileup P is free of uncertainties and we have adopted the criterion that the contents of the TAGS spectra follow the Poisson distribution.

The normalization factors have been calculated as follows:

- Background normalization factor: in the region at the end of the spectrum, denoted as R_1 in figure (3.3), where only the background contributes, the measured spectrum M could be written as

  $$M_i = \lambda_B B_i$$

  so the value of λ_B would be the integral value of the measured spectrum in this region R_1, ΣM_{R_1}, divided by the integral value of the background spectrum in the same region, ΣB_{R_1}:

  $$\lambda_B = \frac{\Sigma M_{R_1}}{\Sigma B_{R_1}}$$

- Pileup normalization factor: just above the Q-value, the measured spectrum is basically background and pileup, region R_2 in the figure (3.3), if there are no other contaminants. It means that

  $$M_i = \lambda_B B_i + \lambda_P P_i$$

  Assuming that the value of λ_B has been previously determined, we can define the value of λ_P as

  $$\lambda_P = \frac{\Sigma M_{R_2} - \lambda_B \Sigma B_{R_2}}{\Sigma P_{R_2}}$$

  where ΣM_{R_2}, ΣB_{R_2} and ΣP_{R_2} are the integral values of M, B and P, respectively, in the region R_2.

R_1 and R_2, are different for the different nuclei. The ones shown in figure (3.3) are the corresponding regions used for the ^{104}Tc case.

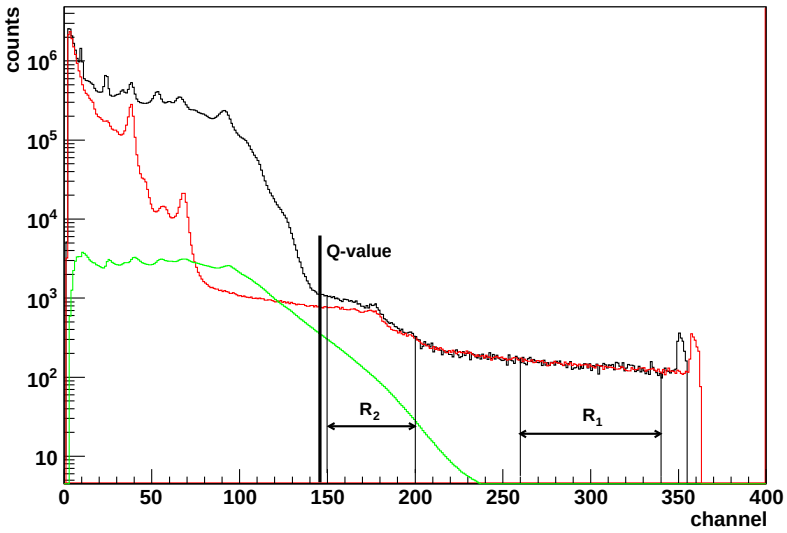

Figure 3.3: Recalibrated spectrum for ^{104}Tc decay. The different regions, where the normalization factors have been calculated for this nucleus, are labeled. The background normalization factor is calculated from the integral values of the measured spectrum in region R_1. This value is used for the calculation of the pileup normalization factor from the integral values of the region R_2 with the formula given above.

The errors (equations (3.13) and (3.14)) associated with the normalization factors have been calculated using the error propagation formula:

$$\sigma^2_{\lambda_B} = \frac{\lambda_B}{\Sigma B_{R_1}} \cdot (1 + \lambda_B) \tag{3.13}$$

$$\sigma^2_{\lambda_P} = \frac{1}{\Sigma P^2_{R_2}} \cdot (\Sigma M_{R_2} + \Sigma B_{R_2} \cdot \lambda^2_B + \Sigma B^2_{R_2} \cdot \sigma^2_{\lambda_B}) \tag{3.14}$$

The beta-TAGS coincidence spectrum could help us to decide if the normalization factors are well defined. The spectra of ^{104}Tc, background, pileup and coincidence data spectra are compared in figure (3.4). The agreement above channel 147 (the corresponding ^{104}Tc Q-value in channels, obtained with the equation (3.7)) between the calculated pileup and the coincidence spectrum indicates that the pileup normalization factor is correct. On the other hand, the blue line, which is the result of subtracting the contaminants from the ^{104}Tc measured spectrum, runs almost in full agreement with the coincidence spectrum except for the high energy part where the energy threshold of the

Si detector plays a more important role in the Si-TAGS coincidence spectra (low energy betas). The normalization factors for each nucleus obtained in this way will be given for each nucleus in the next chapter.

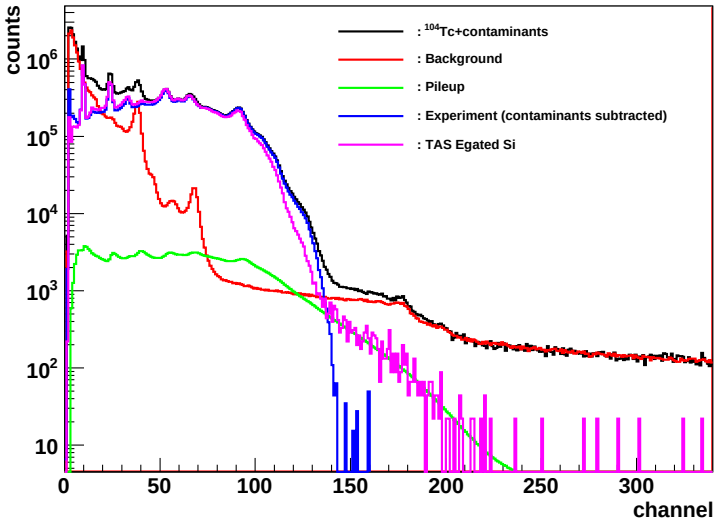

Figure 3.4: Measured spectrum for ^{104}Tc with the contaminants normalized with the proper factors and the beta-gated coincidence spectrum. The good agreement between experiment (contaminations subtracted) and beta-gated coincidence spectrum reflects the quality of the method used.

- Daughter normalization factor: as mentioned earlier, the daughter contamination factor can be determined solving the Bateman equations with the measuring cycle information (implantation/transport/measuring time). The Bateman equations give us the percent of the daughter contamination, namely r. This method is based on the assumption that the TAGS has an approximately 100% efficiency for the detection of gamma cascades. Then, the integral of the measured parent nucleus decay spectrum, background and pileup free,

  $$\sum_i \left(M_i^p - \lambda_B^p B_i^p - \lambda_P^p P_i^p \right),$$

  will be a 100% of parent contribution plus a r% of daughter contribution. If we also calculate the integral of the measured daughter nucleus decay spectrum,

background and pileup subtracted with the corresponding factors for the daughter nucleus,

$$\sum_i \left(M_i^d - \lambda_B^d B_i^d - \lambda_P^d P_i^d \right),$$

we can easily determine the daughter contamination factor as:

$$\lambda_C = \frac{\sum_i \left(M_i^p - \lambda_B^p B_i^p - \lambda_P^p P_i^p \right) \cdot r}{\left(100 + r \right) \cdot \sum_i \left(M_i^d - \lambda_B^d B_i^d - \lambda_P^d P_i^d \right)}$$

where the superscripts p and d have been added to distinguish between parent and daughter. In case there are $gs \longrightarrow gs$ transitions, additional corrections have to be considered for this factor, since the TAGS response is different for these transitions.

^{102}Tc case

To analyse this nucleus we need, first of all, the response function for the $^{102}Mo \rightarrow ^{102}Tc$ decay. We construct it from the known level scheme of this nucleus, fixing the feeding to the ^{102}Tc ground state to 94.1%[2]. Since the Q_β-value of this decay is only 1.01 MeV, we assume that the β-strength to missing levels is negligible. Once it has been calculated, we make the following steps:

1. We obtain the pileup and background normalization factors in the way explained earlier.

2. The ^{102}Mo has a Q-value of 1014(23) keV, and the last known level has an energy of 359.9 keV. The equivalence between channels and energy for low energies (equation (3.6)) tell us which channel corresponds to this energy, which is channel 10. Taking this into account and the fact that the first excited state of ^{102}Tc has an energy of 475.21 keV, we assumed that from channel 12 (443.33 keV) forward, there is no influence of ^{102}Mo in the ^{102}Tc spectrum. So we performed a first analysis of the nucleus from channel 12 until the end of the spectrum. The analysis process will be explained in detail in the next section.

3. The integral value of the feeding file obtained from the analysis gives us the normalization factor needed for the Molybdenum contamination, λ_{Mo}. This is called a self consistency requirement: due to the difference between the lifetimes of the two nuclei, ^{102}Tc and ^{102}Mo, one can expect that every decay of ^{102}Mo will produce a decay of ^{102}Tc.

[2]We tried with other values from 90 to 98%, in steps of 1%, but at the end we decided to use 94.1%, which is the feeding given in the literature. See more details in the next chapter.

Once we have this factor, the ^{102}Mo spectrum is scaled by λ_{Mo} and summed up to the background spectrum which was previously scaled by the factor λ_B

$$BMo_i = \lambda_B B_i + \lambda_{Mo} Mo_i$$

Then, the corresponding spectrum free of contaminants A for the ^{102}Tc would be

$$A_i = M_i - BMo_i - \lambda_P P_i, \quad i = 1, ..., n \tag{3.15}$$

where no normalization factor is needed for BMo_i because it has been previously normalized. And the errors associated with this spectrum are given by

$$\sigma_{A_i A_j} = \sigma_{M_i M_j} + (\lambda_B^2 \sigma_{B_i B_j} + B_i B_j \sigma_{\lambda_B}^2 + Mo_i Mo_j \lambda_{Mo}) + P_i P_j \sigma_{\lambda_P}^2 \tag{3.16}$$

For equation (3.16) we have assumed that the calculated ^{102}Mo spectrum is free of uncertainties and the error in λ_{Mo} is the square of the ^{102}Mo spectrum content in each bin (assuming a Poisson distribution for the ^{102}Mo spectrum).

3.4 Construction of the response matrix R

This is the next step in the analysis process. Although a very detailed description of the process of construction of the response matrix is given in reference [28], a brief descripton is given here.

The level response, j column of the response matrix R_{ij}, depends on all quanta emitted in the decay. If the response to a given quantum does not depend on the response to the other quanta, then the response matrix can be constructed from the individual response distributions. In the sense we are using it, the response $\mathbf{q} = \{q_i\}$ for a single quantum of energy E represents the probability that the spectrometer will register a count in a given channel i (in our case related to the light collected by the photomultiplier tubes). Generally there will be a probability of not registering any count. For this probability of non-interaction a fictitious channel zero is introduced so the response will be normalized to unity.

The response to two coincident quanta can then be obtained by convolution of the respective responses $\mathbf{p}$ and $\mathbf{q}$:

$$[p \otimes q]_i = \sum_{k=0}^{i} p_{i-k} q_k$$

In this way, the total response can be constructed by successive convolution of the single quantum responses. Then, the level j response, R_j, is constructed by convolution of the response to the electromagnetic de-excitation of level j, r_j, with the corresponding decay emission response to this level, $b_j^{\pm}$. The response to the electromagnetic de-excitation can be obtained in a recursive way starting from the level of lowest excitation energy. For a pure γ-ray de-excitation it takes the form:

$$\mathbf{r_j} = \sum_{k=0}^{j-1} b_{jk} \mathbf{g_{jk}} \otimes \mathbf{r_k} \tag{3.17}$$

where b_{jk} is the branching ratio for transition $j \longrightarrow k$ and g_{jk} stands for the response to the γ-ray transition from level j to level k. By convention, we introduce the ground state response r_0 as

$$r_{i0} = \begin{cases} 1 & \text{if i=0} \\ 0 & \text{if } i \neq 0 \end{cases}$$

The response to the γ-ray transition from level j to level k can be replaced by

$$\mathbf{g_{jk}} \longrightarrow \left(\frac{1}{1+\alpha_{jk}^{tot}} \mathbf{g_{jk}} + \frac{\alpha_{jk}^{K}}{1+\alpha_{jk}^{tot}} e_{jk}^{K} \otimes \mathbf{x} + \ldots \right) \tag{3.18}$$

where α_{jk}^{tot} and α_{jk}^{K} are the conversion electron coefficients for transition $j \longrightarrow k$, e_{jk}^{K} is the response to the K conversion electron transition $j \longrightarrow k$ and $\mathbf{x}$ is the response to X-ray emission. In this way we have taken into account the conversion electron process. In general, it is only necessary to consider the response $\mathbf{x}$ to the K X-ray emitted after the conversion electron process. This is so because X-rays filling higher atomic shells or Auger electrons would have too low an energy to be able to reach the sensitive part of the detector after passing the dead material surrounding the source.

Depending on the decay process we will have:

$$R_j^{\beta^-} = \mathbf{b}^- \otimes \mathbf{r_j}, \tag{3.19}$$

$$R_j^{\beta^+} = \mathbf{b}^+ \otimes \mathbf{r_j}, \tag{3.20}$$

$$and\ R_j^{EC} = \mathbf{x} \otimes \mathbf{r_j} \tag{3.21}$$

For β^-- and β^+-decay the response $\mathbf{b}$ corresponds to the continuum distribution of electron or positron energies, respectively, extending up to $Q_\beta - E_j$ if E_j is the excitation energy of level j.

If we assume that we know the de-excitation branching ratios b_{jk} and the conversion electron coefficients α_{jk}, the problem of constructing the TAGS response can be reduced to the problem of obtaining all the individual quanta responses g_{jk}, e_{jk} and $b_j^{\pm}$ involved in the decay. The only suitable way to accomplish this task is by means of Monte Carlo simulations.

Special care must be taken regarding the interactions of the particles with the matter as well as the reproduction of the detector geometry and the characteristics of the materials used. An accurate description of the geometry of the detector has been obtained with Geant4 and the simulations were performed with the same version of this Monte Carlo code, geant4.9.0.p01. The known light yield non-proportionality of the NaI(Tl) detectors[28] was also taken into account for the simulation of the responses.

For the construction of the response matrix, the following partial responses were generated: response functions to γ-rays with the known precise energies for each nucleus as well as to β^- particles with the corresponding end-point energies for each nucleus. On the other hand, two sets of γ and β^- response functions from 40 keV to about 7 MeV in steps of 40 keV were simulated. 40 keV is the energy bin width used in this work.

Some other considerations must be taken into account here that affect the construction of the response matrix:

1. For nuclei far from stability the number of levels accessible in the decay inside the energetically allowed window can easily become of the order of $10^4 - 10^6$. The predicted number of levels for the isotopes under study are summarized in table (3.4):

Isotope	predicted number of levels
^{101}Nb	4537
^{105}Mo	372
^{102}Tc	2030
^{104}Tc	1769
^{105}Tc	82058
^{106}Tc	68358
^{107}Tc	44572

Table 3.4: Predicted number of levels for the isotopes under study using the parametrizations available in RIPL-2[54].

For densely spaced levels, rather than the decay probability to each level, it would be more appropriate to determine the average probability over a certain energy

interval or bin. In such a way, $\mathbf{d} = \mathbf{R} \cdot \mathbf{f}$ can be reinterpreted assuming that j represents a certain bin of mean energy $(j - \frac{1}{2})\Delta E$, f_j the average feeding to levels within that interval and $\mathbf{R_j}$ the average response. However, the average response $\mathbf{R_j}$ is not calculable using an expression similar to equation (3.17) because the branching ratio matrix $\mathbf{b}$ cannot be grouped into bins. The branching, out of the levels within a given bin, depends on how these levels are reached. Thus, the construction of the average response should be based on individual cascades increasing to unacceptable values the number of convolutions necessary to build the response matrix. This introduces a small systematic error, see [28].

2. The branching ratios are only known for a few levels lying at relatively low excitation energy, the known part of the level scheme. For the unknown part of the level scheme, the branching ratios are handled as external parameters introduced by hand. In this way, we reduce the problem to the determination of the feeding distribution instead of determining feeding and unknown branching ratios. The good reproduction of the measured spectrum will be an indication that our guess about the branching ratios is correct.

3.5 Construction of the decay scheme

A knowledge of the decay level scheme is a prerequisite for the construction of the response matrix. In general, the experimental knowledge about the level scheme is limited to low excitation energies, where the electromagnetic de-excitation of a nucleus is given by the de-excitation level scheme. For the corresponding part of the level scheme where there is no experimental data, the electromagnetic de-excitation is described by a model called the *statistical model*. This statistical model is based on average quantities such as level densities and strength functions.

The level excitation energies, spins and parities are obtained from a level density functional $\rho(J, \pi, E_x)$ which describes the dependence of the average density of levels of a given spin-parity with excitation energy. This level density is the inverse of the average level distance D. The parametrization we have chosen is the back-shifted Fermi gas model level density formula [55]:

$$\begin{aligned} &\rho(J, \pi, E_x) = \rho(J, \pi)\rho(E_x) \\ &\rho(J, \pi) = \frac{2J+1}{4\sigma^2} e^{-\frac{J(J+1)}{2\sigma^2}} \quad , \quad \rho(E_x) = \frac{1}{12\sqrt{2}} \frac{e^{2\sqrt{a(E_x - \Delta)}}}{\sigma a^{\frac{1}{4}} (E_x - \Delta + t)^{\frac{5}{4}}} \\ &\sigma^2 = 0.0150 A^{\frac{5}{3}} t \, , \quad t = \frac{1 + \sqrt{1 + 4a(E_x - \Delta)}}{2a} \end{aligned} \tag{3.22}$$

The nucleus dependent parameters a and Δ are sensitive to shell effects and are

usually adjusted in order to reproduce measured level densities. It is assumed that both parities are evenly distributed for each spin and energy.

The average radiation width from levels of spin-parity J^π at excitation energy E_x into levels within a certain energy interval $(E, E+\Delta E)$ can be expressed [56] as:

$$\langle \Gamma_\gamma \rangle = \frac{1}{\rho(J,\pi,E_x)} \sum_{XL} \sum_{J_f^{\pi_f}} \int_{E_x-E-\Delta E}^{E_x-E} E_\gamma^{2L+1} f_{XL}(E_\gamma) \rho(J_f, \pi_f, E_x - E_\gamma) dE_\gamma \qquad (3.23)$$

where X represents the character of the transition ($X = E$ for electric, $X = M$ for magnetic), L is the multipolarity, and the range of final spin-parities $J_f^{\pi_f}$ is given by the XL selection rules. Only transitions of $E1$, $M1$ or $E2$ type have been considered. The strength functions f_{XL} have a Lorentzian shape except for $E1$ where a generalized Lorentzian shape is used [56]:

$$f_{E1}(E_\gamma) = 8.68 \times 10^{-8} \sigma_0 \Gamma_0 \left[\frac{E_\gamma \Gamma(E_\gamma)}{(E_\gamma^2 - E_0^2)^2 + E_\gamma^2 \Gamma(E_\gamma)^2} + \frac{2.8\pi^2 T^2 \Gamma_0}{E_0^5} \right]$$
$$\Gamma(E_\gamma) = \Gamma_0 \frac{E_\gamma^2 + 4\pi^2 T^2}{E_0^2} \,, \quad T = \sqrt{\frac{S_n - E_\gamma}{a}} \,, \qquad (3.24)$$

$$f_{M1}(E_\gamma) = 8.68 \times 10^{-8} \frac{\sigma_0 E_\gamma \Gamma_0^2}{(E_\gamma^2 - E_0^2)^2 + E_\gamma^2 \Gamma_0^2} \,, \qquad (3.25)$$

$$and \; f_{E2}(E_\gamma) = 5.22 \times 10^{-8} \frac{\sigma_0 E_\gamma^{-1} \Gamma_0^2}{(E_\gamma^2 - E_0^2)^2 + E_\gamma^2 \Gamma_0^2} \qquad (3.26)$$

Here a is the level density parameter introduced before, S_n (MeV) is the neutron binding energy, and the giant resonance parameters E_0 (MeV), Γ_0 (MeV) and σ_0 (mb) are taken for $E1$ from reference [57], for $M1$ from reference [56] and for $E2$ from reference [58]. The units of the strength function f_{XL} are MeV$^{-(2L+1)}$. The average γ-widths are just proportional to $E_\gamma^{2L+1} f_{XL}(E_\gamma)$.

In this way, several level schemes were constructed for each nucleus, playing with the different available data: the last known level considered for the known part of the level scheme, where the unknown part starts, and the parameters of the strength functions. On the other hand, in particular cases problems may arise with the high resolution information available for the known part of the level scheme. In some cases the experimental data at low excitation energies are not complete and the spins and/or the parities of some levels remain undefined. Then assumptions on this field are needed too, giving as a result additional different level schemes for the construction of the response matrices.

All the assumptions made for the level scheme will introduce systematic uncertainties in the results. The different initial guesses for each nucleus will be commented on the next chapter.

All the needed data used for the construction of the level schemes and the response matrices are summarized in two tables in the appendix A.

3.6 Analysis method

We need to solve the linear problem described by equation (1.12). As has been commented in chapter 1, some methods have been developed by the authors of reference [29] for analyzing the TAGS data. The one that we have used here is the expectation-maximization method which seems the most appropriate to our problem. This method, previously used for the analysis of other TAGS spectra, is an iterative method which converges quickly. The number of iterations was established following the convergence criteria:

- the feedings obtained should not show unrealistic oscillations,
- the Monte Carlo reconstructed spectra (which will be denoted here as d_{rec} must be as close as possible to the experimental ones d_{exp}. It is evaluated with the χ^2:

$$\chi^2 = \sum_i \frac{(d_{rec} - d_{exp})^2}{\sigma^2_{d_{exp}}} \tag{3.27}$$

Considering our earlier experience and the convergence criteria, we have decided that the maximum number of iterations is 200, and this is the upper value that we have used in the different analyses.

The result of applying the analysis programs gives us the normalized β-feeding distribution to unity, $I_i = f_i / \sum_k f_k$[3], and the corresponding errors. The feeding distribution can then be used for the calculation of the average energies as well as for the β-strength distribution.

3.6.1 Average energies calculation

The average energies are described by equations (1.13) and (1.14). Assuming that the energies are free of uncertainties and the error due to the integrated Fermi function

[3]In this case, f_i stands for the β-feeding distribution without normalization.

is so small that it could be neglected, the errors associated with these average energies will be given by the uncertainties in the feeding distribution:

$$\sigma^2_{\overline{E}_\beta} = \sum_i \left(\frac{f_\beta(E_i - Q_\beta)}{f(E_i - Q_\beta)} \right)^2 \sigma^2_{I_i} \tag{3.28}$$

$$\sigma^2_{\overline{E}_\gamma} = \sum_i E_i^2 \sigma^2_{I_i} \tag{3.29}$$

with

$$\sigma^2_{I_i} = \sum_i \frac{\sigma^2_{f_i}}{\left(\sum_k f_k \right)^2} \tag{3.30}$$

The average energies will have, apart from the error due to the feeding, the systematic error due to their dependence on the assumptions made for the construction of the response matrices. Both kinds of error will be evaluated for each nucleus but as we will see, the error due to the dependence on the construction assumptions is larger than the errors on average energies.

3.6.2 β-strength calculation

The β-strength distribution in the daughter nucleus for energy bin i is given by equation (1.5). The Fermi function is calculated by linear interpolation of the tabulated values given in the *log-f tables for beta decay*[59]:

$$f(Q_\beta - E_i) = 10^{m_i(Q_\beta - E_i) + b_i} \tag{3.31}$$

where m_i and b_i are the coefficients of the linear regression at a given energy E_i.

The error in the strength is given by the error propagation formula

$$\sigma^2_{S_\beta(E_i)} = \frac{1}{(f(Q_\beta - E_i)T_{1/2}\Delta E)^2}\sigma^2_{I_\beta} + \left(\frac{I_\beta(E_i)}{f(Q_\beta - E_i)T^2_{1/2}\Delta E} \right)^2 \sigma^2_{T_{1/2}} + \\ + \left(\frac{I_\beta(E_i)}{f(Q_\beta - E_i)^2 T_{1/2}\Delta E} \right)^2 \sigma^2_{f(Q_\beta - E_i)} \tag{3.32}$$

ΔE is the energy bin width (40 keV in this work). The uncertainty in the half-life is taken from the literature, meanwhile the uncertainty in the Fermi function is given by

$$\sigma_{f(Q_\beta - E_i)} = ln(10) m_i f(Q_\beta - E_i) \sigma_{Q_\beta}$$

The experimental value of the integrated β-strength is usually expressed in terms of the total log ft

$$log ft = log_{10} \left(\frac{1}{\sum_i S_\beta(E_i) \Delta E} \right) \tag{3.33}$$

In this case, the uncertainty in this quantity is given by

$$\sigma^2_{log\, ft} = \frac{1}{(ln10\, ft)^2} \sigma^2_{ft} \tag{3.34}$$

since ft can be written as

$$ft = \left(\frac{1}{\sum_i \frac{I_\beta(E_i)}{f(Q_\beta - E_i) T_{1/2}}} \right) \tag{3.35}$$

σ^2_{ft} is

$$\sigma^2_{ft} = \left(\frac{ft}{T_{1/2}} \right)^2 \sigma^2_{T_{1/2}} + \left(-\frac{ft^2}{f(Q_\beta - E_i) T_{1/2}} \right)^2 \sigma^2_{I_\beta(E_i)} + \\ + \left(\frac{I_\beta(E_i) ft^2}{f(Q_\beta - E_i)^2 T_{1/2}} \right)^2 \sigma^2_{f(Q_\beta - E_i)} \tag{3.36}$$

For all the nuclei analysed, the β-strength distribution is also given.

4 Results and discussion

4.1 Results for the nuclei studied

In this section we are going to discuss the results obtained for each nucleus. First of all, a brief description of the nuclei will be given and the assumptions made for each analysis case will be pointed out. The way the normalization factors were obtained was commented on in the previous chapter (see section (3.3)) so only the resulting factors will be mentioned here.

The feeding distribution deduced from the analysis of the decaying nuclei will be compared with the experimental feeding distribution available from the latest compilation of ENSDF[60] for each nuclei. These data are based on high resolution measurements. The result of the comparison will give us an idea about the importance of the Pandemonium effect on those nuclei. A shift to high energies of the TAGS feeding distribution is expected for nuclei that suffer from "Pandemonium". Related to this shift, a change in the average energies is also expected. The average energies obtained with our experimental setup will be compared with those from the JEFF-3.1 database[61].

On the other hand, the strength distribution obtained for each nucleus will be compared with the experimental high resolution strength distribution and with calculation using Gross theory[62].

4.2 ^{102}Tc decay results

4.2.1 The analysis of $^{102}Tc \rightarrow ^{102}Ru$ decay

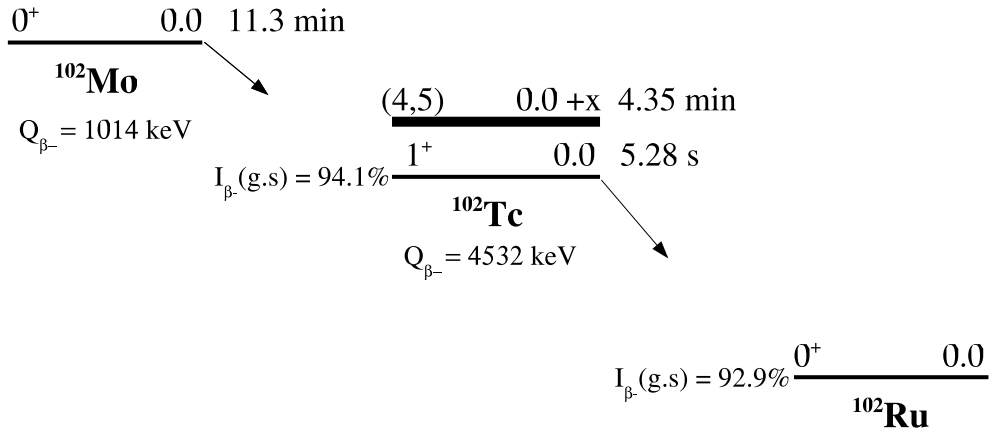

Figure 4.1: ^{102}Mo and ^{102}Tc decays. The ^{102}Tc was produced hrough the decay of ^{102}Mo parent.

In figure (4.1) is shown part of the decay chain of mass 102. Information related to ground state spins and parities, half-lives, Q-values and feeding intensities assigned to the daughter ground states can be found in it. ^{102}Tc has an isomeric state with a half-life of 4.35 minutes and spin (4,5) which also decays to high spin levels in ^{102}Ru. The level scheme of the ^{102}Ru nucleus is quite well known experimentally (spins and parities) up to the excitation energy 1873.2 keV. There is only one level with uncertain spin-parity assignment at excitation energy 1602.9 keV but it is not fed directly in the decay, $(3,4^+)$. We assumed 3^+ for this level in the analysis.

For the construction of the response matrix of the ^{102}Tc decay we have used the precise energies up to 1873.2 keV and from 1960 keV up to the Q-value the statistical model was used in the way described in the previous chapter. However, for the characterization of ^{102}Mo decay only the experimental information available in reference [63] has been used. The ^{102}Mo decay has a small β-decay value and for nuclei with small Q-values it is expected that the experimental data are free of the Pandemonium effect and then it can be considered to be reliable.

Another relevant parameter in the analysis of any isotope is the β intensity to the ground state of its daughter nucleus. In chapter 1 the difficulty of using TAGS spectrom-

eters to detect the $gs \longrightarrow gs$ feeding was mentioned. In this case, most of the feeding goes to the ground states of both ^{102}Tc and ^{102}Ru, 94.1% and 92.9%, respectively. The suitability of these feedings was studied through the evaluation of the χ^2 for different values of both ^{102}Tc and ^{102}Ru ground state feedings. In this case, the χ^2 is given by

$$\chi^2 = \sum \frac{exp - (^{102}Mo + ^{102}Tc)}{^{102}Mo + ^{102}Tc}$$

where *exp* refers to the experimental spectrum and ^{102}Mo and ^{102}Tc are the ^{102}Mo and ^{102}Tc reconstructed decay spectra obtained from the analyses, respectively.

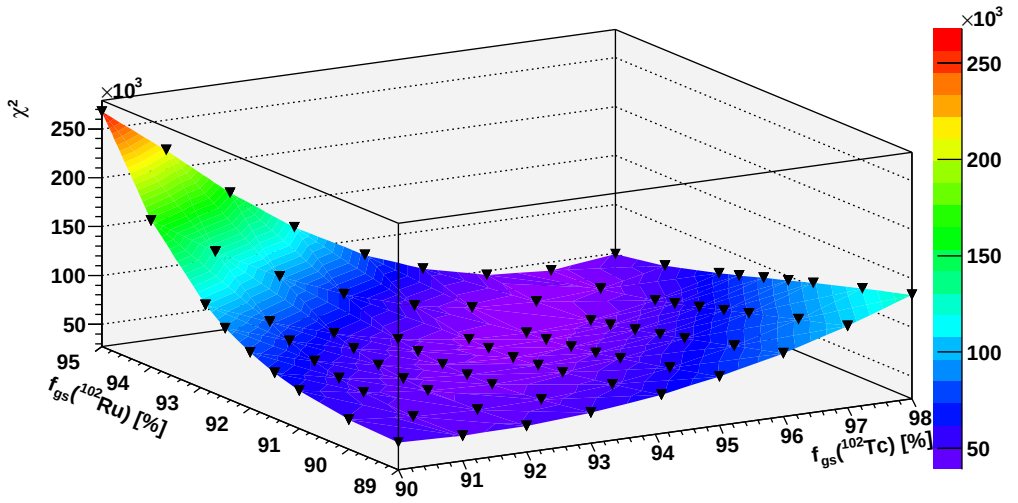

Figure 4.2: Surface of χ^2 values obtained using different ^{102}Tc and ^{102}Ru ground state feedings.

The different decay response functions for the decay of ^{102}Mo were constructed varying the ground state feeding from 90 to 98% in steps of 1% (including the value in the literature, 94.1%). On the other hand, we performed analyses of the ^{102}Tc decay data from channel 12 (443.33 keV, where there is no ^{102}Mo influence) on, fixing the ^{102}Ru ground state feeding to 89, 90, 91, 91.5, 92, 92.5, 92.9, 94 and 95%, respectively. For each analysis (i.e. ^{102}Ru ground state feeding) we obtained one ^{102}Tc reconstructed decay spectrum and one feeding file. Each ^{102}Mo spectrum was scaled by a factor given by the integral value of each feeding file and it was summed to the corresponding ^{102}Tc decay spectrum for the calculation of the χ^2. In such way we constructed a three-dimensional

χ^2-plot, see figure (4.2).

The absolute minimum χ^2 corresponds to the case where there is 96% of feeding to ^{102}Tc ground state and 94% of feeding to ^{102}Ru ground state. The value of the χ^2 obtained using the feedings given in the Nuclear Data sheets is quite close to the minimum, this is the reason why we decided to keep the original values (94.1% and 92.9% respectively, for ^{102}Tc and ^{102}Ru ground state feedings).

Last known level considered	1873.2 keV
Start unknown part	1960 keV
Background normalization factor	1.15 ± 0.01
Pileup normalization factor	$(3.34 \pm 2.93) \cdot 10^5$
^{102}Mo normalization factor	$(2.6676 \pm 0.0005) \cdot 10^7$
Comments	^{102}Tc ground state feeding fixed to 94.1%
	^{102}Ru ground state feeding fixed to 92.9%

Table 4.1: Assumptions made for the analysis of ^{102}Tc decay.

4.2.2 Result I: feeding distribution

The final analysis was performed fixing both ground state feedings within the analysis program and with the assumptions summarised in table (4.1). The result of the analysis is the feeding distribution shown in the lower panel of figure (4.3). This distribution is compared with the one obtained from high resolution measurements in the same plot. It must be noticed that the feeding for the ground state is divided by a factor 20 in both cases in order to enhance the feeding to excited states. For this nucleus, the decay is dominated by the transition between ground states, thus the excited states of high energy are populated with low probability. Although the feeding of the ground state in our analysis was fixed to the value given by high resolution measurements, the feeding distributions slightly differ.

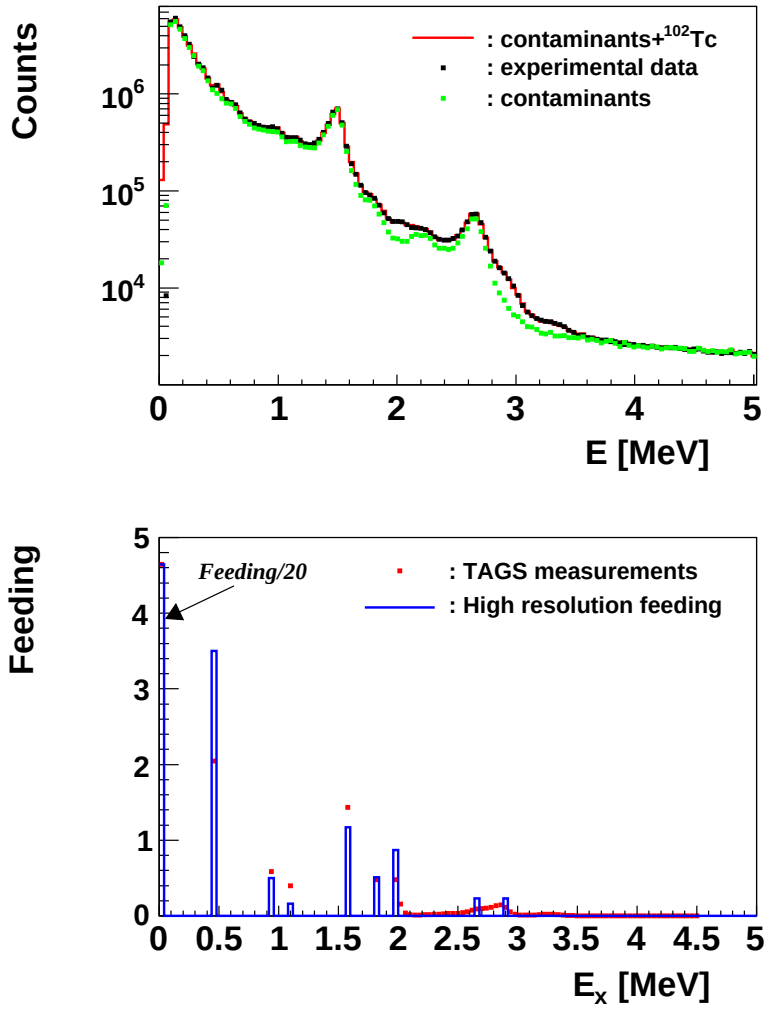

Figure 4.3: Upper panel shows the comparison of reconstructed and experimental data including the contaminations for ^{102}Tc decay. Green dots in the upper panel show the contribution of the contaminants (pileup+background+parent contamination). The β-feeding distribution obtained from the experiment is compared with the one from high resolution measurements in the lower panel.

On the other hand, the upper part of figure (4.3) shows a comparison of the results of the reconstructed spectrum (red continuous line) from our analysis with the measured spectrum (black dots). Both spectra include all the contaminants: background, pileup and ^{102}Mo decay. The contribution of those contaminants is also shown in this plot (green dots). In this way we can do a quick check of how good the Monte Carlo reconstruction of the experimental data is.

The quality of the reconstruction of the decay spectrum can be seen better in figure (4.4). The black dots from the upper panel represent the measured spectrum free of contaminants, with the corresponding errors calculated following equation (3.16). The red line (reconstructed spectrum, contaminants subtracted) fits the experimental data quite well between 1.5 MeV and 3.5 MeV. Up to 1.5 MeV, the experimental points are distributed very closely around the reconstructed spectrum. From 3.5 MeV onwards, the number of counts decreases considerably and the error associated with them become large. In this part of the spectrum, the reconstructed spectrum runs inside the error bars.

The lower panel shows the relative deviations between the spectra:

$$relat.dev. = \frac{reconstructed\,spectrum\ -\ experimental\,spectrum}{experimental\,spectrum}$$

The existing differences between the spectra are better shown in this plot since the number of counts in the upper panel is on a log scale. Larger differences are found at the end of the spectrum, from 3.5 MeV on, as has been indicated in the previous paragraph. It is due to the low statistics that we have close to the Q-value. For low energies, up to approximately 1.5 MeV, the differences are larger than in the central region. They are probably due to a slight mismatch in the energy calibration of the spectra.

The χ^2 deduced for this analysis, obtained using equation (3.27), has the value 47239.3. This relatively high value can be understood from the lower panel of figure (4.4). The relative deviations are not as smooth as one could expect and it may be translated into a large χ^2.

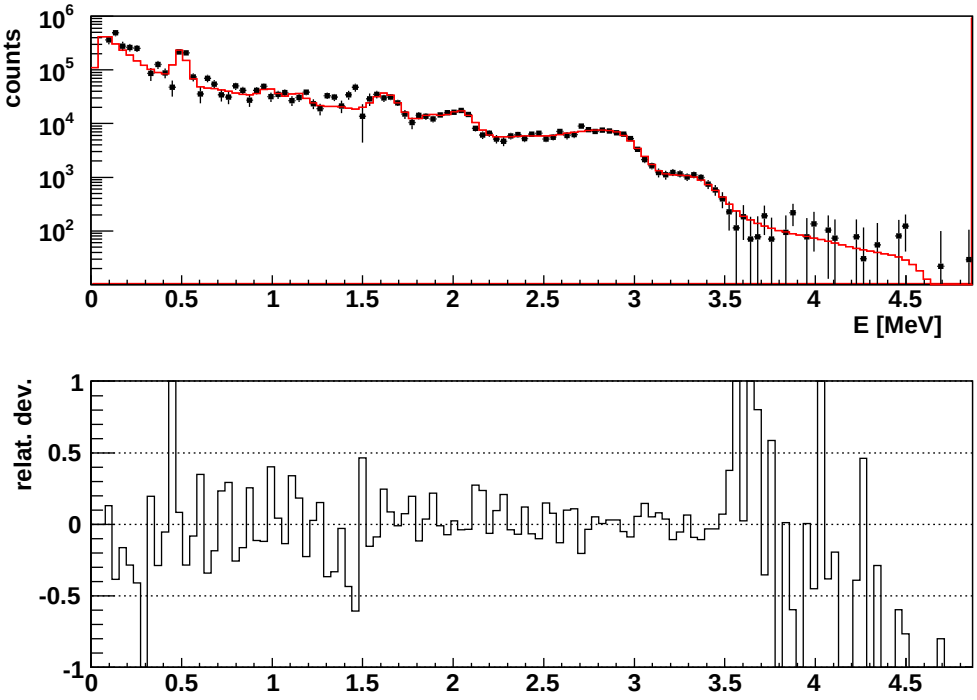

Figure 4.4: In the upper panel we present a comparison between the reconstructed (red continuous line) and experimental (black dots) spectra once the different contaminations have been subtracted from ^{102}Tc decay data. The lower panel corresponds to the relative deviation between the spectra.

4.2.3 Result II: strength distribution

The feeding distribution shown in figure (4.3) was used to calculate the strength distribution for the decay of ^{102}Tc (red dots in figure (4.5)). It is worth mentioning that for convenience the strength values have been multiplied by 10^6 and they are plotted on a log scale.

In figure (4.5), the TAGS strength distribution is compared with the one obtained from high resolution measurements and with the calculated one using Gross Theory. Similarly, in figure (4.6) the accumulated strength is represented. If we sum the strength values in figure (4.5) up to an excitation energy 2900 keV, which is the last known high resolution energy level, we find that the integral value of the TAGS strength is higher

than the integral value of high resolution strength, and the Gross theory prediction is approximately a factor of 5 smaller. This can be seen directly from the accumulated strength values of figure (4.6) at excitation energy 2.9 MeV. In the whole energy interval ($0 \leq E_{ex} < Q_\beta$) available in the decay the Gross theory predicts a strength value which is approximately 4 times less than the value measured with the TAGS.

The explosive behaviour of the TAGS strength distribution when $E_i \rightarrow Q_\beta$ is partially due to an imperfect subtraction of the background close to the end point which is enhanced by the Fermi function. This behaviour will be present in the strength distribution of all the nuclei studied. For that reason the strength to the last channels is not shown and also the feeding to the last channels will not be included in the calculations of global properties such as accumulated strength, B(GT), etc.

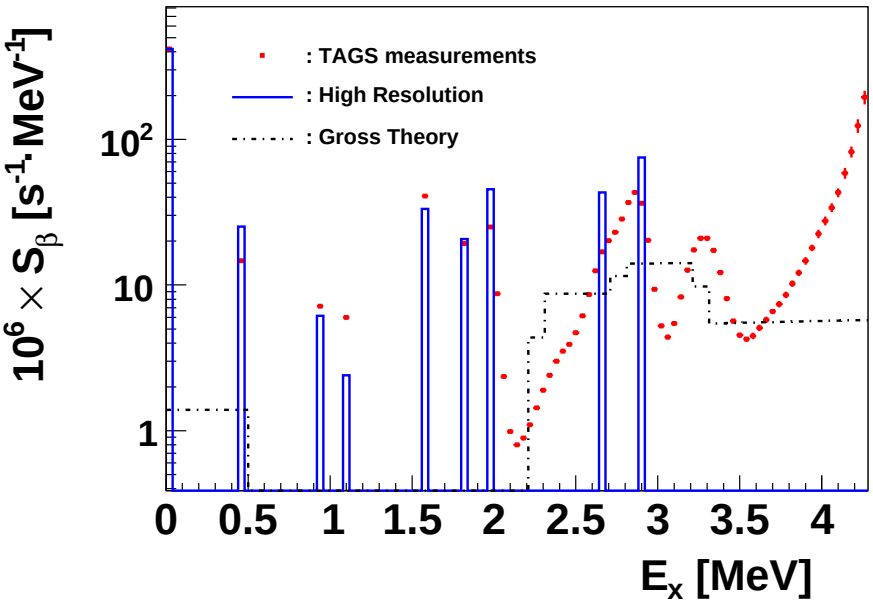

Figure 4.5: Deduced β-strength distribution from the TAGS measurement for the β-decay of ^{102}Tc. A comparison of the TAGS β-strength distribution with high resolution measurements and calculations using Gross theory is also given.

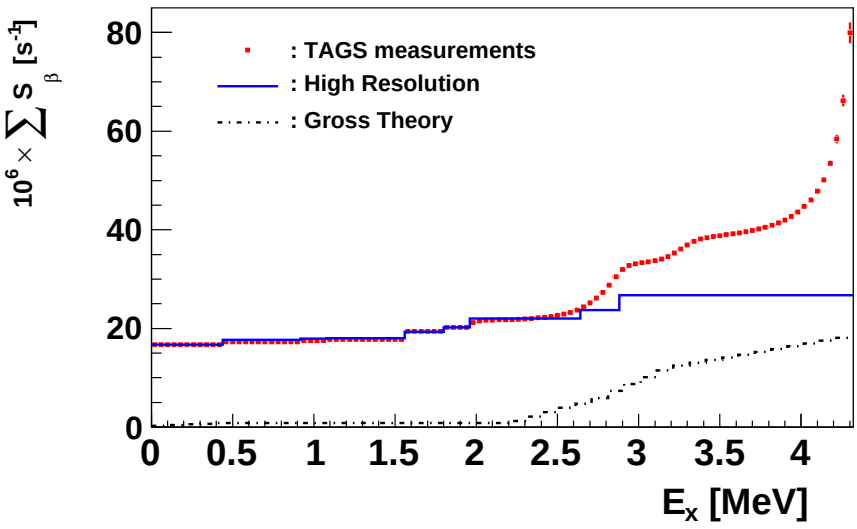

Figure 4.6: Accumulated strength distributions for the decay of ^{102}Tc.

4.2.4 Result III: average energies

The average energies were calculated from the feeding distribution using the equations (1.8) and (1.9). The values obtained were:

$$\overline{E}_\beta = 1935.30 \pm 0.29 \pm 11.00 \text{ keV}$$

$$\overline{E}_\gamma = 105.83 \pm 0.02 \pm 23.00 \text{ keV}$$

The average β- and γ-ray energies are given with two kinds of error. The first error comes from the uncertainties in the feeding distribution, equations (3.28) and (3.29), respectively. The second error is the systematic error due to the dependence of the average energies on the assumptions made for the construction of the response matrix (table (4.1)).

The systematic error has been deduced comparing the average energies obtained for different initial guesses in the feeding to the ground state of ^{102}Tc and ^{102}Ru. This error

is higher than that due to uncertainties in the feeding distribution.

If we compare the values obtained for the average energies with those available at the JEFF-3.1 database

$$\overline{E}_\beta = 1944.97 \pm 15.52 \text{ keV}$$

$$\overline{E}_\gamma = 80.76 \pm 4.59 \text{ keV}$$

we see that the average β-ray energy decreases by 9.67 keV meanwhile the average γ-ray energy increases by 25.07 keV. It can be easily understood if we take into account how a total absorption spectrometer works. With a TAGS we are able to detect the weak γ-cascades coming from feeding at high excitation energies, and thus, the feeding at these energies as shown in the lower panel of figure (4.3). This is not always possible using high resolution setups as explained in chapter 1 and also can be seen in the mentioned plot.

In this case, the Pandemonium effect, i.e. the overestimation of $\overline{E}_\beta$ and underestimation of $\overline{E}_\gamma$, is not very relevant. However, we must think about the special conditions that surrounds this nucleus. The fact that most of the β-feeding goes to the ground state of ^{102}Ru means that only a few percent of the feeding will be distributed among many levels[1]. In such a situation, the effect could not be expected to be significant.

[1] Remember the high number of predicted levels for the decay of ^{102}Tc given in table (3.4)

4.3 ^{104}Tc decay results

4.3.1 Analysis of the decay $^{104}Tc \rightarrow ^{104}Ru$

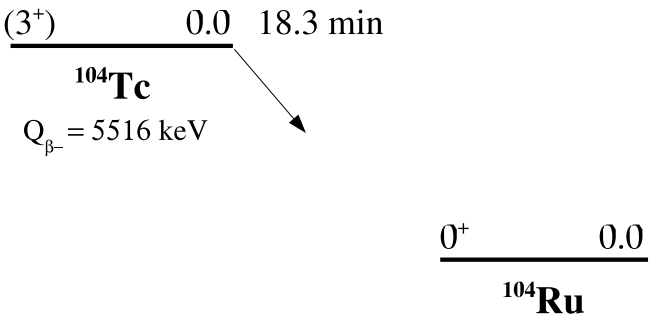

Figure 4.7: ^{104}Tc decay to ^{104}Ru.

Some specific points should be made about the analysis for this nucleus. The first is about the spin-parity of the ground state of ^{104}Tc which is given in brackets. For the analysis 3^+ was assumed. Bearing this in mind as well as the fact that only allowed Gamow-Teller transitions are considered, the ground state of ^{104}Ru will not be directly populated which is in agreement with high resolution measurements.

On the other hand, the ^{104}Tc decay has a large Q_β value, 5516 keV. With such an energy window, the number of possible populated levels can be huge[2]. However, if we check the available information for the decay of this isotope (reference [64]) we find that the known number of levels from high resolution is not so high. In general, the levels from the high resolution ^{104}Ru level scheme at low excitation are well defined. There are two levels with spin and parity in brackets: 1974.8 keV, (6^-,7) which fortunately is not directly populated in the decay and we have assumed 6^-, and 1872 keV, (5^+). For this level 5^+ is used.

In such a context, we decided to perform two kinds of analyses assuming the known level scheme up to the excitation energies 1515.4 keV and 2080.8 keV. With the known level scheme up to 2080.8 keV, the statistical model was used from 2120 keV up to the Q-value. However, with the known level scheme up to 1515.4 keV two types of analysis were performed, one starting the unknown part of the level scheme at 1720 keV and the second one at 1840 keV. We finally decided that the best results were obtained in

[2]See table (3.4) for the predicted number of levels for the isotopes under study.

the case where we have assumed a known level scheme up to 1515.4 keV and used the statistical model from 1720 keV up to the Q-value. This analysis has the advantage that all the inconsistencies are eliminated and it has the lowest χ^2. These values are summarized in table (4.2). The rest of parameters needed for the generation of the average branching ratio matrix can be found in appendix A.

Last known level	1515.4 keV
Start unknown part	1720 keV
Parent spin and parity	3^+
Background normalization factor	0.244 ± 0.003
Pileup normalization factor	$(3.46 \pm 0.20) \cdot 10^5$
Comments	no feeding to ground state

Table 4.2: Assumptions made for the ^{104}Tc analysis.

Regarding this last point, it is worth discussing the deformation parameter used in this case for the calculations of the strength function parameters. From reference [71], this nucleus has a prolate deformation, so we used the value given in this reference, although we decided to try with other values also (see table (4.3)): considering an oblate shape (the same deformation value but with the sign changed) and modifying directly M1, E1 and E2 strength parameters, keeping the rest of the values constant each time. Since compared to the other cases, the decay of ^{104}Tc goes to a well known nucleus (^{104}Ru) from high resolution this study made sense. However, the results of the analyses were worse so we decided to keep the original values of deformation and strength parameters, and present here the results obtained with them.

last known level (keV)	minimum energy for unknown part (keV)	deformation parameter	strength parameter
2080.8	2120	0.253	without modification
1515.4	1840	0.253	without modification
1515.4	1720	0.253	without modification
1515.4	1720	0.253	E1*5
1515.4	1720	0.253	M1*5
1515.4	1720	0.253	E2*5
1515.4	1720	0.253	E1/5
1515.4	1720	0.253	M1/5
1515.4	1720	0.253	E2/5
2080.8	2120	-0.253	without modification
1515.4	1840	-0.253	without modification
1515.4	1720	-0.253	without modification
1515.4	1720	-0.253	E1*5
1515.4	1720	-0.253	M1*5
1515.4	1720	-0.253	E2*5
1515.4	1720	-0.253	E1/5
1515.4	1720	-0.253	M1/5
1515.4	1720	-0.253	E2/5

Table 4.3: Summary of all the analyses done for ^{104}Tc decay. The last column shows the assumptions about the strength parameters. Without modification means that the strength parameters used were those deduced from the deformation parameter. E1, M1 or E2 divided or multiplied by a factor 5 means that the original value of the strength (E1, M1 or E2) was divided or multiplied by this quantity keeping the other original values constant.

Once we have established all the parameters and performed the analysis with them, we reconstructed the experimental spectrum (see figure (4.8)). It reproduces quite well the shape of the spectrum, giving as a result a smooth relative deviation in the lower panel plot.

Apart from the difference due to the low statistics at the end of the spectrum, we also noticed that up to approximately 400 keV, the reconstructed spectrum (red continuous line) runs slightly below the experimental data (black dots). It could be the result of subtracting slight in excess of the contaminants in this part of the spectrum. We have taken a compromise between the fit at low and at high excitation energies, and with the values given for the normalization factors in table (4.2) we obtained the best fit. From the figure, it is deduced that the reconstruction obtained in such way is good.

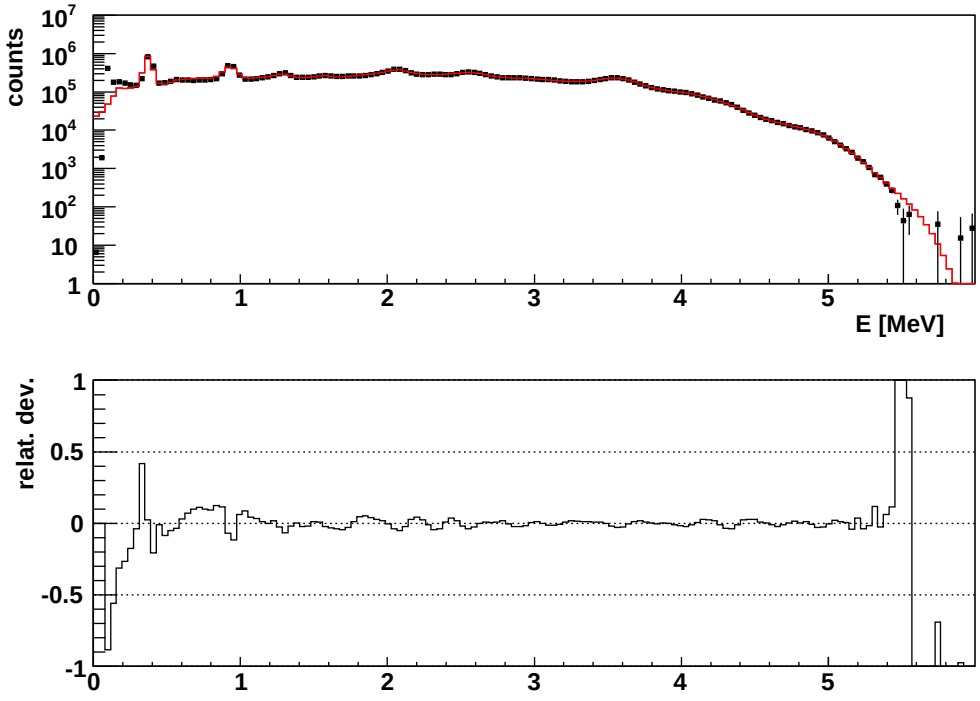

Figure 4.8: In the upper panel the comparison between the reconstructed (red continuous line) and experimental (black dots) spectra once the different contaminations have been subtracted for ^{104}Tc decay is shown. The lower panel corresponds to the relative deviation between the spectra.

4.3.2 Result I: feeding distribution

In the application of the total absorption γ-ray spectroscopy technique, it is very important to use beams of high purity. It is also important to have beams with high production in order to increase the number of total counts in comparison with the room background. In the upper panel of figure (4.9) we see that the production of ^{104}Tc was more than enough to distinguish the ^{104}Tc decay spectrum over the background. In fact, it is easy to distinguish the spectrum shape even without subtracting the contaminants (green dots), which run far from the experimental data (black dots).

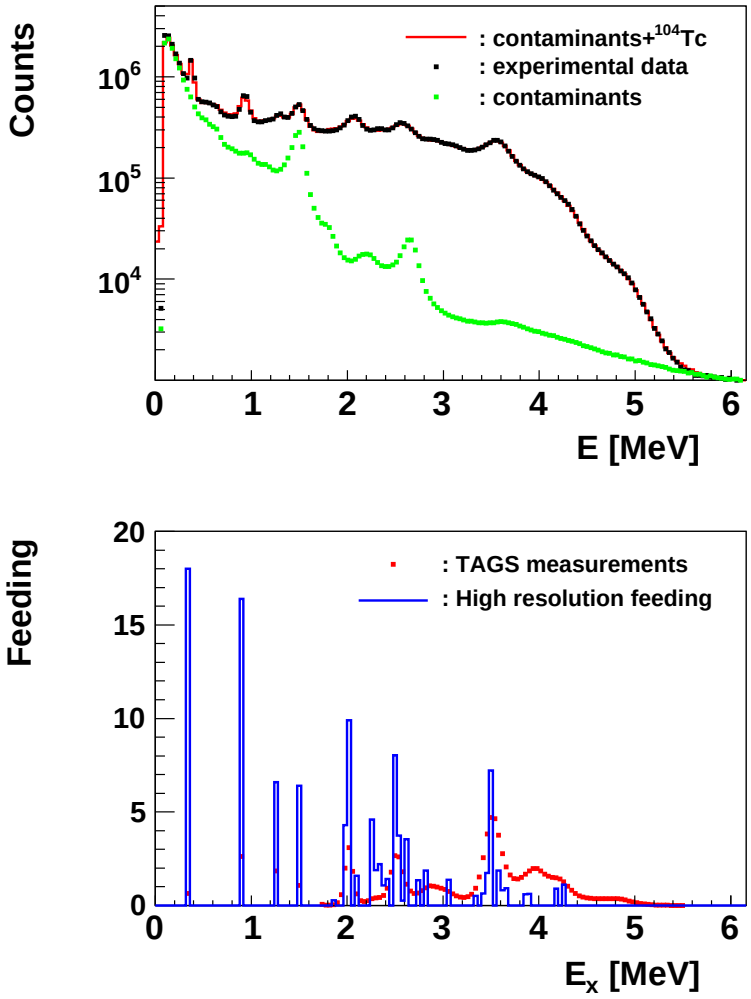

Figure 4.9: The upper panel shows the comparison of the reconstructed spectrum after the analysis with the experimental data (including the contaminants) for ^{104}Tc. The contribution of the contaminants is also presented in the upper panel. In the lower panel the β-feeding distribution obtained from the analysis is compared with the one from high resolution measurements.

In this figure is also shown the reconstructed spectra from the analysis including the distortion introduced by the pileup and the background contamination (red line).

The result of the analysis is the feeding distribution shown in the lower panel of figure (4.9). In this case, the feeding distribution is shifted to higher excitation energies in the daughter. This is the opposite case of high resolution measurements (blue continuous line), where about half of the feeding is concentrated at low energies.

Comparing both spectra we are able to see the influence of the Pandemonium effect. This is a clear-cut case of high resolution data suffering from this effect. Many γ-rays that de-excite levels at high excitation energies remain undetected, and as a consequence, the feeding distribution is shifted to low lying levels in comparison with our results.

Despite this fact, some similarities could be found between the spectra. The structure formed by the TAGS feeding distribution has peaks at energies 2, 2.5 and 3.5 MeV. In high resolution measurements, levels have been detected with the same energies.

4.3.3 Result II: strength distribution

From the analysis, the strength distribution has been determined (figure 4.10). Also the accumulated strength is represented in figure (4.11). Up to the excitation 4268 keV which is the last known level in high resolution, the Gross theory predicts an accumulated strength value 19 times higher than high resolution data and 5 times higher than the TAGS measurement. Above this energy, additional strength is found for levels in the region where no high resolution feeding was found earlier. In the whole energy range available in the decay, the TAGS result is approximately a factor of 1.4 smaller than the predicted Gross theory strength as can be seen from figure (4.11).

Again, the sudden enhancement of the TAGS strength data for values close to the Q_β-value due to the Fermi function should be noted[3].

[3]This behaviour was previously pointed out for the strength distribution of ^{102}Tc decay.

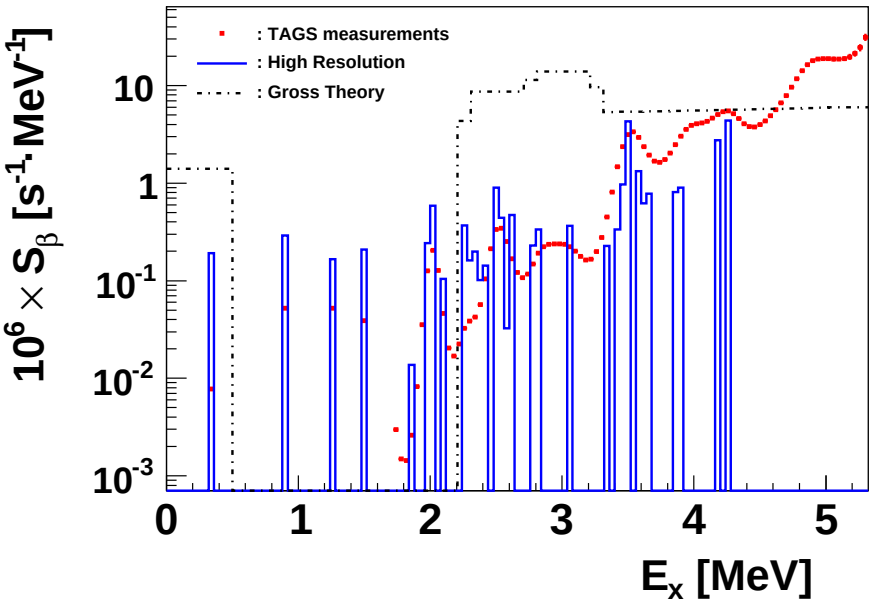

Figure 4.10: β-strength distribution for the decay of ^{104}Tc. The predicted β-strength distribution obtained with the TAGS detector is compared with the results from high resolution measurements and with calculations using Gross theory.

4.3.4 Result III: average energies

The calculated average energies for ^{104}Tc decay show differences between TAGS results and databases that are much higher than for ^{102}Tc decay. The values obtained from the analysis of the data are

$$\overline{E}_\beta = 930.83 \pm 0.04 \pm 10.00 \text{ keV}$$

$$\overline{E}_\gamma = 3229.32 \pm 0.11 \pm 24.00 \text{ keV}$$

The second error given is obtained from the comparison between the different average energies obtained from the different analyses performed. Also in this case, the assumptions made for the construction of the matrix response have an effect and, as a result,

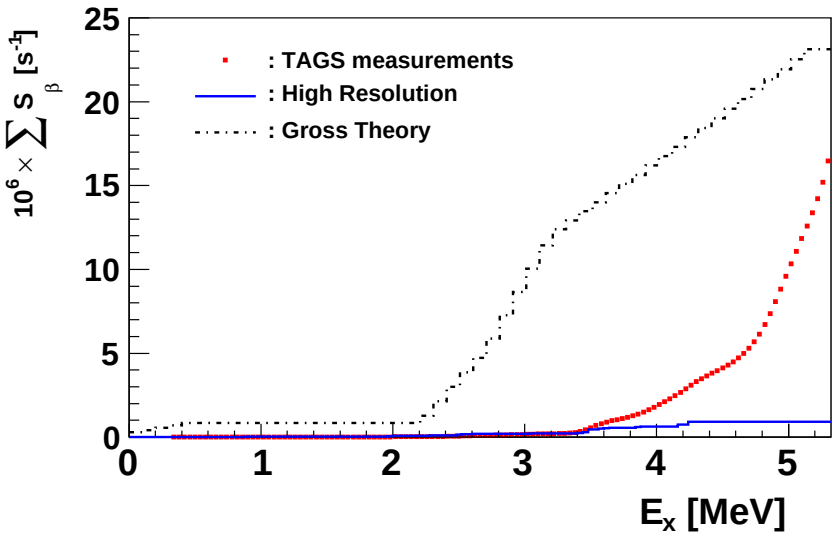

Figure 4.11: Accumulated strength distributions for the decay of ^{104}Tc.

this systematic error is higher than the error due to uncertainties in the feeding distribution.

The values given from JEFF-3.1 database are:

$$\overline{E}_\beta = 1595.11 \pm 74.98 \text{ keV}$$

$$\overline{E}_\gamma = 1889.98 \pm 30.68 \text{ keV}$$

Thus $\overline{E}_\beta$ has decreased by 664.28 keV and $\overline{E}_\gamma$ has increased by 1339.34 keV.

The large differences between these values show that the data included in the databases suffer seriously from the Pandemonium effect. It implies that $\overline{E}_\beta$ is overestimated and $\overline{E}_\gamma$ is underestimated in the databases as we have seen. The inclusion of those new values in the databases will have an impact on the problem of the γ-ray discrepancy.

4.4 ^{105}Tc decay results

4.4.1 Analysis of $^{105}Tc \rightarrow ^{105}Ru$ decay

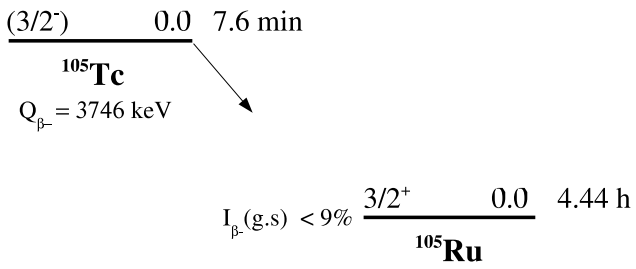

Figure 4.12: ^{105}Tc decay to ^{105}Ru.

The ^{105}Tc decay has the smallest Q_β-value of all the nuclei analyzed, 3746 keV, but at the same time, it has the highest number of predicted levels by theoretical calculations based on the statistical model, 82058. As in the ^{104}Tc case, the spin and parity of the parent ground state is in brackets, and part of the feeding goes to the ground state of ^{105}Ru as in ^{102}Tc decay. We have assumed $3/2^-$ for the ^{105}Tc ground state spin and parity. The feeding to the ^{105}Ru ground state is $< 9\%$ according to [65].

Regarding the ground state to ground state transition, it is a first forbidden transition due to the change of parity between the initial and the final states ($3/2^- \longrightarrow 3/2^+$). However, some feeding to the ground state was detected with high resolution setups. The criterion adopted in this work concerning the type of transitions considered in the decay restricts the transitions to Gamow-Teller allowed transitions. For this particular case and only for the transition ground state to ground state we made an exception: several analyses were performed varying the feeding to the ground state. We fixed the feeding to different values: zero, thus we include the possibility of no direct feeding to the ground state from the decay; and, 9%, which gives an upper limit.

For the decay of this nucleus we have uncertainties in many accepted levels in the daughter. We decided to use the known level scheme up to the excitation energy 1325.5 keV, having 16 levels of 31 with different possibilities of spin and parity. Because of the uncertainties in the level scheme, the number of possible level schemes is large, and we performed the analysis for only a few representative cases. The adopted levels with uncertainties are displayed in table (4.4). The third and fourth columns in this table contain the spins and parities of the levels for two of the level schemes considered.

E_{lev} [keV]	Adopted NDS	level scheme 1	level scheme 2
163.8	$3/2^+$,$5/2^+$	$3/2^+$	$5/2^+$
246.4	$(5/2^-, 3/2)$	$5/2^-$	$3/2^-$
272.7	$(3/2, 5/2^+)$	$3/2^+$	$5/2^+$
441.9	$3/2^+$,$5/2^+$	$3/2^+$	$5/2^+$
578.1	$(5/2^+, 3/2)$	$5/2^+$	$3/2^+$
582.1	$3/2^+$,$5/2^+$	$3/2^+$	$5/2^+$
644	$(5/2, 3/2)$	$5/2^-$	$3/2^-$
725.9	$(5/2^-, 7/2, 9/2^+)$	$7/2^+$	$5/2^-$
756.7	$3/2^+$,$5/2^+$	$3/2^+$	$5/2^+$
824.3	$3/2^+$,$5/2^+$	$3/2^+$	$5/2^+$
841.1	$7/2^+$,$9/2^+$	$7/2^+$	$9/2^+$
956.7	$(3/2, 5/2^+)$	$3/2^+$	$5/2^+$
967.1	$(1/2, 3/2, 5/2^+)$	$3/2^+$	$5/2^+$
1058.8	$(3/2^+, 5/2, 7/2^+)$	$5/2^+$	$7/2^+$
1180.1	$(3/2^+$,$5/2^+)$	$5/2^+$	$3/2^+$
1325.5	$(1/2, 3/2)$	$3/2^+$	$1/2^+$

Table 4.4: Two examples of level schemes used in the analyses. Only the levels with uncertain spins and parities are included in this table.

For the construction of the unknown part of both level schemes, we applied the statistical model in the usual way from 1360 keV up to the Q-value. It is important to mention that although we have used different level schemes, the results obtained for each case are very similar, so we decided to give the results with level scheme 2 because the χ^2 is smaller than the χ^2 from results with level scheme 1.

On the other hand, the results presented here correspond to the case where the feeding to the ground state is fixed to 9%. We decided to give this upper limit because in such way we are consistent with high resolution measurements[4]. We must keep in mind that although in this case the transition between ground states is a first forbidden transition, the known data until now for the decay of this nucleus indicate direct feeding to the ground state.

All the information about the analysis of the decay of ^{105}Tc is summarized in the next table.

Figure (4.13) shows the comparison between the reconstructed spectrum (red continuous line) and the experimental data (black dots) after the subtraction of the con-

[4]For completeness, we will also give the case where feeding is fixed to zero

Last known level	1325.5 keV
Start unknown part	1360 keV
Parent spin and parity	$3/2^-$
Background normalization factor	0.484 ± 0.007
Pileup normalization factor	$(1.42 \pm 3.33) \cdot 10^5$
Comments	level scheme 2
	^{105}Ru ground state feeding fixed to 9%

Table 4.5: Assumptions made for the ^{105}Tc decay analysis.

taminants for ^{105}Tc decay. Similar to the earlier cases, we see oscillations at the end of the spectra due to the low statistics.

4.4.2 Result I: feeding distribution

The upper panel of figure (4.14) shows a comparison between the measured spectrum including the contaminants, with the deduced spectrum after the analysis. The green dots shows the contribution of the contaminants, pileup and room background. In the lower panel of figure (4.14), the deduced feeding distribution is presented. The red dots represent the TAGS data and the blue continuous line high resolution feeding distribution (as it was already used in earlier figures). As in the ^{104}Tc case, there is a shift in the feeding distribution to higher energies compared to the high resolution result, despite the fact of the lower Q-value of the decay.

The differences between high resolution and TAGS feeding distribution will be also seen in the strength distribution and will have an important effect on the average energies.

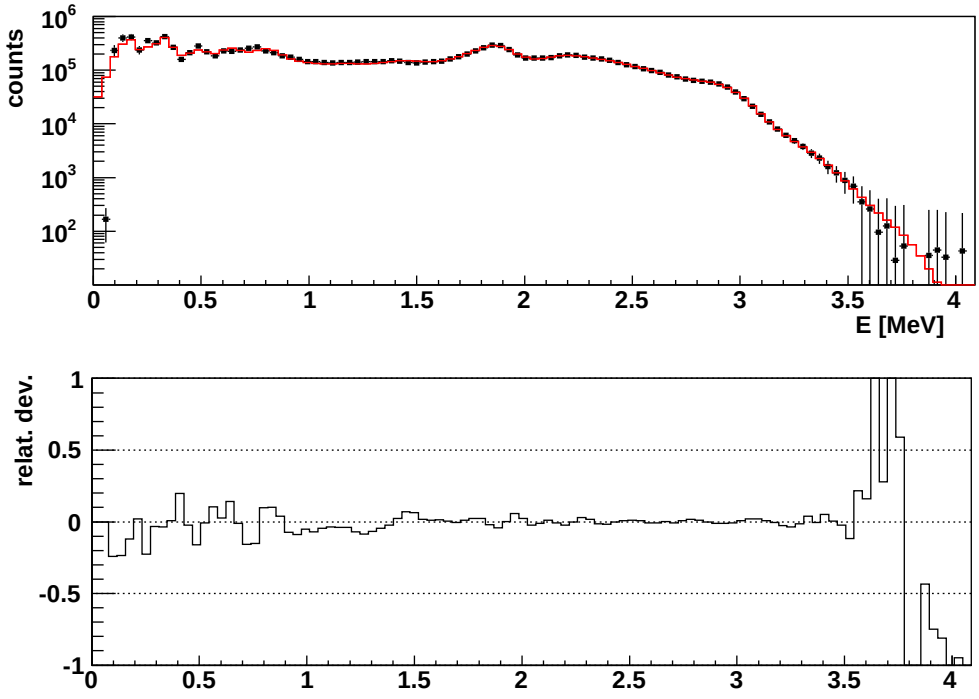

Figure 4.13: Comparison between the reconstructed spectrum (after the analysis) with the experimental data after the subtraction of the contaminants for ^{105}Tc decay. The lower panel shows the relative deviation between the spectra.

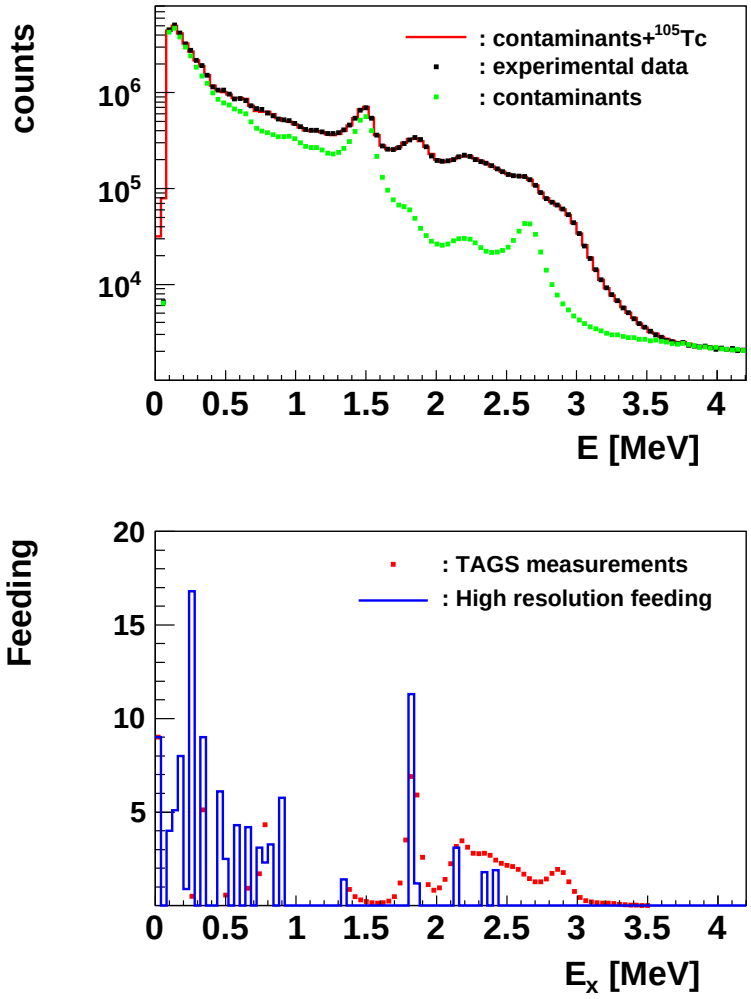

Figure 4.14: The upper panel shows the comparison of the reconstructed spectrum after the analysis with the experimental data for ^{105}Tc decay. The contribution of the contaminants is also presented in the upper panel. In the lower panel, the β-feeding distribution obtained from the analysis is compared with that from high resolution measurements.

4.4.3 Result II: strength distribution

In figure (4.15) the strength distribution deduced from the analysis is compared with the high resolution results and with the predictions of Gross theory. As far the earlier cases, the accumulated strength is presented in figure (4.16). Up to 1.7 MeV excitation energy, the TAGS results run below the high resolution results and the Gross theory predictions as can be seen from figure (4.16). In the energy range available in the decay the TAGS accumulated strength value is approximately a factor of 1.3 lower than the Gross theory prediction.

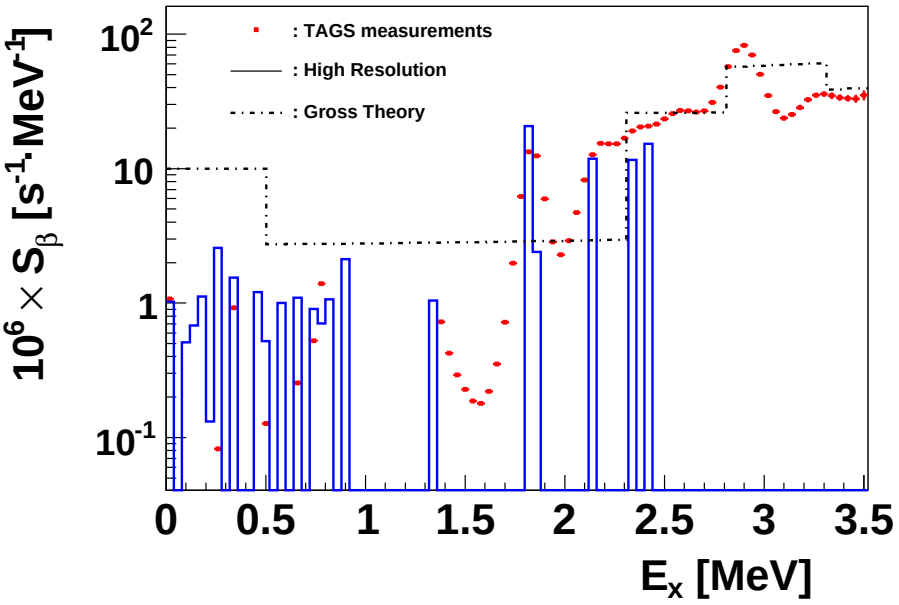

Figure 4.15: β-strength distribution for the decay of ^{105}Tc. The predicted β-strength distributions obtained with the TAGS detector is compared with the results from high resolution measurements and with calculations using Gross theory.

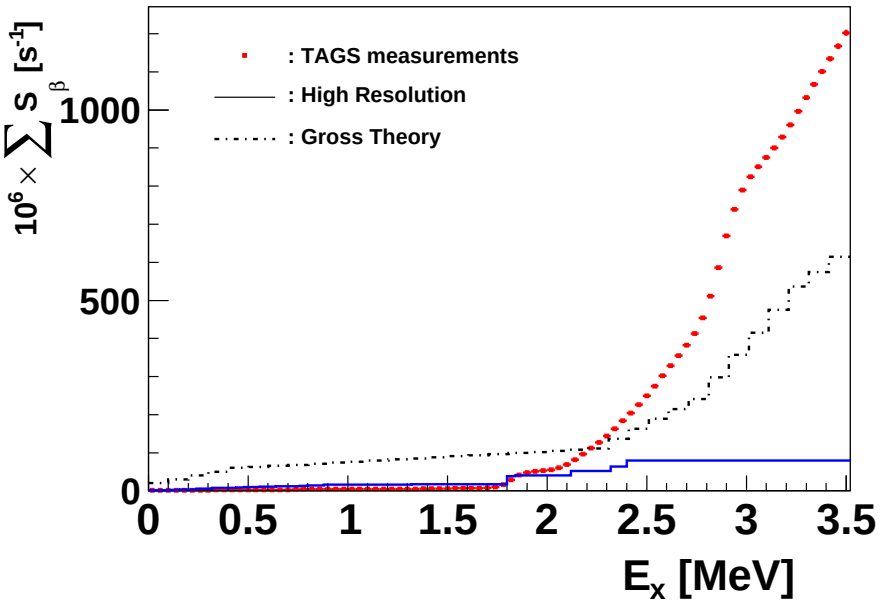

Figure 4.16: Accumulated strength distributions for the decay of ^{105}Tc.

4.4.4 Result III: average energies

The average energies obtained from the analysis described above are (ground state feeding fixed to 9%):

$$\overline{E}_\beta = 764.34 \pm 0.04 \pm 81.00 \text{ keV}$$

$$\overline{E}_\gamma = 1825.10 \pm 0.10 \pm 174.00 \text{ keV}$$

If we fix the ground state feeding to zero, the average energies are: $\overline{E}_\beta = 683$ keV and $\overline{E}_\gamma = 1999$ keV. The systematic errors come from the energy differences between different analyses.

The corresponding values given in the JEFF-3.1 database for this nucleus are:

$$\overline{E}_{\beta} = 1309.61 \pm 173.19 \text{ keV}$$

$$\overline{E}_{\gamma} = 668.42 \pm 18.98 \text{ keV}$$

The differences between TAGS and high resolution average energies are again quite relevant. The β-ray average energy has decreased by 545.27 keV and the γ-ray average energy has increased by 1156.68 keV. Those values are comparable with those obtained for the ^{104}Tc case.

The interpretation of the results is similar to that presented for ^{104}Tc decay. The increase in the γ-ray and the decrease in the β-ray average energies released in the decay are signs of high resolution data suffering from the Pandemonium effect. These results will also have an impact in the summation calculations.

4.5 ^{106}Tc decay results

4.5.1 Analysis of the $^{106}Tc \rightarrow ^{106}Ru$ decay

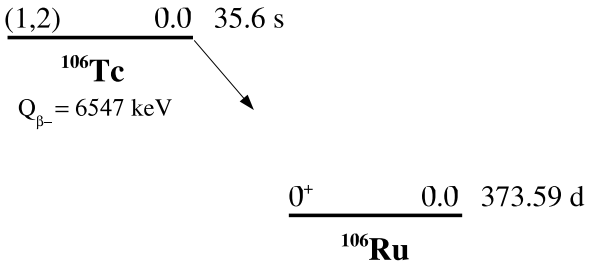

Figure 4.17: ^{106}Tc decay to ^{106}Ru.

Similar to some of the isotopes already analyzed, the ground state properties of this decaying nucleus are not well known. However, this case is even more problematic because we do not have any information about the parity and there are two possibilities for the spin. It means that we must try with both parities and both spins. Fortunately, the spin and parity of the ground state daughter nucleus, ^{106}Ru, is well known and it helps us to decide about the different analyses that have to be performed. For instance, the transition between ground states $1^+ \rightarrow 0^+$ allows direct feeding to the ^{106}Ru ground state. However, for the transition $2^+ \rightarrow 0^+$ no direct feeding is possible.

As far as the level scheme of ^{106}Ru is concerned, many uncertainties were involved and thus a large number of level schemes were possible. In this case, other difficulties also appeared. An important point for the analysis is to decide which level could be taken as the last known level. In the first instance, the level at 2239.4 keV was considered to be the last known level because there is a difference of 393.42 keV between this level and the next one in the level scheme available from reference [66]. With such an energy gap, many levels could be missing between them. However, with a cut off in the accepted known information at excitation energy 2239.4 keV the results were not satisfactory. Some unrealistic oscillations appeared. This is the reason why we decided to include the level scheme up to the energy excitation of 3550.98 keV.

With the level scheme up to 3550.98 keV, the spin-parities of only 4 levels out of 21 are free of uncertainties. On the other hand, for most of the levels with uncertainties only the spin is known and it also appears in brackets. We decided to use the level schemes of table (4.6) for the analysis.

E_{lev} [keV]	Adopted NDS	level scheme 1	level scheme 2	level scheme 3	level scheme 4
714.69	(4^+)	4^+	4^+	4^+	4^+
1091.55	(3^+)	3^+	3^+	3^-	3^-
1295.8	(6^+)	6^+	6^+	6^+	6^+
1688.41		2^+	2^+	2^-	2^-
1774.37	(2^+)	2^+	2^+	2^-	2^-
1885.61	(2^+)	2^+	2^+	2^-	2^-
1973.4	(8^+)	8^+	8^+	8^-	8^-
2239.4	(1)	1^+	2^+	1^-	2^-
2632.82	(0^+)	0^+	0^+	0^-	0^-
2701.43	(1)	1^+	2^+	1^-	2^-
2945.94	(1, 2)	1^+	2^+	1^-	2^-
3047.13	(1)	1^+	2^+	1^-	2^-
3059.53	(1)	1^+	2^+	1^-	2^-
3186.43	(1)	1^+	2^+	1^-	2^-
3259.43	(1)	1^+	2^+	1^-	2^-
3364.13	(1)	1^+	2^+	1^-	2^-
3550.98	(1)	1^+	2^+	1^-	2^-

Table 4.6: Different level schemes used in the analyses.

Each level scheme was used with both spins for the ^{106}Tc ground state. We also performed the analysis changing the parities of the daughter states and the spins of those

levels in the high resolution adopted level scheme that appear as (1). All the analyses performed are summarized in the next table:

g.s. $\pi(^{106}Tc)$	g.s. $\pi(^{106}Ru)$	level scheme
+	+	version 1 up to 2239.4 keV
−	+	version 1 up to 2239.4 keV
+	+	version 1
−	+	version 1
+	+	version 2
+	−	version 3
−	−	version 3
−	−	version 4

Table 4.7: Analyses performed for the decay of ^{106}Tc.

The analyses done with opposite parities between the ground states provided unrealistic results as was expected. For completeness, we performed the analysis of the data with negative parity for the ^{106}Ru ground state. When both parities are the same (even both negatives) the results were quite satisfactory. We obtained similar results among the analyses and with the two spins of the parent nucleus ground state, 1 and 2.

Having in mind that:

- no direct feeding to the ground state of ^{106}Ru has been noticed with high resolution measurements,
- we do not find direct feeding to the ^{106}Ru ground state in all of our analyses, even when the spin of ^{106}Tc ground state was supposed to be 1,
- the results with 1^+ and 2^+ for the ground state of ^{106}Tc are very similar,

we decided to accept as more reasonable the result of the analysis corresponding to the assignment of spin and parity 2^+ for the ^{106}Tc ground state. The last known level considered in the analysis was 3550.98 keV from high resolution measurements and the statistical model was applied from excitation energy 3600 keV up to the Q-value. The values used for normalization are given in table (4.8).

Last known level	3550.98 keV
Start unknown part	3600 keV
Parent spin and parity	2^+
Background normalization factor	0.78 ± 0.01
Pileup normalization factor	$(4.94 \pm 2.16) \cdot 10^5$
Comments	level scheme 1

Table 4.8: Assumptions made for the ^{106}Tc decay analysis.

Figure (4.18) shows the result of the reconstructed spectrum after the analysis compared with the experimental one. For both spectra the contaminants have been subtracted.

The fit of the points is quite good in almost all of the spectrum, although some differences become relevant in the first MeV (due to the subtraction of the contaminants) and at the end of the spectrum (as a result of low statistics near the Q-value). However, the tendency shown in the lower plot with the relative deviations is a smooth distribution around zero.

4.5.2 Result I: feeding distribution

The lower panel of figure (4.19) shows the feeding distribution deduced from the analysis. In this case, the last known level considered from the high resolution level scheme has a higher excitation energy than in other cases. Thus, most of the feeding is shared between the known levels taken from the high resolution level scheme (blue line). However, there is an energy gap of about 3000 keV between the last known level in the analysis and the Q-value. In this energy gap we find levels with non-zero feeding, i.e., part of the feeding is shifted to higher excitation energies from levels of lower energy in the TAGS data.

The upper panel of figure (4.19) also shows the contribution of the contaminants to the measured spectrum. Up to about 1.6 MeV, the spectrum is dominated by the contaminants (green dots). A defined structure of three peaks appears from this energy up to 3.5 MeV. The second peak coincides with the second peak found in the background (from the decay of ^{208}Tl to ^{208}Pb). The peaks are better seen in the previous figure (4.18) because the contaminants have been subtracted.

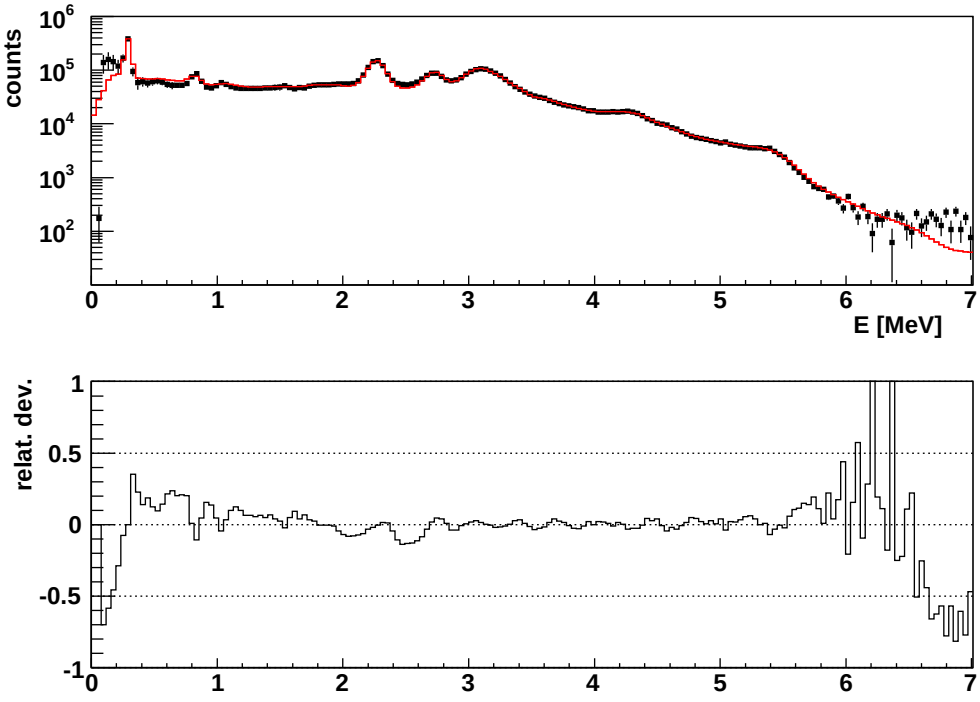

Figure 4.18: Upper panel: the comparison between the reconstructed (red continuous line) and experimental (black dots) spectra is presented for ^{106}Tc. The different contaminants have been subtracted. The lower panel corresponds to the relative deviation between both spectra.

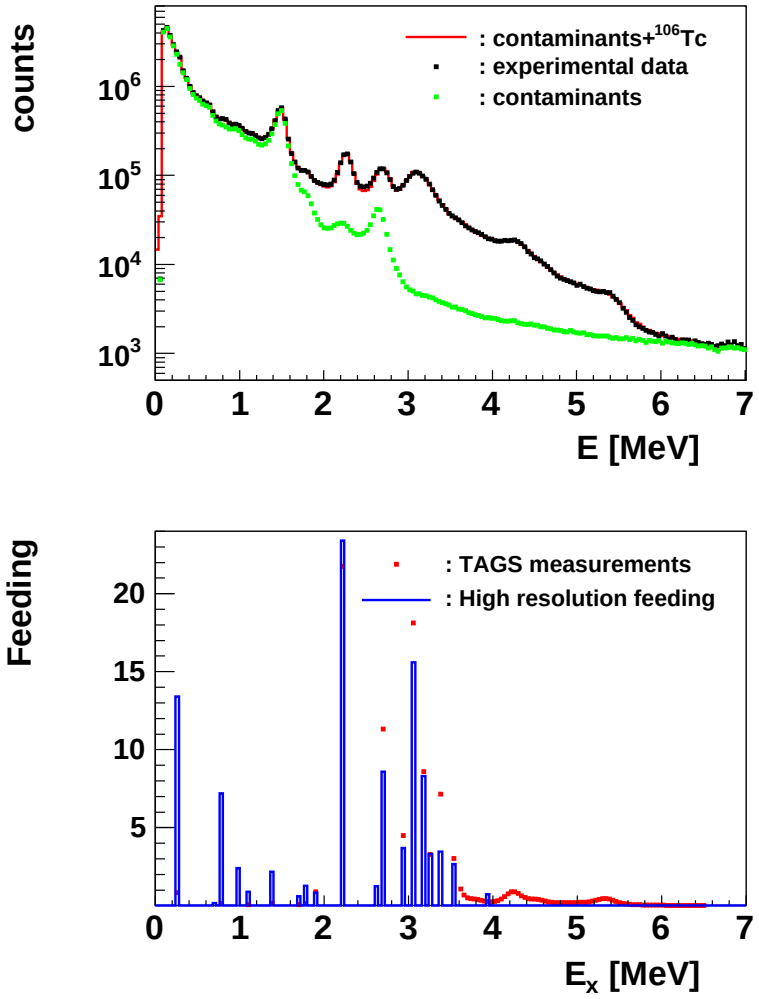

Figure 4.19: Upper panel shows the comparison of the reconstructed spectrum with the experimental data including the contaminations for the ^{106}Tc decay. The β-feeding distribution obtained from the analysis is compared with that from the high resolution measurements in the lower panel.

4.5.3 Result II: strength distribution

Figure (4.20) shows the strength distribution deduced from the analysis of the TAGS data (red dots). Figure (4.21) shows the accumulated strength. In the full energy range the TAGS accumulated strength is a factor of 1.6 higher than the Gross theory prediction and a factor of 26 higher than the high resolution result.

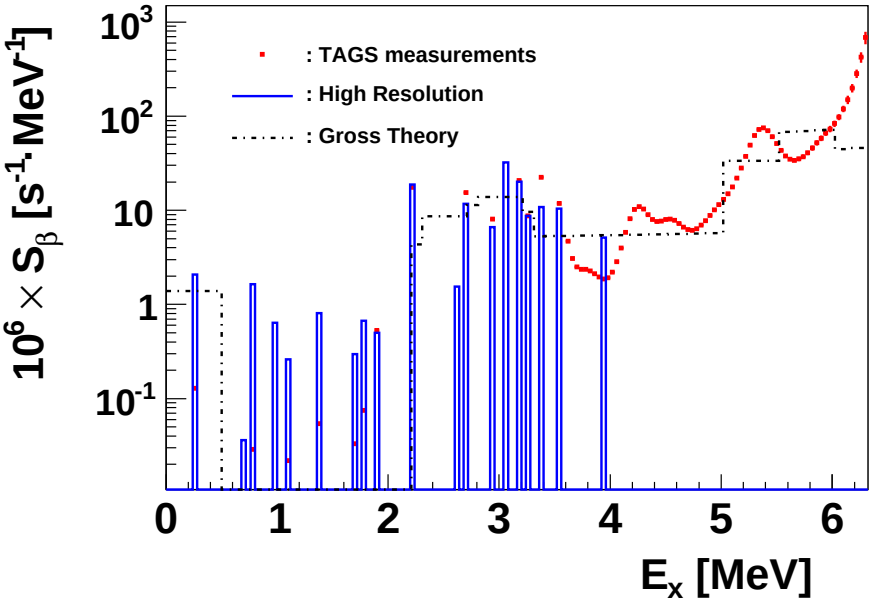

Figure 4.20: β-strength distribution for the decay of ^{106}Tc. The β-strength distributions obtained with the TAGS detector are compared with the one deduced from high resolution measurements and with the one obtained from Gross theory.

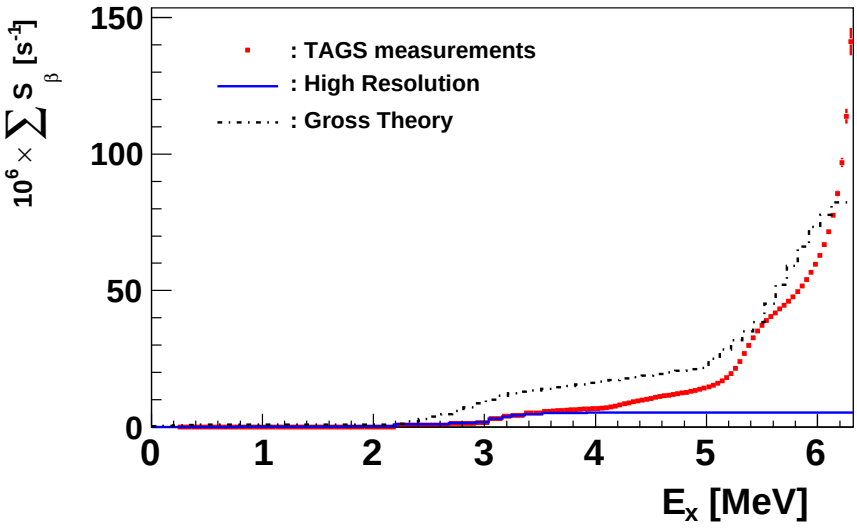

Figure 4.21: Accumulated strength distributions for the decay of ^{106}Tc.

4.5.4 Result III: average energies

The average energies deduced from the feeding distribution shown in the lower panel of figure (4.19) are:

$$\overline{E}_\beta = 1456.60 \pm 0.23 \pm 30.00 \text{ keV}$$

$$\overline{E}_\gamma = 3132.15 \pm 0.37 \pm 70.00 \text{ keV}$$

Where the systematic error in both energies is given by the largest energy difference between the analyses performed.

The same average energies in the JEFF-3.1 database have the values

$$\overline{E}_\beta = 1942.93 \pm 68.68 \text{ keV}$$

$$\overline{E}_\gamma = 2190.63 \pm 51.15 \text{ keV}$$

The β-ray average energy has decreased by 486.33 keV and the γ-ray average energy has increased by 941.52 keV. These large differences with respect to high resolution data show that the high resolution data suffer from the Pandemonium effect. The inclusion of the TAGS data in the databases will introduce a change in the γ-component of decay heat.

4.6 ^{107}Tc decay results

4.6.1 Analysis of the $^{107}Tc \rightarrow ^{107}Ru$ decay

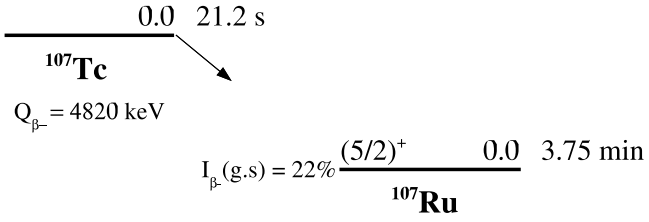

Figure 4.22: ^{107}Tc decay to ^{107}Ru.

The analysis of the decay of ^{107}Tc was not easy. The available information about this isotope is very incomplete[67]. Nothing is known about the spin and parity of the ^{107}Tc ground state and the spin of the ^{107}Ru ground state is given in brackets. The spin of the ground state of this last isotope is not a problem. We have assumed $5/2$, and the parity is well known, it is positive. However, the fact that there is no information about the spin and parity of the ^{107}Tc ground state is a problem because this information is needed for the construction of the response matrix. We have decided to perform the analysis of the experimental data assuming that the spin of the ground state is $3/2$. Regarding the parity of the ^{107}Tc ground state, we have used both possibilities for the analysis. Depending on the parent ground state parity, the daughter ground state can be directly populated or not:

- if we assume that the parity of the ^{107}Tc ground state is positive, the result is a $3/2^+ \rightarrow 5/2^+$ transition between ground states. This transition is an allowed Gamow-Teller transition, and direct feeding to the ground state of ^{107}Ru is possible.
- On the other hand, if we assume negative parity for the ^{107}Tc ground state, the transition between the ground states will be a first forbidden transition, $3/2^- \rightarrow 5/2^+$, and no direct feeding to the ground state will be possible.

E_{lev}	spin-parity assignment		feeding
[keV]	Adopted NDS	level scheme used	[%]
102.68		$3/2^+$	12
106.31		$7/2^+$	2.8
142.1		$5/2^+$	8.4
177.02		$5/2^+$	3.9
199.71	$(7/2^+)$	$7/2^+$	1.3
250.56	$(9/2^-)$	$9/2^+$	-
291.46		$5/2^+$	3.6
322.57		$7/2^+$	3.3
360.32		$5/2^+$	2.0
428.46	$(9/2^+)$	$9/2^+$	0.2
460.87		$7/2^+$	1.4
470.89		$7/2^+$	0.3
490.95		$5/2^+$	1.3
492.5		$7/2^+$	1.2
561.35		$3/2^+$	3.2
582.46		$5/2^+$	1.1
585.94		$7/2^+$	1.0
631.95	$(13/2^-)$	$3/2^+$	1.4
698.27		$3/2^+$	2.4
713.71		$5/2^+$	0.6
741.42		$5/2^+$	1.7
807.25		$7/2^+$	2.8
825.94		$5/2^+$	1.2
894.06		$5/2^+$	0.8
900.23		$7/2^+$	0.7
923.2		$5/2^+$	1.0
957.09		$7/2^+$	0.4

Table 4.9: Possible assignment of spins and parities to the levels of ^{107}Ru. The fourth column shows the known feeding from high resolution measurements[67].

However, from high resolution measurements, we know that the ground state of ^{107}Ru is directly populated and according to [67] it is 22%. Two kinds of analysis were performed, one leaving the feeding to the ground state free and another one fixing this value to 22%. At this point is important to mention an additional problem that we had to face with the analysis of this nucleus. This problem is the lack of information about spins and parities of the levels found means of high resolution measurements. In fact, this problem affected the analysis because the construction of the response matrix requires a good knowledge of the level scheme. In such a situation, we tried to assign

spins and parities to the level scheme as shown in table (4.9) from the high resolution measurements.

For the assignment of spin-parities to the levels we took into account the type of transitions between the levels (electric or magnetic transitions or a mixture of both) so we selected spins and parities depending on that where possible. The level scheme constructed in such way is only one of many possible level schemes.

In the high resolution level scheme, almost all the levels have direct feeding with one exception, the level with excitation energy 250.56 keV (see table (4.9)). However, with the chosen spin of the ^{107}Tc ground state and assuming only allowed Gamow-Teller transitions, not all the levels can have direct feeding. Thus, we decided to perform the following analyses:

$J^{\pi}(^{107}Tc)$	comments
$3/2^-$	all levels without feeding (no direct feeding to ground state)
$3/2^+$	only allowed transitions have feeding. Feeding to ground state free.
$3/2^-$	all known levels with feeding (including forbidden transitions). Feeding to ground state free.
$3/2^-$	all levels without feeding, except g.s., feeding fixed to 22%
$3/2^+$	only allowed transitions have feeding. g.s. feeding fixed to 22%
$3/2^-$	all known levels with feeding (including forbidden transitions). g.s. feeding fixed to 22%

Table 4.10: Analyses performed for ^{107}Tc decay.

Table (4.11) contains the assumptions made for the analysis with the best fit whose results are presented in this work. It corresponds precisely to the values given in the literature, i.e., ground state feeding fixed to 22% and all the levels with feeding. The last accepted known level from the high resolution scheme was at the excitation energy of 957.09 keV. From this excitation energy on the energy gap between the known levels increases, raising the possibility of missing levels. This is the reason why we decided to use only the known levels up to this excitation. The start of the unknown part was placed at 1020 keV, and the statistical model was applied from this energy up to the Q-value.

Last known level	957.09 keV
Start unknown part	1020 keV
Parent spin and parity	$3/2^-$
Daughter spin and parity	$5/2^+$
Background normalization factor	2.13 ± 0.02
^{107}Ru contamination normalization factor	6.47
Comments	pileup contribution very small, not included in the analysis
	^{107}Ru ground state feeding fixed to 22%
	all the levels with feeding

Table 4.11: Assumptions made for the ^{107}Tc decay analysis.

At this point, a comment is necessary about the pileup distortion introduced by the electronics. In this case, this distortion has not been taken into account in the analysis. In the data analysis chapter, it was shown how to use the β-gated coincidence spectrum for the determination of the normalization factors. The β-gated coincidence spectrum for ^{104}Tc decay was compared with the measured spectrum once the contaminations (properly scaled) were subtracted. In this particular case there is practically no difference in comparison with the situation without including pileup. This is the reason why we decided not to include the pileup distortion in the analysis.

The reconstructed spectrum (free of contaminants) obtained with this analysis is shown in figure (4.23). Despite the fact that we have used one possible combination of spins and parities for the level scheme and forced the feeding to the ground state of ^{107}Ru to be 22%, the global fit is not so bad. If we focus our attention on the central part of the spectrum plotted in the upper panel of this figure we see that the fit is almost perfect from 2.3 MeV to 4 MeV. From 0.5 MeV to 2.3 MeV, the red fitted line (reconstructed spectrum) runs very close to the experimental data but some points of the experimental data are distributed around the fit. This is reflected in the small oscillations in the lower panel of figure (4.23).

Large differences in the fit of the spectrum appear in the first 400-500 keV, where the contaminants have more influence, and also at the end of the spectrum, where the statistics are low. The fit at energies lower than 500 keV is a problem because several levels are concentrated at these excitation energies. The fit could not be improved (even taking into account the pileup distortion) and in this part of the spectrum it runs below the experimental data (black dots). This tendency was also present in the rest of analyses performed.

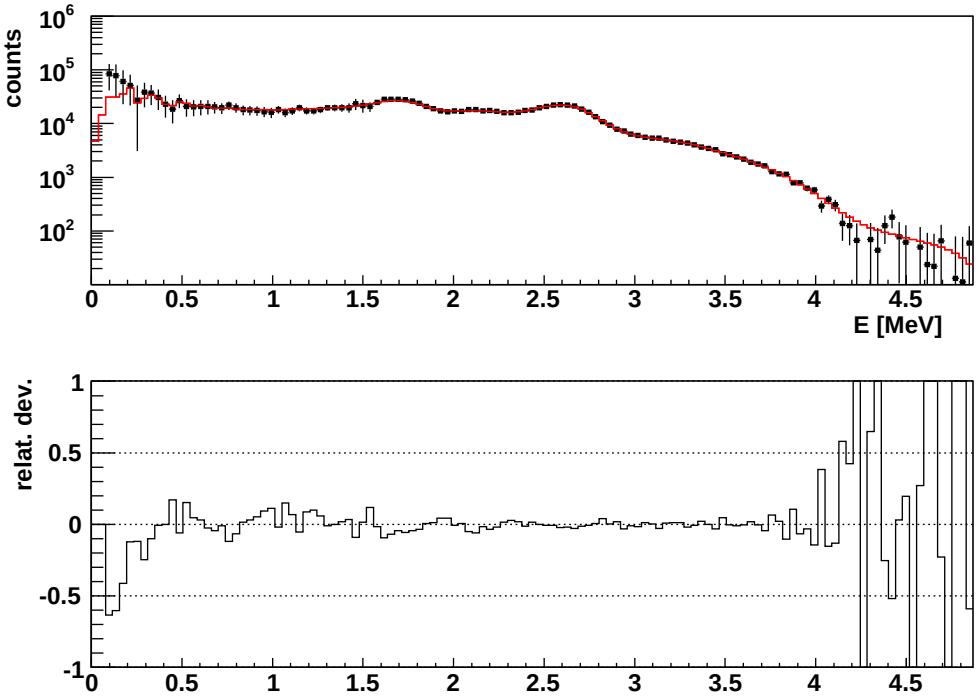

Figure 4.23: In the upper panel is shown the comparison between the reconstructed (red continuous line) and experimental (black dots) spectra once the different contaminants have been subtracted for ^{107}Tc. The lower panel corresponds to the relative deviation between the spectra.

4.6.2 Result I: feeding distribution

The feeding distribution deduced from the analysis of the experimental data is shown in the lower panel of figure (4.24). The TAGS feeding distribution is very different from the high resolution feeding distribution. According to reference [67], 35.3 % of the feeding is shared between the levels below 350 keV. If we include the feeding that goes to the ground state of ^{107}Ru (22%), it means that 57.3 % of the feeding is concentrated at very low energies.

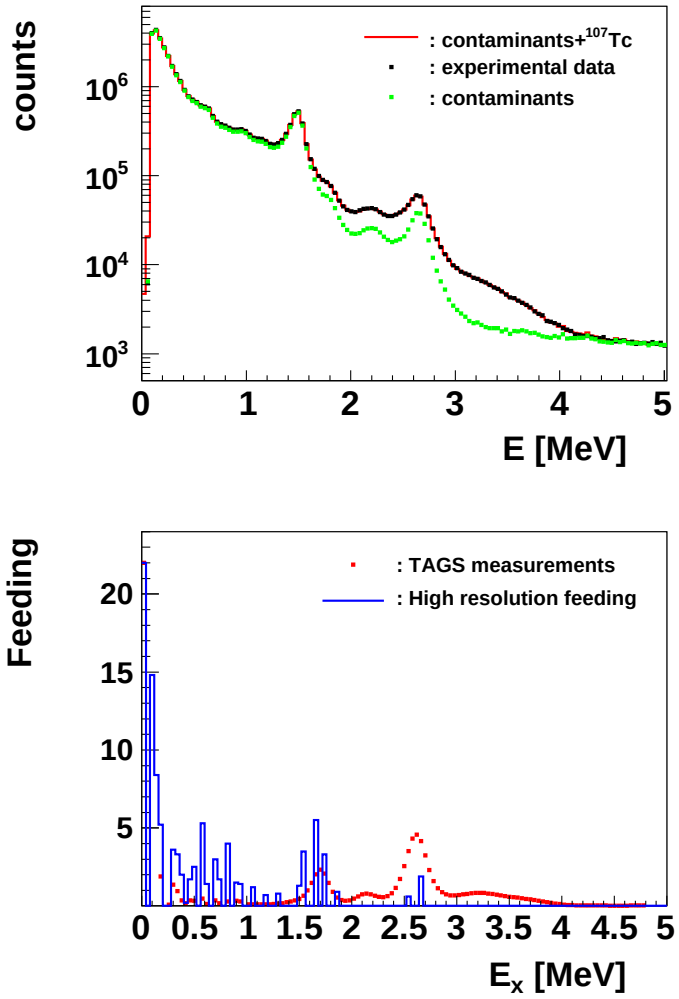

Figure 4.24: Upper panel shows the comparison of reconstructed and experimental data including the contaminations for the ^{107}Tc decay. Also in the upper panel the contribution of the contaminants is shown. The TAGS β-feeding distribution is shown in the lower panel compared with that from high resolution measurements.

There are clear differences in the feeding distributions of figure (4.24). The levels seen from high resolution at approximately 0.5 MeV excitation receive less feeding in the TAGS data. A "resonant like" feeding is seen at excitation 1.7 and 2.6 MeV in the TAGS data, which is confirmed by the existence of levels fed in high resolution data. Some feeding seen in high resolution at 0.6 and 1.5 MeV, respectively, is shifted to high excitation energies. The last fed level in high resolution is at excitation 2679.67 keV. The TAGS data show sizable feeding up to 4 MeV.

4.6.3 Result II: strength distribution

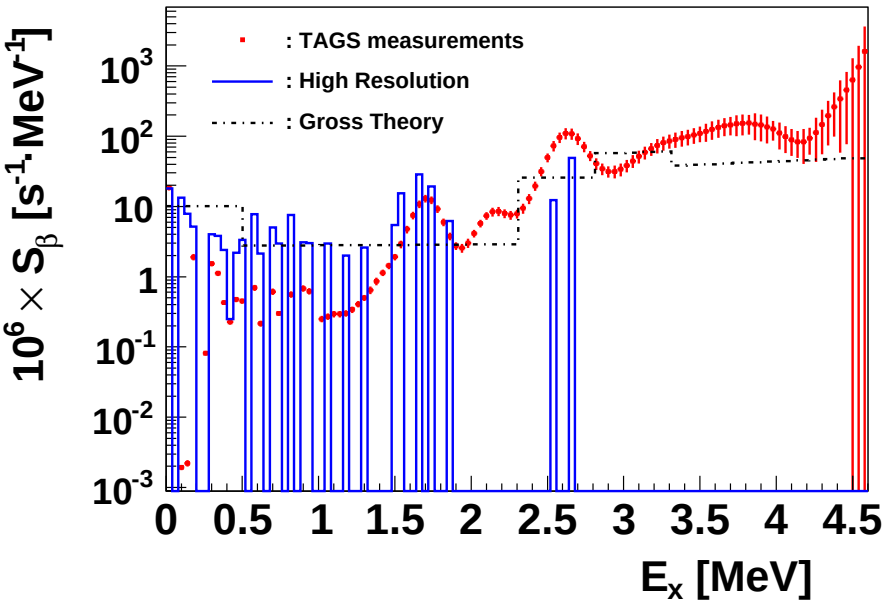

Figure 4.25: β-strength distribution for the decay of ^{107}Tc. The β-strength distribution obtained with the TAGS detector is compared with that deduced from high resolution measurements and the one obtained from Gross theory.

Figure (4.25) shows three different strength distributions: the one deduced from the analysis of the TAGS data (red dots), the high resolution strength distribution (blue continuous line), and the strength obtained from Gross theory (black dashed line). The figure (4.26) shows the corresponding accumulated strength distributions. The three ac-

cumulated strength distributions differ. The accumulated TAGS strength in the available energy range is approximately 3 times higher than the prediction of the Gross theory.

The errors in the TAGS strength distribution are strongly enhanced at the end of the spectrum. This effect was not so pronounced in other isotopes.

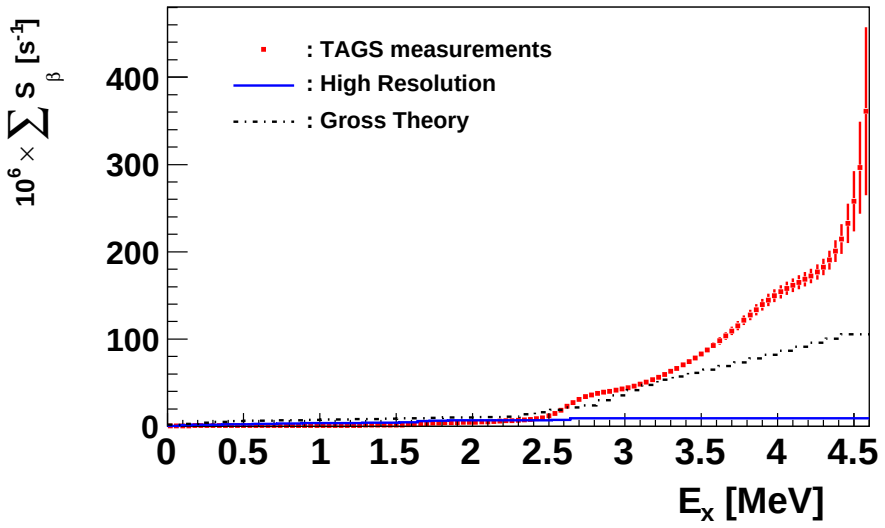

Figure 4.26: Accumulated strength distributions for the decay of ^{107}Tc.

4.6.4 Result III: average energies

From the analysis the following average energies were deduced:

$$\overline{E}_\beta = 1263.03 \pm 0.09 \pm 212.00 \text{ keV}$$

$$\overline{E}_\gamma = 1822.07 \pm 0.18 \pm 450.00 \text{ keV}$$

In this case, the large systematic error comes from the differences between the average energies obtained with the different possible analyses using other assumptions (see

table 4.11). The systematic errors are higher than the systematic errors associated with other isotopes analyzed in the same way. The uncertainties associated with the high resolution level scheme and with the dependence on the assumptions made for the construction of a possible level scheme have a strong influence in the determination of the average energies and their errors. In this case, we can easily see how the decisions taken for the construction of the response matrix play an important role in the analysis of the data.

If we do not include the daughter activity contamination (^{107}Ru decay) the analysis gives $\overline{E}_\beta = 1275.50$ keV and $\overline{E}_\gamma = 1795.36$ keV. The ^{107}Ru decay contamination amounts to 12.97% as was mentioned earlier (section 3.3.4).

On the other hand, if we compare these values with the average energies taken from JEFF-3.1 database

$$\overline{E}_\beta = 2055.69 \pm 254.10 \text{ keV}$$

$$\overline{E}_\gamma = 514.78 \pm 10.90 \text{ keV}$$

we see that the β-ray average energy has decreased 792.66 keV, and the γ-ray average energy has increased 1307.29 keV. The effect obtained is the same noted for the other nuclei studied. The results obtained from high resolution data underestimate the γ-ray average energy and overestimate the β-ray average energy.

4.7 ^{101}Nb decay results

4.7.1 Analysis of the $^{101}Nb \rightarrow ^{101}Mo$ decay

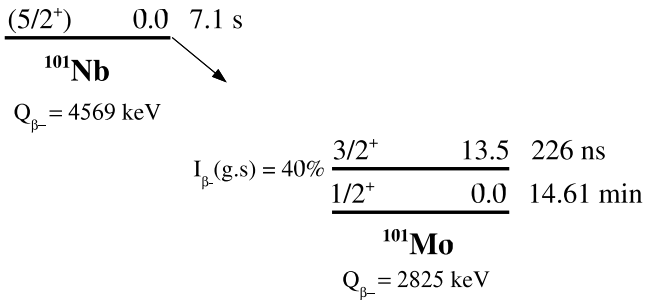

Figure 4.27: ^{101}Nb decay to ^{101}Mo.

Figure (4.27) shows the decay of ^{101}Nb into ^{101}Mo. In this case, there is no direct feeding to the ground state of the daughter nucleus but the first excited state is placed very close to the ground state (its excitation energy is 13.5 keV) and it has a direct feeding of 40%. With the TAGS detector we are not able to separate these levels.

The knowledge of the ^{101}Mo level scheme from high resolution measurements is relatively complete. The levels fed in the decay have in general well defined spin and parity[60], with the exception of only a few levels that have several spin/parity values or the spin and/or parity appear in brackets. The spin and parity of the ^{101}Nb ground state also appears in brackets. We have assumed $5/2^+$ in the analysis.

The last known level considered in the analysis has an excitation energy of 479.78 keV and the statistical model was applied from 520 keV up to the Q-value. With the level scheme up to this energy, the number of levels with uncertainties is reduced to the levels with excitation energy 237.73 keV and 315 keV. For both levels, two possible spin-parities are given. Thus, four level schemes were used, one for each possible combination of spin-parities. We decided not to add more levels to the used known part in order to minimize the uncertainties because the number of possibilities in the high resolution data for the decay of this isotope increases with if the known part limit is shifted to higher excitation energies.

The following table, table (4.12) contains the information about the assignment of spin-parities to the different level schemes.

E_{lev} $[keV]$	Adopted NDS	level scheme 1	level scheme 2	level scheme 3	level scheme 4
13.5	$3/2^+$	$3/2^+$	$3/2^+$	$3/2^+$	$3/2^+$
57.01	$5/2^+$	$5/2^+$	$5/2^+$	$5/2^+$	$5/2^+$
170.98	$5/2^+$	$5/2^+$	$5/2^+$	$5/2^+$	$5/2^+$
237.73	$3/2^+, 5/2^+$	$3/2^+$	$3/2^+$	$5/2^+$	$5/2^+$
240.50	$7/2^+$	$7/2^+$	$7/2^+$	$7/2^+$	$7/2^+$
289.53	$3/2^+$	$3/2^+$	$3/2^+$	$3/2^+$	$3/2^+$
294.59	$1/2^+$	$1/2^+$	$1/2^+$	$1/2^+$	$1/2^+$
315.00	$7/2, 9/2^+$	$7/2^+$	$9/2^+$	$7/2^+$	$9/2^+$
318.86	$5/2^+$	$5/2^+$	$5/2^+$	$5/2^+$	$5/2^+$
351.59	$3/2^+$	$3/2^+$	$3/2^+$	$3/2^+$	$3/2^+$
454.55	$5/2^+$	$5/2^+$	$5/2^+$	$5/2^+$	$5/2^+$
479.78	$3/2^+$	$3/2^+$	$3/2^+$	$3/2^+$	$3/2^+$

Table 4.12: Summary of the level schemes used in the analysis of the decay of ^{101}Nb.

For each level scheme, we performed one analysis leaving the feeding to the first excited state free. The differences in the results with all the level schemes used were minimal so we decided to perform an additional analysis fixing the feeding to the first excited state to 40% using one of the level schemes available, for example the first one. The analysis fixing the feeding fairly differ from the previous ones. The analyses done leaving the first excited state free give a value for the feeding to this state close to zero, and in general, the feeding distribution was very different from high resolution measurements. Thus we decided to present the results obtained with the analysis where the feeding to the first excited state was fixed to 40%. For completeness, the values obtained when the feeding to the first excited state was left free will also be given. The analysis performed with the condition of leaving the ground state feeding free gives a slightly better χ^2 value than the one performed with the feeding fixed to 40%.

On the other hand, it must be noticed that the pileup contribution was not included in the contaminant spectrum and then not taken into account in the analysis of the data, as happened for ^{107}Tc decay. The explanation is the same. The pileup distortion introduced by the electronics was very small and there was practically no effect in the spectrum when this contaminant was introduced.

Table (4.13) summarises the assumptions made in the analysis.

Last known level	479.78 keV
Start unknown part	520 keV
Parent spin and parity	$5/2^+$
Background normalization factor	3.44 ± 0.04
Comments	pileup contribution very small, not included in the analysis
	feeding to first excited level (13.5 keV) fixed to 40%
	level scheme 1

Table 4.13: Assumptions made for the analysis of ^{101}Nb decay.

The reconstruction obtained with this analysis of the experimental data is given in the upper panel of figure (4.28). In this case, the reconstructed spectrum (red continuous line) fits extremely well the experimental spectrum (black dots) at low energies, where the influence of the contaminants has the maximum effect. The relative deviation between both spectra, free of contaminants, oscillates a little around zero, but those oscillations are quite small[5]. The fit is worse around 1500 keV, but no level has been found with high resolution measurements from the decay of ^{101}Nb.

4.7.2 Result I: feeding distribution

We have previously mentioned the fact that no pileup distortion was added to the contaminant spectrum. In the upper panel of figure (4.29) we can see the background contribution (green dots) in the experimental spectrum (black dots). The red continuous line is the fit including the background contribution to the experimental data.

The lower panel of the same plot is the result of the analysis, the feeding distribution. The one obtained by us is represented by red dots, and in blue, the high resolution feeding distribution is presented. Both distributions are very close at low energies (below than 1 MeV).

From 1099 keV on, there are no levels detected in high resolution measurements. If we take into account that the Q-value of the decay for this isotope is 4569 keV, it means that we have an energy gap of 3470 keV where no feeding was detected. The number of possible missing levels could be quite high[6] so this isotope is probably suffering from the Pandemonium effect. In fact, we detect feeding at high excitation energies, concentrated

[5] We must have in mind that the upper panel of figure (4.28) is plotted in log scale so the differences are not well seen in this type of graphs.

[6] The number of total levels predicted for this isotope of 4537.

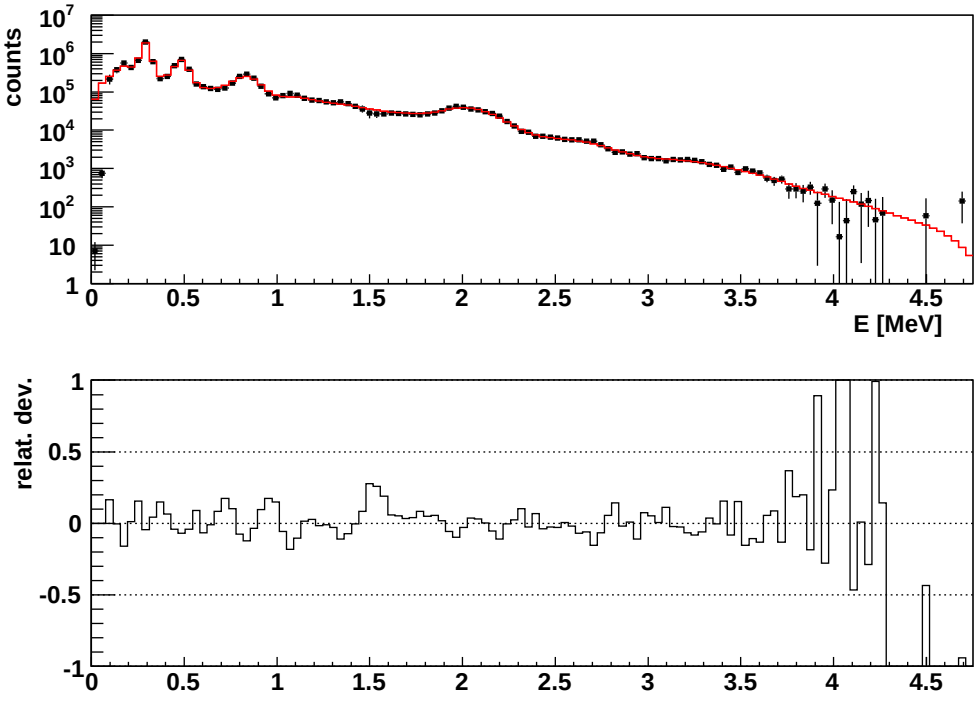

Figure 4.28: Upper panel: the comparison between the reconstructed (red continuous line) and experimental (black dots) spectra is shown once the different contaminations have been subtracted for ^{101}Nb decay. The lower panel corresponds to the relative deviation between the spectra.

in an small region of 300 keV centred at approximately 2 MeV. The proportion is not high, because about 78 % of the feeding is assigned to the levels with excitation energy 13.5 keV, 289.53 keV, 454.55 keV and 479.78 keV.

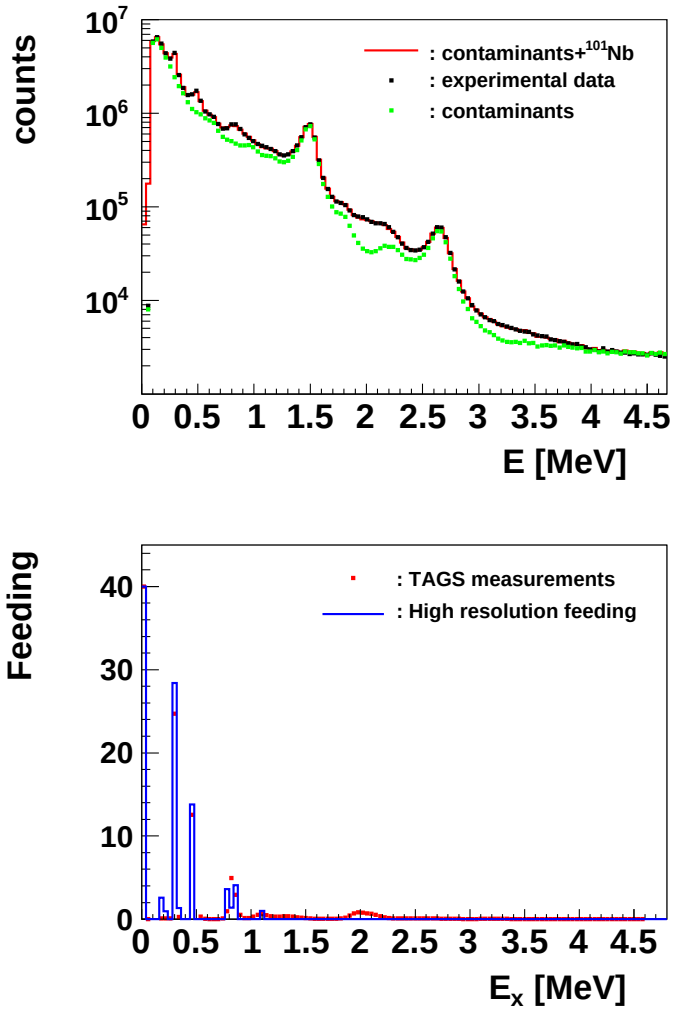

Figure 4.29: Upper panel shows the comparison of reconstructed and experimental data including the contaminations for ^{101}Nb decay. The contribution of the contaminants is also shown in the upper panel (green dots). The β-feeding distribution obtained from the experiment is compared with that deduced from high resolution measurements in the lower panel.

4.7.3 Result II: strength distribution

The strength distribution deduced from the analysis is presented in figure (4.30). In the same figure we also present the strength distributions deduced from high resolution data and the Gross theory. In figure (4.31) the accumulated strength of the three distributions is presented. Up to 1.8 MeV excitation energy, the TAGS distribution and the high resolution distribution are similar and they run above the Gross theory prediction. In the energy range available in the decay, the TAGS accumulated strength is 1.4 times higher than the Gross theory prediction and approximately 7 times higher than the high resolution value.

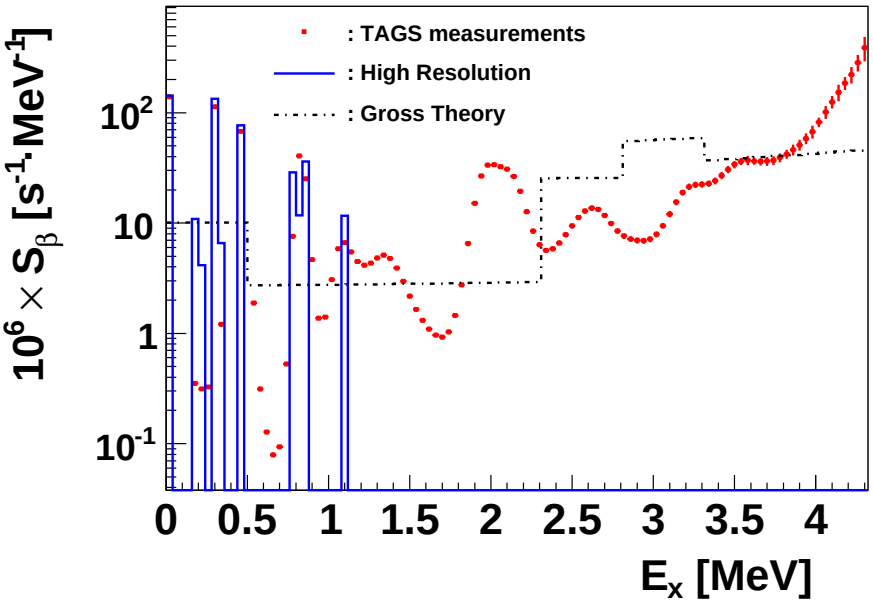

Figure 4.30: β-strength distributions for ^{101}Nb decay. The β-strength distribution obtained with the TAGS detector is compared with that deduced from high resolution measurements and with the one obtained from Gross theory.

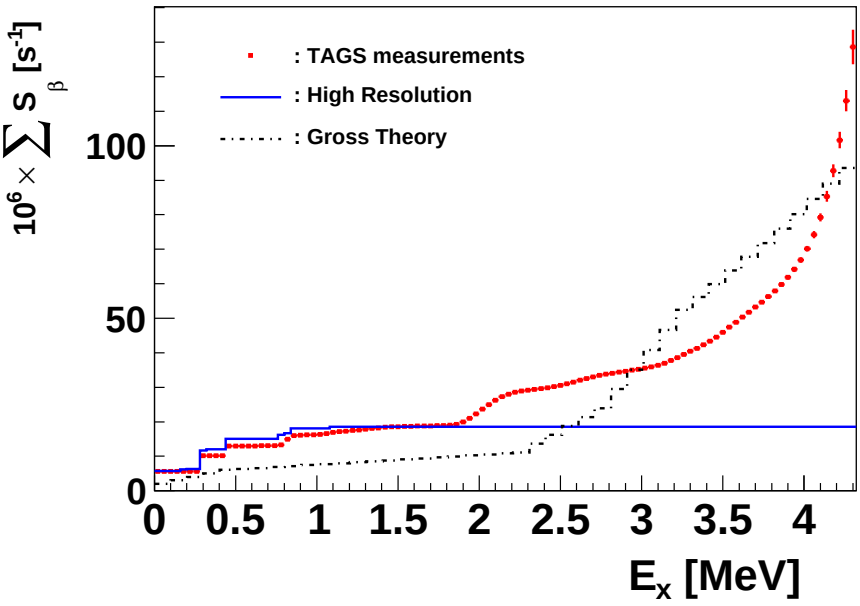

Figure 4.31: Accumulated strength distributions for the decay of ^{101}Nb.

4.7.4 Result III: average energies

Finally, the average energies deduced from the analysis presented here have the following values

$$\overline{E}_\beta = 1796.50 \pm 0.16 \pm 133.00 \text{ keV}$$

$$\overline{E}_\gamma = 445.04 \pm 0.03 \pm 279.00 \text{ keV}$$

The average energies when the feeding to the first excited state was left free are (level scheme 1): $\overline{E}_\beta = 1664$ keV and $\overline{E}_\gamma = 724$ keV. The energy differences between different analyses determine the systematic error quoted.

As in the ^{102}Tc case, large differences are not expected in the average energies between TAGS and the JEFF-3.1 database. In fact, the average energies in this database

have the values

$$\overline{E}_{\beta} = 1863.35 \pm 306.75 \text{ keV}$$

$$\overline{E}_{\gamma} = 244.57 \pm 21.78 \text{ keV}$$

It means that the β-ray average energy has decreased only by 66.85 keV, and the γ-ray average energy has increased by 200.47 keV. These quantities are small compared with the average energy differences obtained for other isotopes such as ^{104}Tc or ^{105}Tc. However, the initial conditions are not the same. We must remember the fact that experimentally most of the high resolution feeding is concentrated at low energies, as in the case of ^{102}Tc decay, but some small amount of feeding was detected at approximately 2 MeV excitation in the TAGS data.

4.8 ^{105}Mo decay results

4.8.1 Analysis of $^{105}Mo \rightarrow ^{105}Tc$ decay

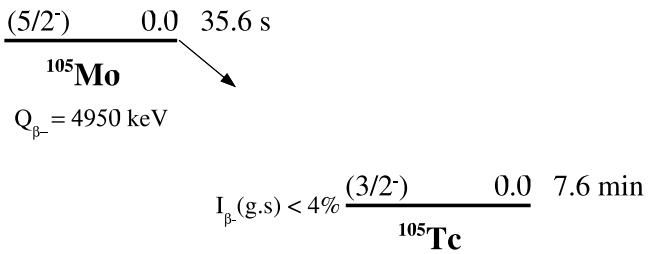

Figure 4.32: ^{105}Mo decay to ^{105}Tc.

The decay of ^{105}Mo to ^{105}Tc is very similar to the decay of ^{105}Tc into ^{105}Ru. In both decays, there are uncertainties in the spin and parity of the parent ground state and the ground state of the daughter nucleus is directly populated. The feeding to the daughter ground state is not well known. In both cases an upper limit is given. In this case, the feeding to the ground state of ^{105}Tc is quoted in [65] as being less than 4%. With respect to the spin and parity of ^{105}Tc ground state, we can use the value deduced from the analysis of the data for ^{105}Tc decay, $3/2^-$. Then, if we assume $5/2^-$ for the spin and parity of the ^{105}Mo ground state, the ^{105}Tc ground state could be directly populated in our analysis.

E_{lev} $[keV]$	Adopted NDS	level scheme 1	level scheme 2
76.58	$(5/2^-)$	$5/2^-$	$5/2^-$
85.43	$(5/2^+)$	$5/2^+$	$5/2^+$
147.76	$(5/2^-)$	$5/2^-$	$5/2^-$
149.61	$(7/2^+)$	$7/2^+$	$7/2^+$
237.03	$(7/2^-)$	$7/2^-$	$7/2^-$
249.62	$(3/2^-,5/2^-)$	$3/2^-$	$3/2^-$
278.60	$(9/2^+)$	$9/2^+$	$9/2^+$
303.76	$(3/2^+)$	$3/2^+$	$3/2^+$
322.17	$(1/2^+)$	$1/2^+$	$1/2^+$
345.68	$(7/2^-)$	$7/2^-$	$7/2^-$
440.90	$(9/2^-)$	$9/2^-$	$9/2^-$
463.63		$5/2^-$	$5/2^-$
491.43	$(7/2^+)$	$7/2^+$	$7/2^+$
523.75		$5/2^-$	$5/2^-$
530.00	$(5/2^+)$	$5/2^+$	$5/2^+$
558.74		$7/2^-$	$7/2^-$
563.77		$7/2^+$	$7/2^+$
610.28		$5/2^+$	$5/2^+$
810.31		$7/2^+$	$7/2^+$
868.87		$9/2^+$	$9/2^+$
880.89	$(9/2^+)$	$9/2^+$	$9/2^+$
891.59	$(9/2^+)$	$9/2^+$	$9/2^+$
940.45		$7/2^-$	$7/2^-$
1043.31		$5/2^-$	$5/2^-$
1172.12		$5/2^+$	$5/2^+$
1415.10		$5/2^+$	$5/2^+$
1476.37		$3/2^-$	$3/2^+$
1819.80		$7/2^-$	$7/2^-$
1890.80		$5/2^-$	$5/2^+$
2195.20		$5/2^-$	$5/2^-$
2211.97		$7/2^+$	$7/2^+$
2766.43		$7/2^-$	$7/2^-$

Table 4.14: The level scheme adopted by the NDS for the decay of ^{105}Mo to ^{105}Tc is presented in column 2. Columns 3 and 4 summarize the level schemes used in the analysis. The differences between them correspond to the levels with excitation energy 1476.37 keV and 1890.80 keV.

The known level scheme available from ENSDF contains the levels presented in table (4.14). Fifteen of the 32 levels are in brackets and the rest have no information available. The situation is similar to the one faced for ^{107}Tc decay analysis. Thus, as we did in the analysis of ^{107}Tc data, we assigned spin and parities to levels using a knowledge of the types of transition between the levels. The result is shown in table (4.14). Two level schemes were developed in such a way. The differences between both level schemes lie in the parities of the levels with excitation energies 1476.37 keV and 1890.80 keV.

Once we have some possible level schemes for the decay of this isotope, we must decide which is the last level in which we have confidence. The last known level from high resolution is at an excitation energy of 2766.43 keV. Several energy gaps of some hundreds of keV could be noticed in the level scheme given by the nuclear data sheets. For the analysis, we decided to consider those energy gaps as a signal of where to cut in the level scheme.

We used those level schemes up to 610.28 keV, 1172.12 keV, 1476.37 keV and 2766.43 keV. In the next table all the analyses performed are summarized, including where the unknown part starts in each of them. In 6 of the 8 analyses, the feeding to the ground state was left free. In the other two cases, it was fixed to 4% in order to give an upper limit.

level scheme	start unknown part	feeding to ground state
up to 1172.12	1240	free
1	2800	free
2	2800	free
1 up to 1476.37	1520	free
2 up to 1476.37	1520	free
up to 610.28	660	free
1 up to 1476.37	1520	fixed to 4%
up to 610.28	660	fixed to 4%

Table 4.15: Analyses performed for ^{105}Mo decay.

We present here the analysis corresponding to feeding to the ground state of ^{105}Tc fixed to 4%, a known level scheme up to 1476.37 keV and the statistical model applied from 1520 keV up to the Q-value (see table (4.16)).

We decided to show the results of this analysis because of the following reasons:

- the fit where the level scheme from high resolution is introduced up to 1476.37 is

Last known level	1476.37 keV
Start unknown part	1520 keV
Parent spin and parity	$5/2^-$
Daughter spin and parity	$3/2^-$
Background normalization factor	0.301 ± 0.003
Pileup normalization factor	$(1.50 \pm 0.84) \cdot 10^5$
^{105}Tc contamination normalization factor	0.12
Comments	^{105}Tc ground state feeding fixed to 4%

Table 4.16: Assumptions made for the analysis of ^{105}Mo decay.

better than for the other cases (it has the minimum χ^2, 37845). The fit could be seen in figure (4.33).

- The feeding to the ground state of ^{105}Tc in the nuclear data sheet is less than 4% so the average energies deduced from this analysis will represent an upper limit.
- The feeding to the ground state of ^{105}Tc obtained from the analysis was in all cases zero, even when this feeding was left free.

In figure (4.33), the relative deviation deduced from the upper panel shows a smooth distribution around zero. The effect of subtractions can be checked in the first 500 keV, where some oscillations in the lower panel of this figure appear. The reconstruction (red continuous line) in this part runs below the experimental data (black dots). But the overall result is quite good.

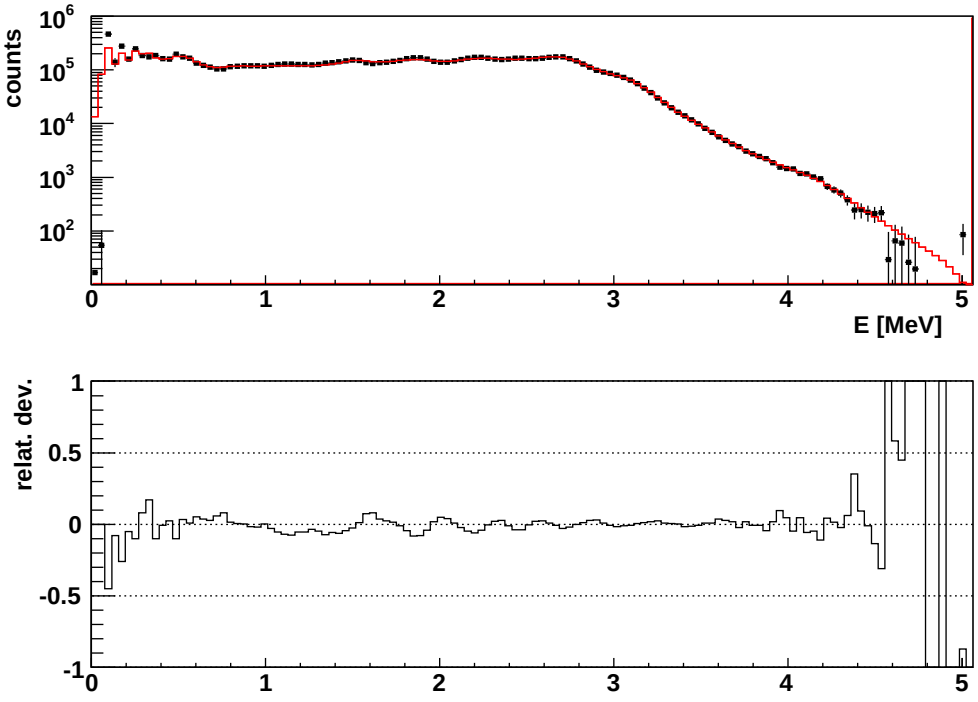

Figure 4.33: Upper panel: the comparison between the reconstructed (red continuous line) and experimental (black dots) spectra is shown for ^{105}Mo decay. The different contaminants have been subtracted. The lower panel shows the relative deviation between the spectra.

4.8.2 Result I: feeding distribution

The feeding distribution deduced is shown in the lower panel of figure (4.34). The effect of feeding shifted from low to high excitation energies compared with high resolution measurements is also noticeable for this decay. About 72.7 % of the feeding is concentrated in the first 523 keV in high resolution, whilst, most of the feeding in the TAGS feeding distribution is placed above 1.5 MeV.

If we have a look at the upper panel of the same figure we see that in the first 500 keV experimental data (black dots) and the sum of the contaminants (green dots) partially overlap.

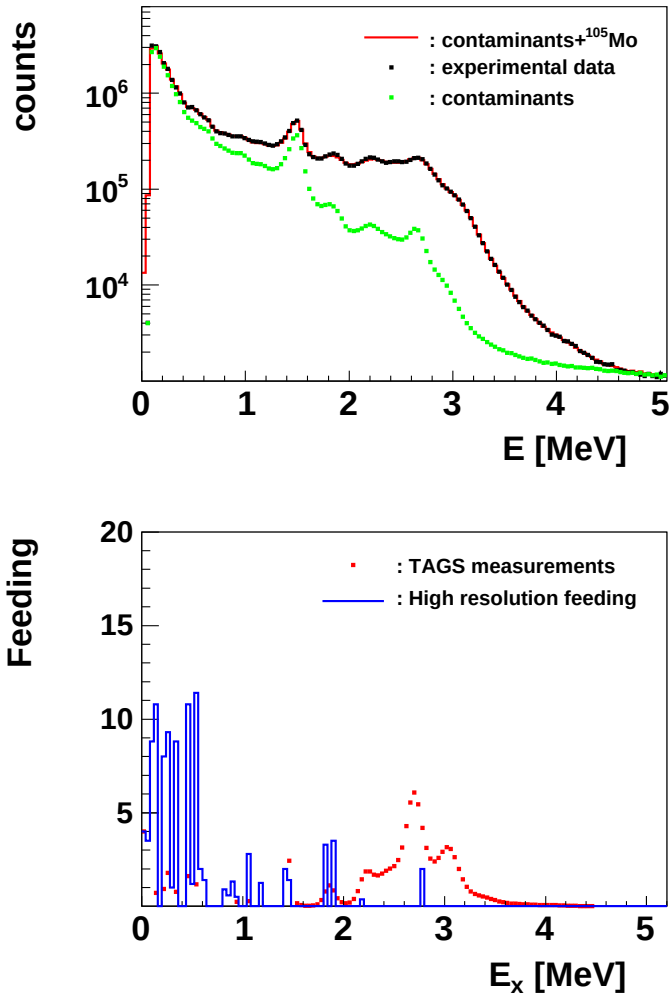

Figure 4.34: Upper panel: the comparison of reconstructed and experimental data including the contaminants is shown for ^{105}Mo decay. The contribution of all the contaminants is also shown in the upper panel. In the lower panel, the β-feeding distribution obtained from the experiment is compared with the one from high resolution measurements.

4.8.3 Result II: strength distribution

In figure (4.35) the TAGS strength distribution is compared with the high resolution strength distribution and the one predicted by Gross theory. Figure (4.36) shows the accumulated strength. Up to 3 MeV the three distributions differ and the TAGS distribution runs below the Gross theory and the high resolution distributions. From this energy up to the Q-value, the TAGS and Gross Theory distributions are similar and both differ from the high resolution distribution. In the energy range available to the decay, the accumulated TAGS strength is approximately equal to the Gross Theory prediction and a factor of 22 higher than the high resolution result.

The errors of the TAGS strength distribution are in general small except in the last MeV where they oscillate considerably. This effect was also seen when ^{107}Tc decay was studied.

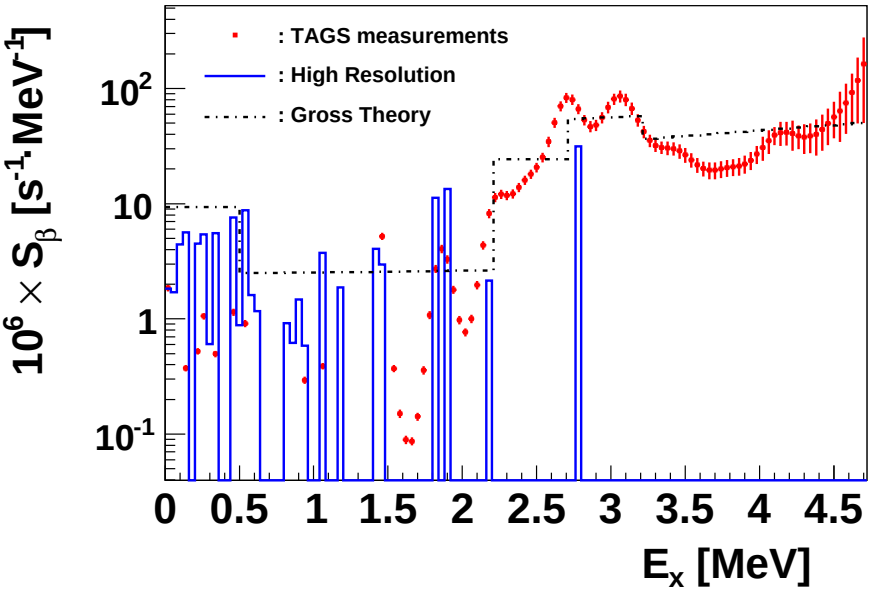

Figure 4.35: β-strength distribution for the decay of ^{105}Mo. The β-strength distribution obtained with the TAGS detector is compared with the one deduced from high resolution measurements and with that obtained from Gross theory.

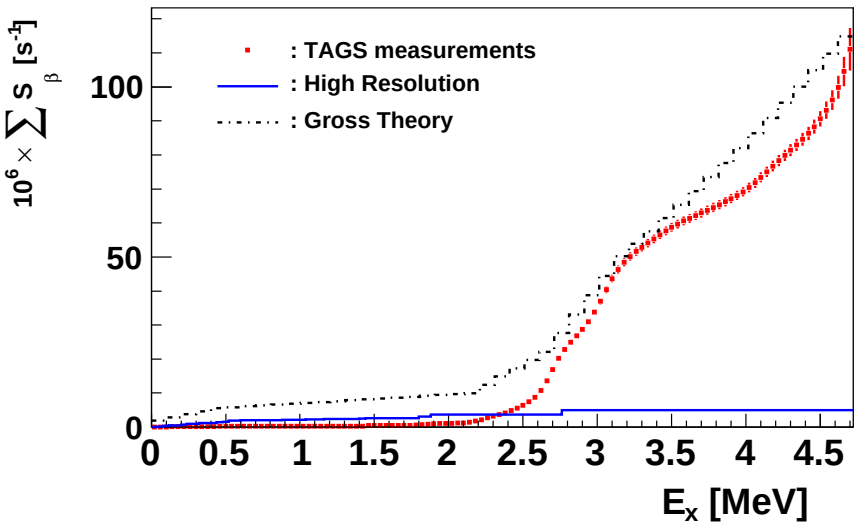

Figure 4.36: Accumulated strength distributions for the decay of ^{105}Mo.

4.8.4 Result III: average energies

The average energies obtained with this analysis are:

$$\overline{E}_\beta = 1048.65 \pm 0.05 \pm 44.00 \text{ keV}$$

$$\overline{E}_\gamma = 2406.52 \pm 0.13 \pm 93.00 \text{ keV}$$

These results correspond to the assumptions of known level scheme up to 1476.37 keV, statistical model applied from 1520 keV on and feeding to the ground state of ^{105}Tc fixed to 4%. Similar analysis leaving free the feeding to the ground state of the daughter nucleus gives $\overline{E}_\beta = 1004$ keV and $\overline{E}_\gamma = 2500$ keV. This second analysis has the closest χ^2 value. Similarly to earlier cases, the systematic errors were obtained from the different analysis. If we do not include the daughter activity contamination (^{105}Tc decay) the analysis gives $\overline{E}_\beta = 1076.24$ keV and $\overline{E}_\gamma = 2347.38$ keV. The ^{105}Tc decay contamination amounts to 13.76% as was mentioned earlier (section 3.3.4).

The values differ from the average energies given in the JEFF-3.1 database,

$$\overline{E}_{\beta} = 1922.02 \pm 122.48 \text{ keV}$$

$$\overline{E}_{\gamma} = 551.49 \pm 24.21 \text{ keV}$$

by 873.37 keV for the average beta energy and by 1855.03 keV for the average gamma energy. The TAGS average beta energy decreases, meanwhile the TAGS average gamma energy increases dramatically. This is the expected effect when high resolution data suffer from the Pandemonium effect.

4.9 Effect of the average energies on the summation calculations

In the next table we summarize the average energies obtained for the experiment as well as the average energies from JEFF-3.1[61] and ENDF/B-VII[68] databases. The values from both databases are exactly the same except for some nuclei where the values differ in several keV.

Isotope	energy type	TAGS experiment [keV]	JEFF-3.1 [keV]	ENDF/B-VII [keV]	difference [keV]
^{102}Tc	beta	1935(11)	1945(16)	1945(16)	-10
	gamma	106(23)	81(10)	81(5)	25
^{104}Tc	beta	931(10)	1595(75)	1595(75)	-664
	gamma	3229(24)	1890(31)	1890(31)	1339
^{105}Tc	beta	764(81)	1310(173)	1310(205)	-546
	gamma	1825(174)	668(19)	665(19)	1157
^{106}Tc	beta	1457(30)	1943(69)	1906(67)	-486/-449
	gamma	3132(70)	2191(51)	2191(51)	941
^{107}Tc	beta	1263(212)	2056(254)	2054(254)	-793/-791
	gamma	1822(450)	515(11)	515(11)	1307
^{101}Nb	beta	1797(133)	1863(307)	1966(307)	-67/-169
	gamma	445(279)	245(22)	270(22)	200/175
^{105}Mo	beta	1049(44)	1922(122)	1922(122)	-873
	gamma	2407(93)	551(24)	552(24)	1855/1854

Table 4.17: Results of average β- and γ-ray energies. Comparison with the databases.

Looking at this table, the fact that for all the nuclei the γ-ray average energy has increased and the β-ray average energy has decreased in comparison with the databases is more evident. This tendency is better seen if we include our average energies in the databases and plot the calculated decay heat components in the usual way. The average energies obtained for the isotopes analyzed were added by Alejandro Sonzogni to the ENDF/B-VII database and the γ- and β-ray decay heat components were calculated for an instantaneous fission event in ^{239}Pu[69]. The results are shown in the next two figures. For both pictures, the colour convention is the following: black dots correspond to experimental measurements (Tobias compilation[70], the standard compilation used in this field) and the blue and red lines represents the theoretical calculations using ENDF/B-VII without and with, respectively, our average energies.

The first figure, (4.37), corresponds to the γ-ray decay heat component. This figure is analogous to the one shown in chapter 1. The effect obtained when our data are included in the nuclear database is to pull up the blue line close to the experimental points. On the other hand, this decay heat component is inside the error bars in almost the whole range, which is an improvement in comparison with the theoretical calculations based only on high resolution measurements. In particular, for the range from 300 to 3000 seconds, the increment in the summation calculations solves about two thirds of the known γ-ray discrepancy. The important fact is that this improvement has been achieved only with the average energies of seven nuclei, possibly affected by the Pandemonium effect.

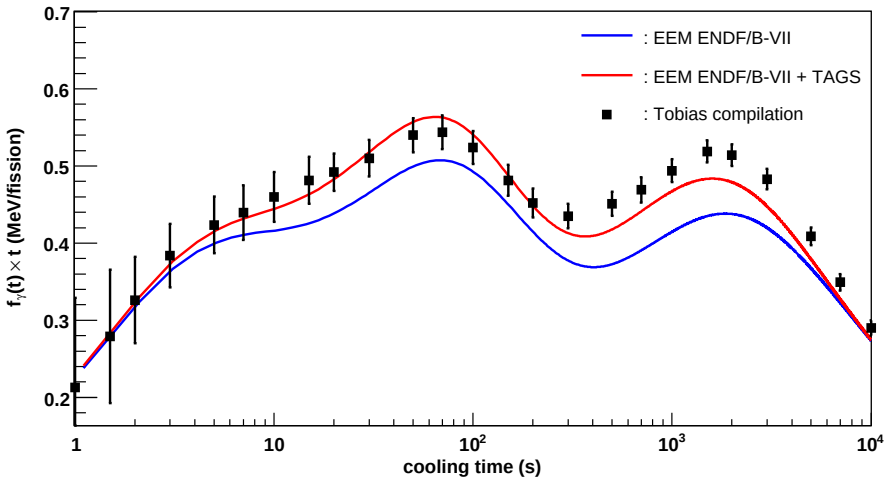

Figure 4.37: Comparison of calculated γ-ray decay heat component with the experimental data compilation of Tobias[70] after an instantaneous fission event in ^{239}Pu.

Now, if we have a look at what happens with the β-ray decay heat component, figure (4.38), we see that the summation calculations do not shows a significant change. The effect of the average energies of the isotopes of interest when included in the database is to pull down the blue line, but it remains inside the experimental error bars.

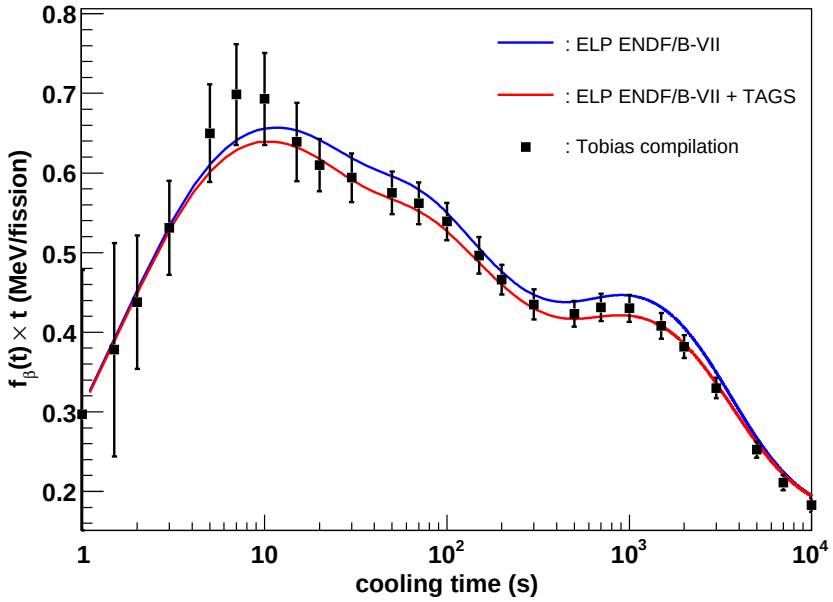

Figure 4.38: Comparison of calculated β-ray decay heat component with the experimental data compilation of Tobias[70] after an instantaneous fission event in ^{239}Pu.

The impact on summation calculations for ^{235}U was also calculated[69]. The γ- and β-ray decay heat components were also calculated for an instantaneous fission event in ^{235}U. The effect of the inclusion of the TAGS data in the nuclear database is similar to the case of ^{239}Pu but less impressive. This is related to the cumulative fission yields. For ^{239}Pu, the cumulative fission yields for the isotopes studied here is approximately 33.8% of the fission, while for ^{235}U it is 13.5%.

5

Summary and conclusions

5.1 Introduction

A correct assessment of decay heat is very important for any nuclear facility and has security, economic and legislative implications. For that reason the data needed for the computations must be accurate enough to determine as precisely as possible the decay heat. In order to improve the prediction power of the decay heat summation calculations, we have measured the decay of some specific nuclei whose decays were assumed to suffer from the Pandemonium effect and were identified as possible important contributors to the reactor decay heat.

For the measurements the total absorption γ-ray technique (TAGS) was used. In contrast to the high resolution technique, this technique is based on the detection of the gamma cascades that follow the beta decay instead of detecting the individual γ-rays. The TAGS technique is able to avoid the Pandemonium effect since a total absorption spectrometer is in essence a calorimeter placed around the source achieving an almost 100% efficiency for detecting gamma cascades. The problem with this technique is the isobaric contamination. We have seen that a total absorption spectrometer is a high efficiency summing device but it has bad resolution compared with a high resolution setup. Then, in order to use this technique, we need very pure beams. Due to the refractory character of the isotopes studied, the experiment was performed at the IGISOL facility in Jyväskylä. In this facility, a Penning trap system is available, that can be used as a high resolution mass separator. This was the first time that a total absorption spectrometer and a Penning trap was used together. The results were very satisfactory. In general, the isotopes were well separated. Only for one case (^{102}Tc), the isotope of interest could not be cleanly separated from its parent nucleus. This was related to the

production mechanism choosen for ^{102}Tc.

5.2 Conclusions

The conclusions that can be drawn from our results are:

- Feeding and strength distributions

We have demonstrated that making use of the total absorption γ-ray spectroscopy we are able to detect feeding and then strength, at excitation energies higher than the last high resolution known level for all the nuclei studied. This confirms that the high resolution data for most of the isotopes studied suffer from the Pandemonium effect[12] as it was assumed.

- Average energies

Regarding the average energies obtained for the isotopes studied, we see that the average γ-ray energies increase and the average β-ray energies decrease for most of the nuclei in comparison with the average energies available at the JEFF-3.1 database, figures (5.1) and (5.2). This fact means that the average gamma energy is underestimated and the average beta energy is overestimated in the database for almost all the isotopes, which is also a sign of high resolution data suffering from the pandemonim effect. The energy difference between TAGS and JEFF-3.1 databases average energies (figure (5.3)) is quite significant for almost all the nuclei (with the exception of the ^{102}Tc and ^{101}Nb decays).

- Summation calculations

The impact of the inclusion of the new average energies in the databases was also studied for two fuels, ^{239}Pu and ^{235}U. For the ^{239}Pu, the obtained TAGS data improves the overall prediction power of the summation calculations: the new average γ-ray energy data increase the γ-ray decay heat component solving two thirds of the γ-ray discrepancy in the 300-3000 s interval, and solves also a discrepancy in the 2-20 s range. On the other hand, the calculated β-ray decay heat component using the new average β-ray energy data is still inside the experimental error bars. For the ^{235}U, the effect of the inclusion of the TAGS data in the nuclear database is less impressive.

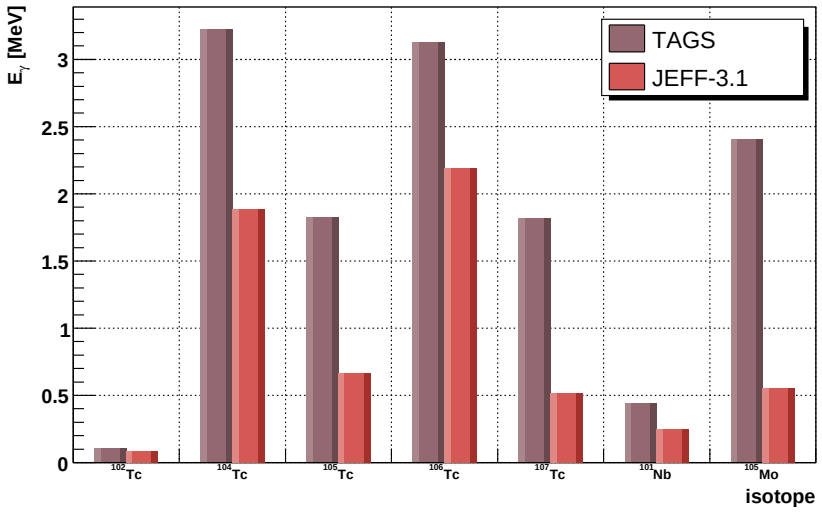

Figure 5.1: Average gamma energies obtained with the TAGS technique for the isotopes studied. The JEFF-3.1 database average energies are also presented for comparison.

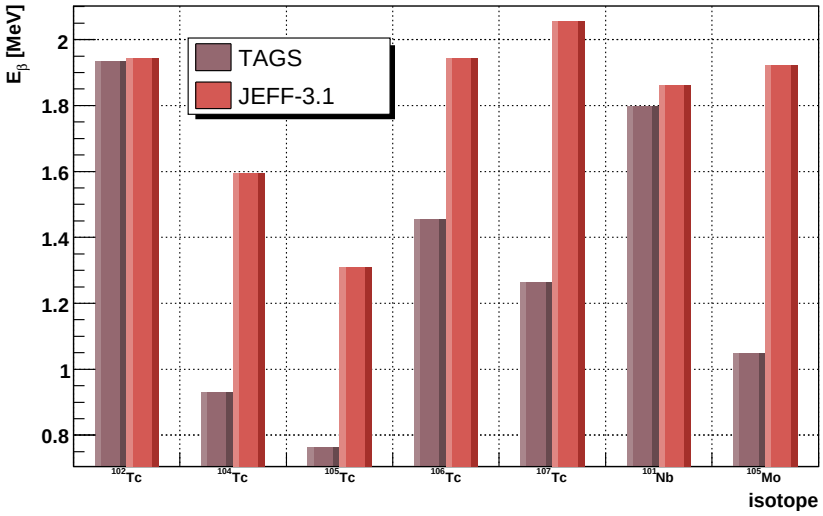

Figure 5.2: Average beta energies obtained with the TAGS technique for the isotopes studied. The JEFF-3.1 database average energies are also presented for comparison.

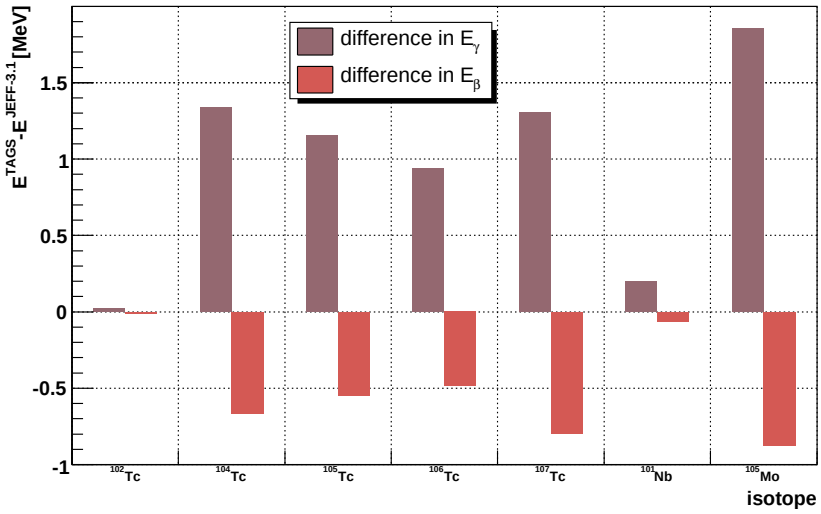

Figure 5.3: Average γ- and β-ray energy differences between TAGS and the JEFF-3.1 database for the relevant nuclei.

5.3 Future plans

With this work we have demonstrated that the use of the total absorption γ-ray spectroscopy applied to β-decay studies of nuclei produced in the fission process is very important to improve the precision of the decay heat summation calculations. This fact has encouraged us to extend this study to other isotopes of interest for the decay heat problem so there is still a lot of work to do. Presently, we have a running research program based on these studies. For example, we have measured at the IGISOL facility some isotopes from that list in November of 2009 with a experimental setup very similar to the one used for our measurements.

Regarding the description of strength distributions, we are presently in contact with theoreticians. It is foreseen that from this study new insigths of the nuclear structure of this interesting region can be obtained. The interest in this region is associated to shape effects predicted by [38] in the A$\sim$100 region.

On the other hand, although this work was performed basically as an application to the decay heat, it has also consequences for other applications such as the prediction of the reactor antineutrino spectrum. Antineutrinos are emitted as part of the β^--decay

process of fission products generated in the core of nuclear reactors. Due to the nature of the antineutrinos, they flight long distances without their flux being attenuated and thus they could be used to monitorize reactor operations non-invasively. Their spectrum is directly related to the β-particle spectrum so an improvement of the β^--decay data may reduce the uncertainties in the global shape of the antineutrino spectrum. Related to it, we have started a new research program aimed to study the beta-decay properties of isotopes of interest for neutrino physics using the total absorption technique.

6 Resumen en castellano

6.1 Introducción al problema

En un reactor nuclear, un flujo controlado de neutrones induce la fisión produciendo núcleos de menor masa, conocidos como productos de fisión, y nuevos neutrones. Aproximadamente el 8% del total de la energía generada durante el proceso de fisión está relacionado con las energías γ y β emitidas durante la desintegración natural de los productos de fisión. Cuando un reactor nuclear es apagado, esta fuente de energía permanece y proporciona la mayor parte del calor residual producido. Por tanto, tras terminar el proceso de fisión es necesario mantener la refrigeración del reactor y la forma y la cantidad de ese requisito esencial debe ser especificado en base a lo que se conoce como cálculos del calor residual. Dicho calor residual varía en función del tiempo de enfriamiento y puede ser determinado en teoría a partir de datos nucleares, mediante cálculos basados en la cantidad de núcleos creados durante el proceso de fisión y en sus propiedades de desintegración radioactiva:

$$f(t) = \sum_{i}^{all\ FPs} (E_{\beta}^{i} + E_{\gamma}^{i})\lambda_{i}^{T} N_{i}(t) \tag{6.1}$$

donde E^i es la energía de desintegración del núcleo i (componentes β y γ), λ_i es la constante de desintegración del núcleo i y $N_i(t)$ es el número de núcleos i en el tiempo de enfriamiento t.

Este método requiere por tanto un conocimiento preciso de secciones eficaces, vidas medias, tasas de fisión, las energías medias γ y β emitidas en la desintegración, etc. Toda esta información es extraida de bases de datos nucleares. En particular es importante mencionar qu las energías medias γ y β se basan en su gran mayoría en medidas

de alta resolución (Ge). Sin embargo, se han observado discrepancias entre las medidas experimentales y los cálculos teóricos de la componente γ del calor residual para varios núcleos como ^{239}Pu, ^{233}U, ^{235}U y ^{238}U. Muchos estudios realizados se han centrado en la búsqueda de la fuente de dicha discrepancia, concluyendo que la principal causa de entre todas las posibles evaluadas (tasas de fisión, secciones eficaces neutrónicas y datos de desintegración β), era la que hacía referencia a los datos de desintegración de los productos de fisión de vidas medias cortas.

Gran parte de los datos de desintegración existentes en las bases de datos nucleares sufren de lo que se conoce como efecto Pandemonio. Este efecto está relacionado con la dificultad experimental para construir un esquema de niveles basado en datos de espectroscopía de alta resolción, debido a la baja eficiencia de los detectores de germanio. A causa de este problema, la probabilidad de transición a niveles a alta energía de excitación en el núcleo hijo es asignada erróneamente a niveles a baja excitación. Este efecto tiene consecuencias directas en los cálculos del calor residual puesto que se subestima la energía media γ y se sobreestima la energía media β emitidas en la desintegración.

Es ya reconocido que la única manera de evitar el efecto Pandemonio es haciendo uso de la técnica de absorción total. El fundamento básico de este tipo de espectroscopía es la detección de todos los rayos γ producidos en la de-excitación de un nivel tras la desintegración β, en vez de detectar cada rayo γ individual como ocurre en la espectroscopía de alta resolución. De modo que en el espectro de energías observaremos un pico suma centrado en la energía correspondiente al nivel que se de-excita. Los espectrómetros que usan esta técnica, comúnmente llamados TAGS (*Total Absorption γ-ray Spectrometer*), están construidos con grandes cristales centelleadores que cubren un ángulo sólido 4π alrededor de la fuente radiactiva obteniendo así altas eficiencias intrínsecas para la detección de rayos γ. Un TAGS ideal tiene un 100 % de eficiencia de pico para rayos γ de todas las energías y su respuesta es independiente de la ruta que siga la cascada de rayos γ. Esto quiere decir que la información de cómo se pueblan los niveles en la desintegración β se puede extraer directamente del espectro medido. Sin embargo, los espectrómetros usados no son ideales, por lo que su eficiencia se va a ver reducida debido a que el detector no es lo suficientemente grueso e incluye material muerto y otro tipo de detectores. Todo esto hace que éste no cubra completamente un ángulo sólido 4π y se reduzca su eficiencia lo cual implica que tendremos diferentes respuestas del detector para diferentes rutas de la cascada de rayos γ. La solución a este problema es el uso de un método de deconvolución de espectros que asigne a cada energía el canal correcto.

Esta técnica fue aplicada con éxito en los años 90 por Greenwood *et al.* para un total de 45 isótopos ricos en neutrones, para los cuales se midió la intensidad β en función de la energía de excitación. Las energías medias se calcularon a partir de la intesidad β haciendo uso de las siguientes relaciones:

$$\overline{E}_\beta = \sum_i I_i \frac{f_\beta(E_i - Q_\beta)}{f(E_i - Q_\beta)} \tag{6.2}$$

$$\overline{E}_\gamma = \sum_i I_i E_i \tag{6.3}$$

donde I_i es la distribución de intesidad normalizada a la unidad, $f_\beta(E_i - Q_\beta)$ representa el promedio del espectro continuo β emitido que depende del tipo de proceso β así como de la energía disponible para la desintegración y $f(E_i - Q_\beta)$ es el factor de normalización.

Tras los buenos resultados de esta técnica, se creó un grupo de trabajo de la IAEA (WPEC SG-25) que propuso una lista de radionúclidos para futuras medidas con espectrómetros de absorción total con el fin de mejorar la predicción de los cálulos del calor residual. Los isótopos que se recogen en dicha lista han sido identificados como grandes contribuidores al calor residual y sus datos de alta resolución tienen una alta probabilidad de estar sufriendo del efecto Pandemonio.

De dicha lista, se seleccionaron 7 isótopos: ^{101}Nb, ^{102}Tc, ^{104}Tc, ^{105}Tc, ^{105}Mo, ^{106}Tc y ^{107}Tc. Por dos razones. La primera y principal tiene que ver con la contribución de estos isótopos al calor residual. Haciendo uso de la espectroscopía de absorción total se espera obterner datos libre del efecto Pandemonio y ver el impacto que estos isótopos tienen en los cálculos teóricos del calor residual. Y por otro lado, estos núcleos son de interés puesto que se encuentran en una región de coexistencia de forma confirmada. Para entender la estructura nuclear de estos isótopos recurriremos a la distribución de la llamada función de fuerza β o S_β, puesto que esta cantidad es sensible a las pequeñas componentes de las funciones de onda así como a la forma global del núcleo. S_β se define como el promedio de la intensidad B(GT) a todos los niveles dentro de un intervalo de energía ΔE_x con energía de excitación central E_x. Esta distribución está relacionada con la intensidad de la transición β a un nivel de energía de excitación E_i mediante la ecuación

$$S_i = \frac{I_i}{f(Q_\beta - E_i)T_{1/2}} \tag{6.4}$$

donde $f(Q_\beta - E_i)$ es la función de Fermi, ya mencionada anteriormente, $T_{1/2}$ es la vida media.

6.2 El experimento

Debido al carácter refractorio de los isótopos estudiados, el experimento se realizó en las instalaciones de IGISOL de la Universidad de Jyväskylä (Finlandia). Un haz de

protones de 50 MeV se hizo incidir sobre un blanco de uranio natural. Los productos de fisión fueron parados, ionizados y acelerados con campos eléctricos y posteriormente separados en masa con un campo magnético. Una vez seleccionada la masa q se pretendía medir, se realizó la purificación isobárica de los haces mediante el uso de una trampa de iones tipo Penning. Esta es la primera vez que se ha utilizado conjuntamente un espectrómetro de absorción total con una trampa de Penning.

Los haces radiactivos finales eran implantados en una cinta y transportados al interior del espectrómetro de absorción total. Este consiste en dos cristales cilíndricos de NaI(Tl) de 200 mm de diámetro y una longitud de 200 y 100 mm, respectivamente. El cristal más grande tiene además un agujero longitudinal de 43 mm de diámetro. Este espectrómetro de absorción total ha sido utilizado en otros experimentos y tiene una buena eficiencia de detección. La pureza de la fuente era supervisada en todo momento en el punto de implantación con un detector de germanio.

De este modo se realizaron una serie de medidas de los isótopos de interés así como del fondo ambiental presente durante el experimento. El fondo se midió durante una hora cada dos horas de medida de datos durante todo el experimento.

6.2.1 Análisis de los datos

El punto más delicado de este trabajo es el complejo análisis de los datos. Los datos medidos están relacionados con como se pueblan cada uno de los niveles a través de la respuesta del espectrómetro. Esto quiere decir que para obtener la intensidad β, es necesario resolver el siguiente problema lineal, también conocido como problema inverso

$$d_i = \sum_{j=1}^{j_{max}} R_{ij} f_j, \quad i = 1, i_{max} \quad o \quad \mathbf{d} = \mathbf{R} \cdot \mathbf{f} \tag{6.5}$$

donde la construcción de la matriz de respuesta no es nada trivial puesto que requiere un conocimiento previo del esquema de de-excitación del núcleo. Hay que tener en cuenta que para núcleos lejos de la estabilidad como es nuestro caso, el número de niveles posibles puede ser del orden de $10^4 - 10^5$ dentro de la ventana de energías accesible en la desintegración y que el esquema de de-excitación de los núcleos solo se conoce en parte, por lo que se hace necesario el uso del modelo estadístico para completar la información. A parte, este problema tiene infinitas soluciones que son compatibles con los datos experimentales, con lo cual se hace necesario resolver el problema inverso directamente. Por lo tanto, para resolverlo hemos hecho uso de un método de deconvolución de espectros descrito en la referencia [29].

6.3 Resultados obtenidos

Para todos los isótopos analizados, se ha comparado la intensidad β obtenida con la intensidad β de alta reslución. Generalmente, la intensidad β de alta resolución está concentrada a bajas energías de excitación, que es lo que se espera si las medidas de alta resolución sufren del efecto Pandemonio. Esto no es así para la intensidad β obtenida con el método de espectroscopía de absorción total. De hecho, en todos los casos, se ha detectado intensidad β a alta energía de excitación, por encima del último nivel conocido del esquema de de-excitación de alta resolución de los isótopos. Esto se puede entender como un desplazamiento de parte de la intensidad β de alta resolución a altas energías de excitación. A partir de la intensidad β se ha calculado las energías medias β y γ mediante las ecuaciones (6.2) y (6.3), y la distribución de la función de intensidad β, ecuación (6.4), de cada uno de los isótopos estudiados.

6.3.1 Energías medias

En las gráficas (6.1) y (6.2) se comparan las energías medias γ y β obtenidas con las energías medias usadas en la base de datos JEFF-3.1 para todos los isótopos estudiados. Como se puede ver en la gráfica (6.1), las energías medias γ obtenidas con el TAGS para todos los isótopos estudiados son mayores que las energías medias γ de la base de datos JEFF-3.1. Las differencias entre los distintos valores son bastante considerables para casi todos ellos, con la excepción del ^{102}Tc. Para este isótopo, la diferencia es de tan solo 25 keV, bastante pequeña si comparamos esta cantidad con la gran diferencia de energías entre datos experimentales y base de datos para los otros isótopos. En el caso del ^{101}Nb, la diferencia de energías no llega a ser tan notable como en los otros isótopos (^{104}Tc, ^{105}Tc, ^{106}Tc, ^{107}Tc y ^{105}Mo) puesto que ambas energías difieren solo en 200 keV. En cuanto a las energías medias β, gráfica (6.2), vemos que los valores obtenidos con el espectrómetro de absoción total son menores que las dadas en JEFF-3.1. De nuevo, la diferencia es mínima para el ^{102}Tc (que en este caso es de solo 10 keV), en comparación con las grandes diferencias de los otros isótopos, a excepción del ^{101}Nb, en la que datos experimentales y base de datos difieren solo en 67 keV.

Por completitud, en la gráfica (6.3), se muestran las diferencias entre datos experimentales y la base de datos JEFF-3.1 para ambas energías medias. Las diferencias son positivas para las energías medias γ y negativas para las energías medias β y así se muestran en la gráfica. Por otro lado, la tabla (6.1) es una tabla resumen de las energías medias con sus errores del experimento y de dos bases de datos, JEFF-3.1 y ENDF/B-II. Las diferencias entre los datos experimentales y las bases de datos se dan en la sexta columna. Como se puede apreciar, las energías medias de JEFF-3.1 y ENDF/B-II son prácticamente iguales, diferiendo solo en algunos casos y por cantidades muy pequeñas.

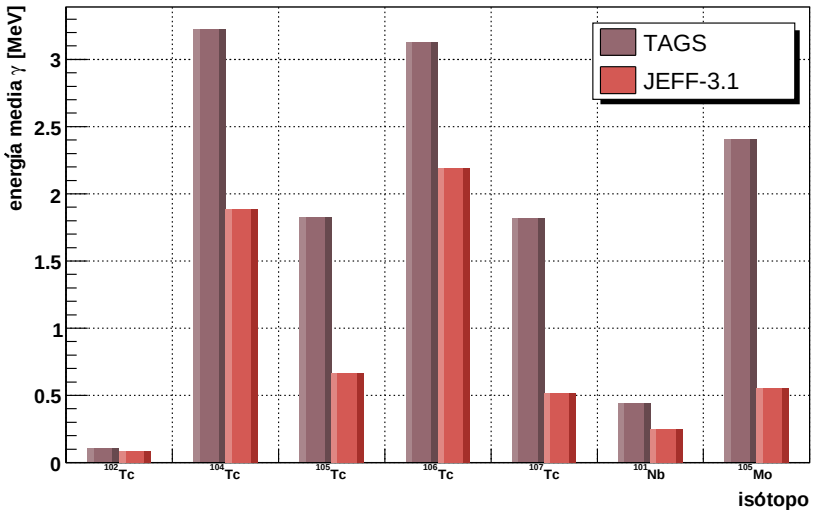

Figure 6.1: Energías medias γ obtenidas con la técnica TAGS de los isótopos analizados. Comparación con las energías medias de la base de datos JEFF-3.1.

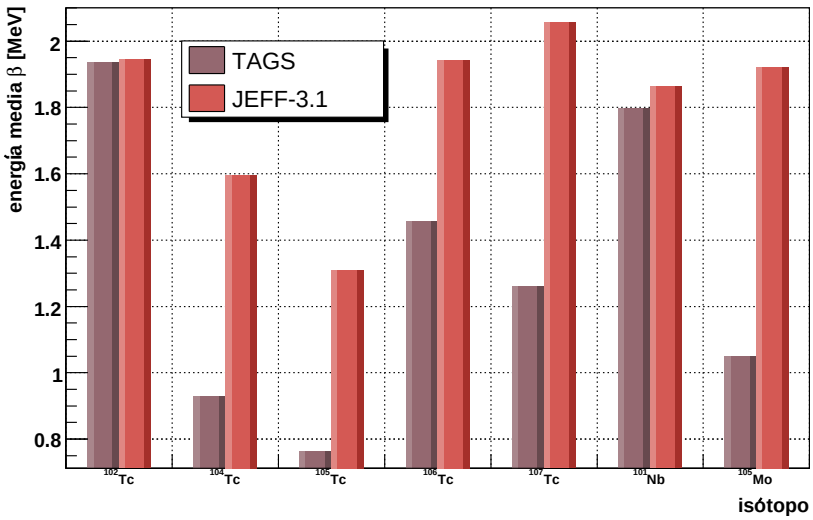

Figure 6.2: Energías medias β obtenidas con la técnica TAGS de los isótopos analizados. Comparación con las energías medias de la base de datos JEFF-3.1.

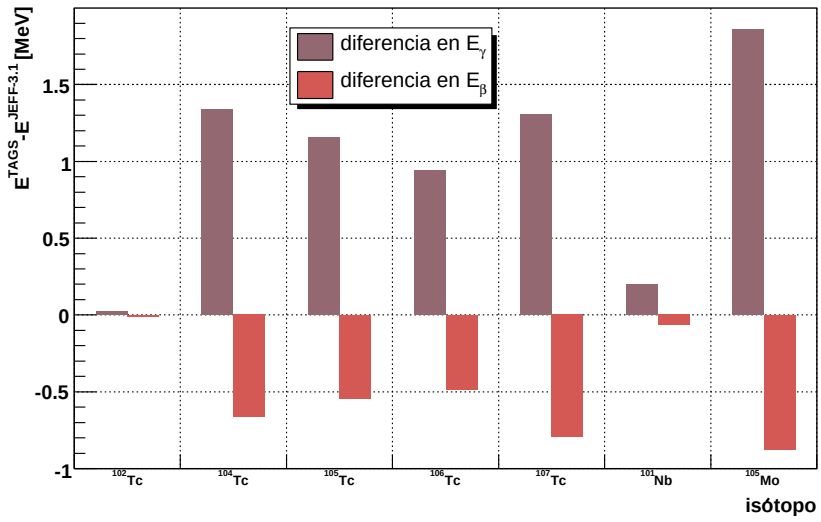

Figure 6.3: Diferencias de energías medias γ y β entre datos experimentales y la base de datos JEFF-3.1.

Isótopo	tipo de energía	experimento TAGS [keV]	JEFF-3.1 [keV]	ENDF/B-VII [keV]	diferencia de energías [keV]
^{102}Tc	beta	1935(11)	1945(16)	1945(16)	-10
	gamma	106(23)	81(10)	81(5)	25
^{104}Tc	beta	931(10)	1595(75)	1595(75)	-664
	gamma	3229(24)	1890(31)	1890(31)	1339
^{105}Tc	beta	764(81)	1310(173)	1310(205)	-546
	gamma	1825(174)	668(19)	665(19)	1157
^{106}Tc	beta	1457(30)	1943(69)	1906(67)	-486/-449
	gamma	3132(70)	2191(51)	2191(51)	941
^{107}Tc	beta	1263(212)	2056(254)	2054(254)	-793/-791
	gamma	1822(450)	515(11)	515(11)	1307
^{101}Nb	beta	1797(133)	1863(307)	1966(307)	-67/-169
	gamma	445(279)	245(22)	270(22)	200/175
^{105}Mo	beta	1049(44)	1922(122)	1922(122)	-873
	gamma	2407(93)	551(24)	552(24)	1855/1854

Table 6.1: Energías medias β y γ obtenidas de los datos de TAGS comparadas con los valores de las bases de datos JEFF-3.1 y ENDF/B-VII.

Para ver el impacto de las energías medias obtenidas, estas han sido incluidas en la base de datos ENDF/B-VII y se han calculado las componentes γ y β del calor residual después de un suceso de fisión instantáneo en el ^{239}Pu[69]. Los resultados obtenidos han sido comparados con las medidas experimentales de la compilación de Tobias (que es la estándar en este campo) y con las componentes γ y β del calor residual usando ENDF/B-VII sin nuestros datos. En la gráfica (6.4) se muestran los resultados para la componente γ del calor residual. Vemos que al incluir las energías medias γ de los isótopos analizados en la base de datos (línea roja) la curva se acerca a los datos experimentales (puntos negros) solucionando aproximadamente unas dos terceras partes de la discrepancia en el rango de tiempos de enfriamiento de 300 a 3000 segundos. Fuera de ese rango de tiempos, la curva está dentro de los errores experimentales. Por otro lado, los resultados para la componente β, gráfica (6.5), muestran que los cálculos incluyendo TAGS no introducen un cambio significativo estando siempre dentro de las barras de error de los datos experimentales. La inclusión de los datos de espectroscopía de absorción total en las bases de datos no producen un efecto tan pronunciado en otros núcleos como en el caso del ^{239}Pu. En el caso del ^{235}U, se calcularon también las componentes γ y β del calor residual después de un suceso de fisión instantáneo en este núcleo obteniendo resultados parecidos a los del ^{239}Pu pero menos cuantitativos. Esto es debido a las tasas de fisión acumuladas, que para el ^{235}U son menores que para el ^{239}Pu.

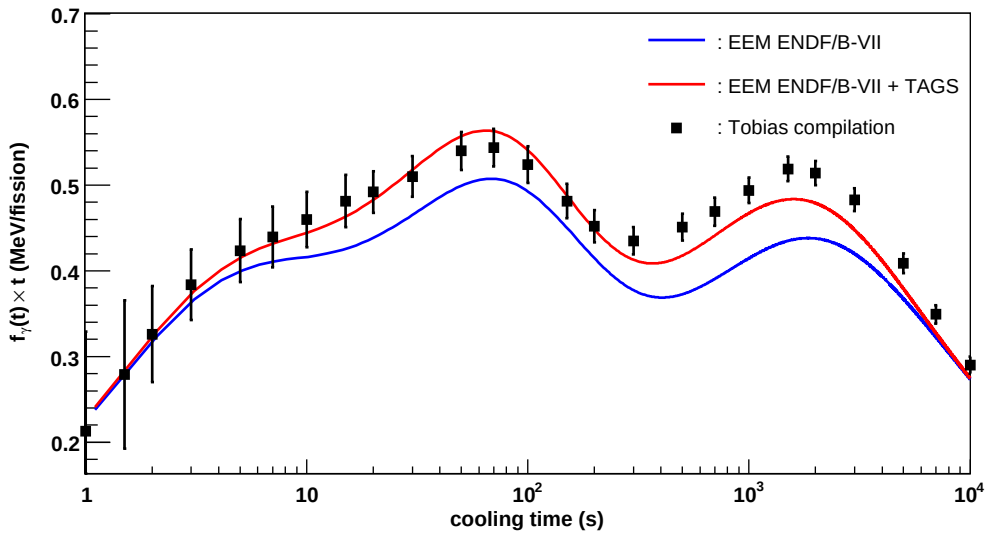

Figure 6.4: Componente γ del calor residual después de un suceso de fisión instantáneo en el ^{239}Pu.

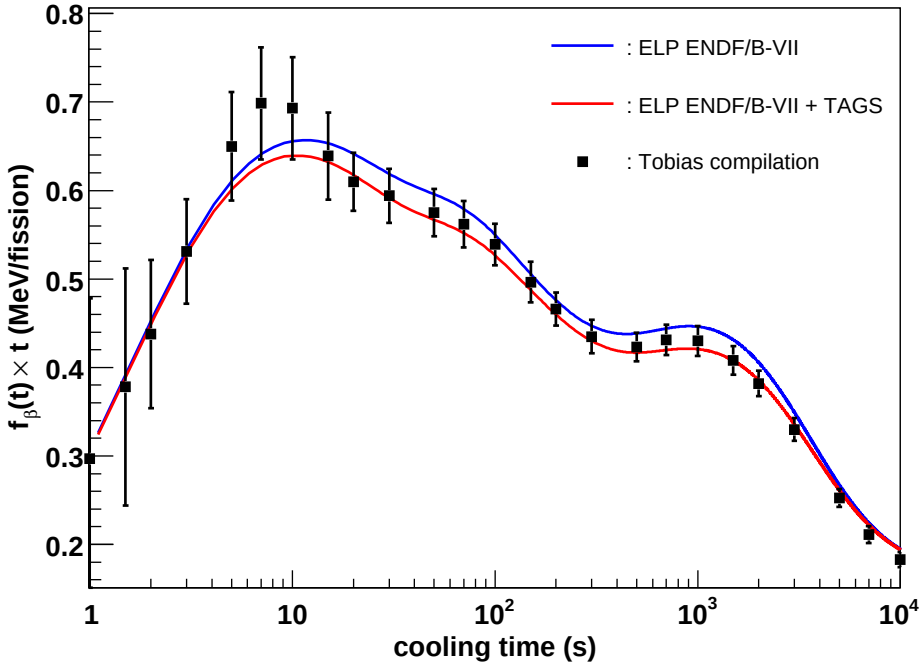

Figure 6.5: Componente β del calor residual después de un suceso de fisión instantáneo en el ^{239}Pu.

6.4 Conclusiones y visión de futuro

En este trabajo hemos realizado un estudio de las propiedades de la desintegración β de núcleos ricos en neutrones que son de interés en el cálculo del calor residual en reactores nucleares mediante el uso de la espectroscopía de absorción total. Con el espectrómetro de absorción total hemos detectado intensidad β, y por tanto también S_β, por encima del último nivel conocido de alta resolución para prácticamente todos los isótopos estudiados. Esto demuestra que los datos de alta resolución para la gran mayoría de estos isótopos sufren de efecto Pandemonio. Este efecto también se pone de manifiesto en las energías medias obtenidas a partir de la intensidad β puesto que al ser comparados los valores obtenidos con dos bases de datos diferentes, JEFF-3.1 y ENDF/B-VII, se observa un aumento de las energías medias γ y una disminución de las energías medias β. La inclusión de las energías medias obtenidas con esta técnica

en la base de datos ENDF/B-VII nos ha permitido mejorar la precisión de los cálculos del calor residual para el ^{239}Pu como ha quedado demostrado en las gráficas (6.4) y (6.5).

Vistos los buenos resultados obtenidos con esta técnica, hemos decidido extender este estudio a otros isótopos de interés para el problema del calor residual. De hecho, algunos de ellos ya han sido medidos en el pasado mes de noviembre de 2009 y los datos están siendo analizados en estos momentos.

El estudio de estos isótopos también es relevante para estudios de estructura nuclear, puesto que estos isótopos se encuentran en la región A$\sim$100, donde se han asociado efectos de forma predichos por [38]. Referente a esto, ya nos hemos puesto en contacto con teóricos pero aún queda mucho trabajo por hacer.

Por otra parte, aunque este trabajo ha sido realizado principalmente como una aplicación del calor residual, tiene también consecuencias en otras aplicaciones como la predicción del espectro de antineurinos emitidos en los reactores nucleares. En el proceso de desintegración β^- de los productos de fisión que tiene lugar en el interior de un reactor se producen también antineutrinos. Estos interaccionan débilmente con la materia y por tanto vuelan grandes distancias sin verse su flujo atenuado. Es por esto por lo que se pueden usar para supervisar los sistemas de operación de los reactores de manera no invasiva. Este espectro está relacionado con el espectro de emisión de las partículas β emitidas en el proceso de desintegración β^- y, por tanto, una mejora de los datos de desintegración β^- implica la reducción de las incertidumbres en la forma del espectro de antineutrinos. Relacionado con esto, hemos iniciado un programa de medidas de las propiedades de desintegración β de isótopos de interés para la física de neutrinos haciendo uso de la espectroscopía de absorción total.

A

Relevant data of the studied isotopes

Isotope	$T_{1/2}$ [s]	Q_β [keV]	S_n [keV]	parent J^π	daughter J^π	references
^{101}Nb	7.1(3)	4569(18)	5398.24(7)	$(5/2^+)$	$1/2^+$	NDS 2000
^{105}Mo	35.6(16)	4950(50)	7870(70)	$(5/2^-)$	$(3/2^-)$	NDS 2005
^{102}Tc	5.28(15)	4532 (9)	9219.64(5)	1^+	0^+	NDS 1998
^{104}Tc	1098(18)	5516(6)	8901(3)	(3^+)	0^+	NDS 2007
^{105}Tc	456(6)	3746(6)	5910.10(11)	$(3/2^-)$	$3/2^+$	NDS 2005
^{106}Tc	35.6(6)	6547(11)	8466(7)	(1,2)	0^+	NDS 2008
^{107}Tc	21.2(2)	4820(90)	5670(120)	$(3/2^-)$	$(5/2)^+$	NDS 2008

Table A.1: Relevant experimental data of the analyzed isotopes.

Table (A.1) contains the relevant data and the corresponding errors of the β-decay studied processes: half-lives, Q values, neutron separation energies, spin and parity of the ground state of parent and of the daughter nuclei. In all the cases, it was checked if new data was incorporated to the databases or recent versions were available. In this table, some of the spins and parities appear in brackets. This is because there is not enough experimental information about them or the different available information is contradictory.

isotope	Level density parameters		deformation parameter	Strength function parameters								
				E1			M1			E2		
	a	Δ	β	energy [MeV]	width [MeV]	sigma [mb]	energy [MeV]	width [MeV]	sigma [mb]	energy [MeV]	width [MeV]	sigma [mb]
^{101}Nb	11.683	-1.165	0.309	13.469 18.104	3.733 6.566	301.3 171.3	8.817	4.	0.836	13.549	4.898	2.133
^{105}Mo	16.451	-0.769	0.32	13.266 18.013	3.626 6.503	321.0 178.9	8.704	4.	4.045	13.375	4.85	2.172
^{102}Tc	11.973	0.561	0.189	14.391 17.291	4.236 6.015	270.7 190.6	8.788	4.	6.643	13.504	4.886	2.323
^{104}Tc	12.0	0.56	0.253	13.6711 17.722	3.8402 6.304	303.0 184.5	8.731	4.	6.79	13.417	4.861	2.290
^{105}Tc	12.557	-1.013	0.291	13.488 17.813	3.743 6.367	313.1 184.1	8.704	4.	1.114	13.375	4.85	2.274
^{106}Tc	14.353	-0.331	0.281	13.526 17.714	3.762 6.299	313.527 187.274	8.676	4.	5.295	13.332	4.838	2.258
^{107}Tc	16.465	-0.625	0.301	13.346 17.807	3.668 6.362	323.8 186.7	8.650	4.	0.956	13.291	4.826	2.243

Table A.2: Level density and strength function parameters of the nuclei under study.

The data summarized in table (A.2) is data needed for the construction of the unknown part of the level scheme as level density parameters, the deformation parameter and the strength function parameters. The level density parameters, a and Δ, are from the Back-shifted Fermi Gas Formula [55]. These parameters were retrieved from the Reference Input Parameter Library (RIPL-2) webpage[54], for almost the majority of the nuclei. For those nuclei whose level density parameters do not appear in this database the a and Δ parameters were calculated with a program that fits the parameters of the Back-Shifted Fermi Gas Model formula from a set of cumulative number of levels N at different excitation energies U[1]. The deformation parameter, β, was taken from reference [71] and it is needed for the calculation of the strength function parameters. The parameters of the electromagnetic strength functions, *energy*, *width* and *sigma*, are the parameters corresponding to giant resonance, Lorentzian or generalized Lorentzian giant resonances depending on the type of transition.

[1] These cumulative number of levels at different excitation energies are obtained from the HF-BCS Total Level Densities that can be retrieved also from the RIPL webpage.

Bibliography

[1] Juhani Kantele, *Handbook of nuclear spectrometry*, Academic Press Inc., San Diego, 1995.

[2] A. Bohr and B.R. Mottelson, *Nuclear Structure* I (1998) 411.

[3] H. V. Klapdor, Prog. Part. Nucl. Phys., 10 (1983) 131.

[4] A. L. Nichols, FJ/OH Summer School 2000 and references therein.

[5] A. Tobias, Prog. in Nuc. Energy 5 (1980) 1.

[6] F. Schmittroth, Nucl. Sci. Eng. 59 (1976) 117

[7] F. Schmittroth and R. E. Schenter, Nucl. Sci. Eng. 63 (1977) 276.

[8] F. Storrer, Proc. Int. Conf. Nucl. Data for Science and Technology, Vol. 2 (1994) 819.

[9] K. Oyamatsu et al., Proc. Int. Conf. Nucl. Data for Science and Technology, Vol. 59 (1997) 756.

[10] A. Algora et al., Eur. Phy. J. A 20 (2004) 199.

[11] John M. Blatt and Victor F. Weisskopf, *Theoretical nuclear physics*, Dover Publications, Inc. New York, 1991.

[12] J. C. Hardy, L. C. Carraz, B. Jonson and P. G. Hansen, Phys. Lett. 71 B (1977) 307.

[13] T. Yoshida et al., Journal of Nucl. Science and Technology 36 (1999) 135.

[14] M. Akiyama and S. An, Proc. Int. Conf. on Nuclear Data for Sci. and Technol., Antwerp, p. 237 (1982) and references therein.

[15] J. K. Dickens et al., Nucl. Sci. Eng. 74 (1980) 106.

[16] J. K. Dickens et al., Nucl. Sci. Eng. 78 (1981) 126.

[17] H. V. Nguyen et al., Proc. Int. Conf. on Nuclear Data for Sci. and Technol., Trieste, p. 835 (1997).

[18] K. Tasaka et al., JNDC Nuclear Data Library of Fission Products, JAERI, 1320 (1990)

[19] F. Storrer, Proc. Int. Conf. on Nuclear Data for Sci. and Technol., Gatlinburg, p. 819 (1994).

[20] T. R. England et al., Proc. Int. Symp. on Nucl. Data Eval. Meth., Brookhaven, p. 611 (1992).

[21] K. Takahashi and M. Yamada, Prog. Theor. Phys. 41 (1969) 1470

[22] S. Koyama, K. Takahashi and M. Yamada, Prog. Theor. Phys. 44 (1970) 663

[23] K. Takahashi, Prog. Theor. Phys. 45 (1971) 1466.

[24] T. Tachibana, M. Yamada and Y. Yoshida, Prog. Theor. Phys., 84 (1990) 641.

[25] H. Nakata, T. Tachibana and M. Yamada, Nucl. Phys. A 594 (1995) 27.

[26] T. Tachibana and M. Yamada, Proc. Int. Conf. on Exotic Nuclei and Atomic Masses, Arles, p. 763 (1995).

[27] A. Algora et al., Phys. Rev. C 68, (2003) 034301

[28] D. Cano-Ott, J.L. Tain, A. Gadea, B. Rubio, L. Batist, M. Karny, E. Roeckl, Nucl. Instr. and Meth. A 430 (1999) 333.

[29] J.L. Tain, D. Cano-Ott, Nucl. Instr. and Meth. A 571 (2007) 728.

[30] N. Hagura, T. Yoshida and T. Tachibana, Journal of Nucl. Science and Technology 43 (2006) 497.

[31] R.C. Greenwood, R.G. Helmer, M.H. Putnam, K.D. Watts, Nucl. Instr. and Meth. A390 (1997) 95.

[32] Z. Hu et al., Phys. Rev. C 60 (1999) 024315.

[33] Z. Hu et al., Phys. Rev. C 62 (2000) 064315.

[34] J. Agramunt et al., Proc. of the SGR97 on New Facet of Spin Giant Resonances in Nuclei, Tokio, Japan, p. 150 (1998).

[35] A. Algora et al., Nucl. Phys. A 654 (1999) 727c.

[36] E. Nacher et al., Phys. Rev. Lett. 92 (2004) 232501-1.

[37] E. Poirier et al., Phys. Rev. C 69 (2004) 034307.

[38] P. Möller et al., Phys. Rev. Lett. 97, (2006) 162502.

[39] J. Äystö, Nucl. Phys. A 693 (2001) 477.

[40] V. Kolhinen et al., Nucl. Instrum. and Meth. Phys. Res. A 528 (2004) 776.

[41] L.S. Brown and G. Gabrielse, Phys. Rev. A 25 (1982) 2423.

[42] M. König et al., Int. J. Mass Spectrom. Ion Processes 142 (1995) 95.

[43] V.-V. Elomaa et al., Nucl. Instr. and Meth. A 612 (2009) 97.

[44] G. Gräff, H. Kalinowsky, and J. Traut, Z. Phys. A 297 (1980) 35.

[45] A. Jokinen et al., Int. J. Mass. Spectrom. 251 (2006) 204.

[46] I77 proposal, University of Jyväskylä, Jyväskylä, spokepersons: A. Algora, J. L. Tain.

[47] L. Batist, private comunication.

[48] Geant4 colaboration, Nucl. Instr. and Meth. A 506 (2003) 250.

[49] Enrique Nacher, PhD tesis, University of Valencia 2004.

[50] T. Eronen and I. D. Moore, University of Jyväskylä, private comunication.

[51] ROOT, Object-Oriented Data Analysis Frameork, http://root.cern.ch/root/

[52] K. Debertin and R. G. Helmer, *Gamma- and X-ray spectrometry with semiconductor detectors*, page 164, table 3.2.

[53] D. Cano-Ott, J.L. Tain, A. Gadea, B. Rubio, L. Batist, M. Karny, E. Roeckl, Nucl. Instr. and Meth. A 430 (1999) 488

[54] RIPL-2, Reference Input Parameter Library 2, http://www-nds.iaea.or.at/RIPL-2/

[55] W. Dilg et al., Nuclear Physics A217 (1973) 269.

[56] J. Kopecky and M. Uhl, Phys. Rev. C 41 (1990) 1941.

[57] J.C. Hardy, Phys. Lett 109 B (1982) 242.

[58] W.V. Preswitch, M.A. Islam and T.J. Kennett, Z. Phys. A 315 (1984) 103.

[59] N. B. Gove and M. J. Martin, Nuclear Data Tables 10 (1971) 229.

[60] ENSDF, Evaluated Nuclear Structure Data File, http://www.nndc.bnl.gov/ensdf/

[61] Joint Evaluated Fission and Fusion File, Incident-neutron data, http://www-nds.iaea.org/exfor/endf00.htm, 2 October 2006; see also A. Koning, R. Forrest, M. Kellett, R. Mills, H. Henriksson, Y. Rugama, The JEFF-3.1 Nuclear Data Library, JEFF Report 21, OECD/NEA, Paris, France, 2006, ISBN 92-64-02314-3.

[62] Calculations performed in Valencia using the code of Dr. Tachibana.

[63] D. De Frenne and E. Jacobs, Nuclear Data Sheets 83 (1998) 535.

[64] J. Blanchot, Nuclear Data Sheets 108 (2007) 2035.

[65] D. DE Frenne and E. Jacobs, Nuclear Data Sheets 105 (2005) 775.

[66] D. DE Frenne and A. Negret, Nuclear Data Sheets 109 (2008) 943.

[67] J. Blanchot, Nuclear Data Sheets 109 (2008) 1383.

[68] M.B. Chadwick et at., Nuclear Data Sheets 107 (2006) 2931.

[69] A. Sonzogni, private comunication.

[70] A. Tobias, Prog. Nucl. Energy 5 (1980); A. Tobias, "Derivation of decay heat benchmarks for ^{235}U and ^{239}Pu by a least squares fit to measured data", RD/B/6210/R89 (1989).

[71] P. Möller and J.R. Nix, Atomic Data and Nuclear Data Tables 59 (1995) 185.

Agradecimientos

Mis primeras palabras de agradecimiento van dirigidas a la gente del grupo de espectroscopía γ donde he tenido la oportunidad de desarrollar mi capacidad como investigadora. En especial tengo que dar las gracias a Jose Luis y a Alejandro por introducirme en el mundo del "calor residual". Un tema realmente interesante que ha llegado a fascinarme sobremanera. Imposible también, no dedicarles a Jorge y Pancho unas palabras, puesto que junto a ellos he compartido muchas horas y buenos momentos y espero seguir teniéndolos.

I also want to say thank you to the IGISOL people because their help made this experiment possible, specially to the people in charge of the Penning trap, Tommi and Veli.

En esta tesis no pueden faltar los agradecimientos a "mis chicas y mis chicos": Emma, Mer, Neus, Joan y Pablo. Todos ellos me han demostrado que son amigos de verdad, me han apoyado cuando lo he necesitado y sé que cuando se vayan de postdoc los echaré mucho de menos. Familia y amigos también merecen unas palabras puesto que ellos me han dado la fuerza y el valor de continuar con este trabajo durante todos estos años. También tengo que agradecer a Abel, mi pareja, compañero y amigo, el haber estado conmigo en la recta final de la tesis, ayudándome cuando más lo necesitaba y sabiendo que estaba ahí para todo.